The galactic scale impact of feedback from individual stars

Andersson, Eric

2022

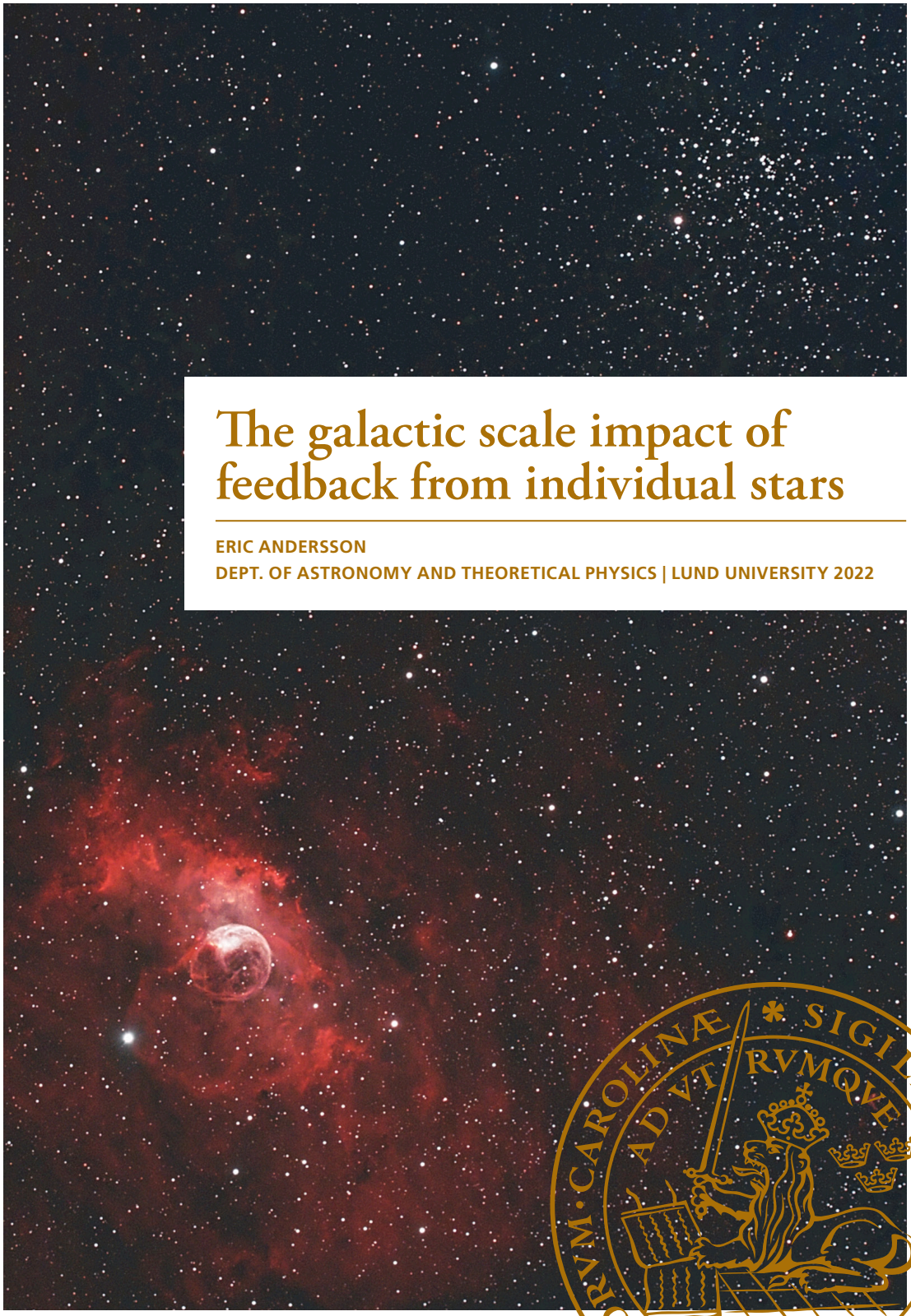

The galactic scale impact of feedback from individual stars

ERIC ANDERSSON
DEPT. OF ASTRONOMY AND THEORETICAL PHYSICS | LUND UNIVERSITY 2022

Printed by Media-Tryck, Lund 2022 NORDIC SWAN ECOLABEL 3041 0903

Faculty of Science
Department of Astronomy and
Theoretical Physics

ISBN 978-91-8039-417-8

The galactic scale impact of feedback from individual stars

Eric Andersson

LUND
UNIVERSITY

Thesis for the degree of Doctor of Philosophy

Thesis advisor: Dr. Oscar Agertz
Co-advisors: Dr. Florent Renaud
Faculty opponent: Prof. Stefanie Walch-Gassner

To be presented, with the permission of the Faculty of Science of Lund University, for public criticism in the Lundmark lecture hall (Lundmarksalen) at the Department of Astronomy and Theoretical Physics on Wednesday, 9th of November, 2022 at 13:00

Organization LUND UNIVERSITY Department of Astronomy and Theoretical Physics Box 43, SE-22100 Lund, Sweden	**Document name** DOCTORIAL DISSERTATION **Date of issue** 2022-10-14
Author(s) Eric Andersson	Sponsoring organization

Title and subtitle
The galactic scale impact of feedback from individual stars

Abstract

Feedback from stars is essential for the formation and evolution of galaxies. It is an energy source that drives gas motions and chemically enriches the galaxy by supplying metals. Without this stellar feedback, numerical galaxy simulations result in galaxies with little resemblance to those observed in our Universe. Modern galaxy simulations frequently reach a mass resolution of a few tens of solar masses. Such high-resolution warrants models incorporating individual stars. These models enable a detailed treatment of when and where stars inject feedback. In this thesis, I present such a model and provide a series of papers exploring physical mechanisms unlocked by this model.

In paper I, we investigate how runaway stars affect the galactic winds driven by stellar feedback in Milky Way-like galaxies. Massive runaway stars can venture to places where these short-lived stars are otherwise not found (e.g., between spiral arms). In these regions of diffuse gas, supernovae can efficiently incorporate energy into large volumes of gas, thereby boosting the gas outflow rate of the galaxy. Furthermore, the star formation rate is not significantly affected since parts of the feedback budget move away from star-forming gas. The result is a ten-fold boost in the mass loading factor.

Paper II is a follow-up investigation of a surprising signal of star formation in spiral galaxies with runaway stars, found in Paper I. The signal is produced by the rapid migration of runaway stars to the galaxy's outskirts. Via direct comparison to observational data, we find that this explains faint far-ultraviolet radiation detected outside the optical radius of nearby spiral galaxies. This radiation manifests as a trend in the star formation relation with a slope similar to one produced by runaway stars escaping to these regions.

In paper III, the star-by-star model is upgraded with a more advanced model for feedback and runaway stars. We showcase this model with a suit of simulations of isolated dwarf galaxies, testing a range of parameters for the natal velocity model of individual stars responsible for incorporating runaway stars. In stark contrast to the Milky Way-like galaxy, we find runaway stars play little to no role in determining outflows in dwarf galaxies. We discuss several possible reasons for the different effects in small and large galaxies.

Key words: galaxies, galaxy evolution, galactic winds, interstellar medium, star formation, stellar feedback, runaway stars, numerical modelling

Classification system and/or index terms (if any)

Supplementary bibliographical information		**Language** English
ISSN and key title		**ISBN** ISBN: 978-91-8039-417-8 (print) ISBN: 978-91-8039-418-5 (pdf)
Recipient's notes	**Number of pages** 137	Price
	Security classification	

Signature  Date 2022-09-28

The galactic scale impact of feedback from individual stars

Eric Andersson

LUND
UNIVERSITY

Faculty Opponent

Prof. Stefanie Walch-Gassner
Physical Institute, University of Cologne,
Cologne, Germany

Cover: Image showing the Bubble Nebula and the open cluster M52. The Bubble Nebula is a region of shocked gas in the interstellar medium created by the wind expelled from the potential runaway O-type star BD+2522. The photo is a 3 hours exposure using a DSLR camera equipped with an L-eXtreme filter and mounted on a 107 mm refractor telescope. Credit: Photo taken and processed by my father, Peter Andersson.

Funding information: This thesis work is financially supported by the Knut and Alice Wallenberg Foundation, the Swedish Research Council (grant 2014-5791 and grant 2019-04659), and the Royal Physiographic Society of Lund (Stiftelsen Walter Gyllenberg fond and Märta och Erik Holmbergs donation).

Faculty of Science, Department of Astronomy and Theoretical Physics

ISBN: 978-91-8039-417-8 (print)
ISBN: 978-91-8039-418-5 (pdf)

Printed in Sweden by Media-Tryck, Lund University, Lund 2022

Contents

List of publications

This thesis is based on the following publications:

I **How runaway stars boost galactic outflows**
E.P. Andersson, O. Agertz, F. Renaud (2020)
Monthly Notices of the Royal Astronomical Society, vol. 494, 3328 (14 pp.)

II **Runaway stars masquerading as star formation in galactic outskirts**
E.P. Andersson, F. Renaud, O. Agertz (2021)
Monthly Notices of the Royal Astronomical Society, vol. 502, L29 (6 pp.)

III **INFERNO: Galactic winds in dwarf galaxies with star-by-star simulations including runaway stars**
E.P. Andersson, O. Agertz, F. Renaud, R. Teyssier (2022)
Submitted to Monthly Notices of the Royal Astronomical Society (17 pp.)

Work not included in the thesis

Peer-reviewed publications not included in this thesis:

I **Tidal stripping as a mechanism for placing globular clusters on wide orbits: the case of MGC1 in M31**
E.P. Andersson, M.B. Davies (2019)
Monthly Notices of the Royal Astronomical Society, vol. 485, 4134-4149 (17 pp.)

II **VINTERGATAN - I. The origins of chemically, kinematically, and structurally distinct discs in a simulated Milky Way-mass galaxy**
O. Agertz, F. Renaud, S. Feltzing, J. Read, N Ryde, **E.P. Andersson**, M. Rey, T. Bensby, D. Feuillet (2021)
Monthly Notices of the Royal Astronomical Society, vol. 503, 5826-5845 (20 pp.)

III **VINTERGATAN - II. The history of the Milky Way told by its mergers**
F. Renaud, O. Agertz, J. Read, N. Ryde, **E.P. Andersson**, T. Bensby, M. Rey, D. Feuillet (2021)
Monthly Notices of the Royal Astronomical Society, vol. 503, 5846-5867 (21 pp.)

IV **VINTERGATAN III: how to reset the metallicity of the Milky Way**
F. Renaud, O. Agertz, **E.P. Andersson**, J. Read, N. Ryde, T. Bensby, M. Rey, D. Feuillet (2021)
Monthly Notices of the Royal Astronomical Society, vol. 503, 5868-5876 (8 pp.)

V **EDGE: The sensitivity of ultra-faint dwarfs to a metallicity-dependent initial mass function**
M. Prgomet, M. Rey, **E.P. Andersson**, A. Segovia Otero, O. Agertz, F. Renaud, A. Pontzen, J. Read (2022)
Monthly Notices of the Royal Astronomical Society, vol. 513, 2326-2334 (8 pp.)

Popular summary

To better understand the Universe, we must also understand the galaxies that inhabit it. The impressive view of the Milky Way band that stretches across the night sky has made galaxies an important topic of conversation throughout history. Already in ancient Greece, it was a subject of debates among philosophers (described in *Meteorologica* by Aristotle[1]). Today, we estimate that the observable Universe is home to a few hundred billion galaxies, found with a wide variety of sizes, shapes, and internal structures.

So what is a galaxy? Since galaxies come in varied shapes and consist of many different components, it is difficult to make a simple definition. The starting point is a system held together by the forces of gravity, and which consists of dark matter, stars, stellar remnants, gas, and dust. The first complication is the fact that, at present, there is no evidence of what dark matter is. There are many indicators of how it behaves; however, not a single experiment has directly detected a particle that can explain it. Stars are the dominant light source, and the luminous shape of the galaxy is commonly used for classification, separating galaxies into elliptical, lenticular, spiral, and irregular types. Gas and dust that lie between the stars make up what is called the interstellar medium. Finally, stellar remnants, such as black holes, are distributed throughout the galaxy. Most galaxies also hold a supermassive black hole at their center, although its origin is not yet well established.

Spiral galaxies (like the Milky Way) evolve cyclically. Surrounding gas flows into them, and is used to create stars. These stars inject energy into their surroundings, heating and pushing gas away. Much of this gas leaves in galactic winds and creates a medium around the galaxy called the circumgalactic medium. Part of this medium reincorporates back into the galaxies, closing the cycle. To study this process, we build theoretical models that we test by simulating galaxies in computers. These simulations are executed on some of the world's most powerful computer facilities, and they allow us to study how dark matter, stars, and gas evolves over millions to billions of year. We can compare these simulations to observations, thereby testing what processes are important, and how these are connected.

Currently, modern simulations of galaxies are unable to represent every single star as an individual element. Because of the numerous stars in a galaxy, there are simply too many calculations to do. Instead, stars are treated as groups, significantly reducing the number of computations. However, this severely limits what can be studied by the models, and as such galaxy theory remains incomplete.

[1] 384 - 322 BCE (Macedonia)

For example, we observe many massive stars in isolation. These stars are not born alone, but end up so after being ejected from their birthplaces. Such stars are called *runaway stars*, an example being the star Betelgeuse. These stars release vast amounts of energy into their surroundings, which makes them very important for galaxy evolution.

With the increasing computational power offered by modern super-computer facilities, we can now incorporate individual stars into galaxy simulations. To this end, I present such a model. Using this star-by-star model, I show that runaway stars play a role in setting the galactic winds driven out of Milky Way-like galaxies and investigate how these stars appear in observations. In these types of galaxies, massive runaway stars can travel to regions where the gas is usually not subjected to the energy released by massive stars (for example, in between spiral arms). When these stars inject energy, they significantly impact gas motions. This leads to strong winds being ejected from the galaxy, which will change how the galaxy evolves over long periods. Furthermore, runaway stars can leave the galaxy entirely and venture to their outskirts. These stars naturally explain observations of highly energetic light coming from these regions, which has puzzled astronomers for the past decade.

Models with individual stars allow us to account for every star's position and velocity and are therefore the first steps toward simulations with an exact representation of entire galaxies. By strengthening the link between our theoretical understanding of stars and galaxies, star-by-star models will serve an important role in the astrophysical theory.

Populärvetenskaplig sammanfattning

Att studera galaxer är mycket viktigt för vår förståelse av Universum. Vintergatans band som sträcker sig över natthimmeln och skapar en imponerande vy har haft stor betydelse för diskussioner om galaxer genom historien. Redan i antikens Grekland debatterade filosofer om vad dessa galaxer skulle kunna vara, något som dokumenterats i *Meteorologica* av Aristoteles[2]. Idag vet vi att det finns flera hundra miljarder galaxer i Universum, och att dessa har en mängd olika storlekar och former.

Så vad är egentligen en galax? Detta är inte enkelt att definiera, eftersom galaxer finns i så många olika former och dessutom består av flera olika komponenter. Utgångspunkten är att beskriva dom som system, sammanhållna av gravitationskrafter, och som består utav mörk materia, stjärnor, gas, damm och det som efterlämnas när stjärnor dör, till exempel svarta hål. Ett första problem med denna beskrivningen är att vi ännu inte vet vad mörk materia är. Trots att det finns många indikationer över att de existerar, så har vi ännu inte lyckats finna någon partikel som kan förklara vad det är. Stjärnor är källan till det mesta av ljuset i en galax, och den struktur som dessa bygger upp används ofta för att dela upp galaxer i olika klasser. Bland annat delas galaxer ofta in i elliptiska, linsformade, spiraler, och irreguljära typer baserat på den form som stjärnorna utgör. Mellan stjärnorna så finns en stor mängd gas och damm, vilket kallas för interstellärt medium. Den sista komponenten till vad som utgör en galax är det som efterlämnas när stjärnor dör, nämligen svarta hål. Dessa skapas då tunga stjärnor slutar sina liv och ligger utspridda i galaxen. Dessutom har också de flesta galaxer ett super-massivt svart hål i sitt centrum, vars ursprung fortfarande inte är känt för oss.

Hur spiralgalaxer (till exempel Vintergatan) utvecklas över tid kan beskrivas som ett kretslopp. Gas flödar från omgivningen till galaxen, där den kan omvandlas till stjärnor. Dessa kan sedermera förse sin omgivning med energi, vilket hettar upp gas och flyttar omkring den. En stor del av denna gasen lämnar galaxen i en såkallad galaktisk vind, vilket skapar ett medium som omger galaxen. Gasen i detta medium kan sedan falla tillbaks på galaxen och gasens kretslopp kan börja om på nytt. För att studera detta kretslopp så bygger vi teoretiska modeller som sedan kan testas i datorer. Dessa tester kallar vi för galaxsimuleringar och vi kör dessa datorprogram på några av världens mest kraftfulla datorer. Med hjälp av simuleringar kan vi undersöka hur olika fysiklagar påverkar galaxen, vilket vi sedan kan jämföras med de stillbilder av Universum som världens största teleskop förser oss

[2] 384 - 322 f.Kr (Makedonien)

med.

Moderna galaxsimuleringar behöver dock göra många förenklingar för att datorerna vi har ska klara av att köra dem. Till exempel så går det ofta inte att inkludera enskilda stjärnor eftersom galaxer innehåller så många. Istället behandlar vi stjärnor i grupp, något som gör att vi behöver göra mindre uträkningar. Denna förenkling förhindrar oss från att testa många intressanta egenskaper hos stjärnor. Bland annat så har vi observerat många väldigt massiva stjärnor som befinner sig långt ifrån andra stjärnor. Dessa stjärnor föds tillsammans med andra stjärnor men blir ivägsparkade genom starka gravitationskrafter från andra stjärnor. Vi kallar dessa för skenande stjärnor (eller flykt-stjärnor) och ett exempel som kan ses på natthimmeln är stjärnan Betelgeuse. Eftersom dessa massiva stjärnor frigör otroliga mängder energi till sin omgivning, är de mycket betydelsefulla för galaxernas kretslopp.

Med hjälp av den ökade beräkningskraften som erbjuds av allt nyare datorer, står vi nu redo för simuleringar av galaxer med enskilda stjärnor. Jag presenterar därför en modell som gör just detta. Med denna modellen, kan jag bland annat visa hur skenande stjärnor spelar en viktig roll för galaxvindar, samt hur de påverkar galaxernas utseende. I galaxer som Vintergatan, så lyckas de skenande stjärnorna flyttas till områden där man vanligvis inte förväntar sig tunga stjärnor, till exempel mellan spiralarmar. Där kan de mycket effektivt frigöra stora mängder energi vilken ändrar hur gasen i galaxen rör sig. Dessutom så flyr många av dem till utkanten av galaxen. På detta sätt blir de en naturlig förklaring till observationer av mycket energirikt ljus i dessa områden, något som ger svar på en gåta som har förbryllat forskare de senaste årtiondet.

Galaxmodeller med enskilda stjärnor är nästa steg i utvecklingen av dator simuleringar. Genom sammankopplingen av teorier om stjärnor och galax modeller så skapas ändlösa förutsättningar för ny forskning.

Acknowledgements

First and foremost, I wish to express my deepest gratitude to my supervisors Oscar Agertz and Florent Renaud. You have made my journey to a Ph.D. one of the most exciting and impactful periods in my life. Both of you have provided me with so much knowledge. Oscar, you have made my curiosity grow, not only for astrophysical science but the world in general. Florent, you have taught me the importance of paying attention to detail and doing what is right, not what is easy. I think of you both as dear mentors and close friends.

I want to thank Linn for all the love and support you have provided. Without you, I would likely not have embarked on this journey. I also want to acknowledge my loving family for motivating me to start pursuing a career in science. If anyone knows how insurmountable pursuing a Ph.D. feels like when coming from the tiny village of Grönahög, without any real experience of the natural sciences, it is you. A special thanks to my brothers Henrik and Johan for all the time spent together to discuss life and all the choices one makes along the way. I also want to extend this gratitude to Sverker and Eva for serving as an extra family here in Skåne.

For helping me improve the quality of this thesis (for example, pointing out grammatical issues or helping me clarify my thoughts), I want to acknowledge Oscar Agertz, Bibiana Prinoth, Linn Eriksson, Álvaro Segovia Otero, Daniel Mikkola, and Henrik Andersson. I also wish to thank Martin Rey, Romain Teyssier, Ulrich Steinwandel, and Stacy Kim for insightful conversations and for inviting me to visit cool places around the world. I wish to thank Jessica Hislop for encouraging me not to burn out during the final period of writing this thesis.

A special thanks to my amazing office mates, Brian Thorsbro and Álvaro Segovia Otero. You made the time spent in the office a time of joy, with tons of memes, music, quotes, insightful conversations, and many silly moments. I also want to express gratitude to all other great friends I have made at the department. In particular, "*I like my name*" Álvaro, Bibi, Mikkola, Madeleine, Nic, FunkyFloFlo, chefen O, Martin, Ma$$teo, Giorgi, and Noemi, with whom I have spent considerable time with outside work hours.

Last, but not least, I want to acknowledge all the support provided by friends outside the department. I want to highlight my close friends Vassily Kornienko, Martin Larsson, and Jonathan Klasson for all the amazing moments and conversations we have shared. I'm also thankful to all the awesome people that I got to know through the band Leading Edge[3], in particular Anna Johannisson, Lewis

[3]Check us out on Spotify and social media! (shameless plug)

Belcher, Alexander Folke Rohlin, Sebastian Wolsing, and Vassily Kornienko. You let me think about things outside work, which has been especially helpful for my well-being in stressful times.

Finally I want to acknowledge help from a few of the quotes that ended up on the board Álvaro and me set up in the office. Hopefully I can come back to these for encouragement, or at least mild amusement.

"*Life gets better*"
- BT
"*Falafel is surprisingly rewarding*"
- ÁSO
"*If you have a lot of work to do, then lagom amount of coffee is a lot of coffee*"
- ÁSO
"*I should take a week to get my life together*"
- EA
"*I'm too awesome to write it down*"
- FR

Part I

Research context

Preface

My thesis concerns models which incorporate individual stars in galaxy simulations. It has to cover a broad range of both astrophysical and technical topics. I have divided this into two separate chapters, the first focusing on astrophysics and the second on numerical methods and modeling. The scientific question of this thesis is *how runaway stars affect galaxy evolution*.

The research content of this thesis consists of a series of three papers focusing on star-by-star simulations of galaxies and a particular emphasis on runaway stars. Below I summarize each article.

Paper I: *How runaway stars boost galactic outflows*
We compare two simulations of a Milky Way-like galaxy with a model resolving massive ($> 8\ \mathrm{M}_\odot$) stars as individual particles. In one simulation, we apply velocity-kicks to massive stars at birth, sampled from a velocity distribution of stars escaping birth clusters (effectively modeling runaway stars). The other simulations serve as an example of ignoring runaway stars, therefore, apply no such kicks. We find that including runaway stars severely affects the ability of stellar feedback to drive outflows, while the cold star-forming ISM remains similar to the case without runaway stars. The result is a boost in the mass loading factor of one order of magnitude, an effect seen regardless of where this quantity is measured. We argue that the process responsible for this boost is runaway stars which travel to large bubbles of diffuse gas in the inter-arm regions of the galaxy. This enables some supernovae explosions to couple energy to large volumes of gas, efficiently heating it and sustaining strong outflows at moderate star formation rates.

Paper II: *Runaway stars masquerading as star formation in galactic outskirts*
We investigate the star formation relation (Σ_{SFR} versus Σ_{gas}) resolved at kpc-scale of the two simulations presented in Paper I. We find that the rapid migration of runaway stars into the outskirts of the galaxy results in a separate trend of roughly constant depletion time ($\Sigma_{\mathrm{gas}}/\Sigma_{\mathrm{SFR}} \sim 100\,\mathrm{Gyr}$). This trend can explain observations of slow star formation in molecule-poor gas without invoking exotic star formation recipes. Furthermore, we predict a deficit of O-type stars associated with this trend since these stars have too short lives to reach the outskirts, in contrast to *in-situ* star formation (for which such a deficit is unexpected). There is observational data in favor of our prediction; however, the quality of this data has been debated in the literature.

Paper III: *INFERNO: Galactic winds in dwarf galaxies with star-by-star simulations including runaway stars*

We expand the star-by-star model presented in Paper I to become INdividual stars with Feedback, Enrichment, and Realistic Natal mOtions (INFERNO), generalizing the sampling method for individual stars to any initial mass function and arbitrary mass threshold for resolved stars. We present improvements to the stellar feedback model, which incorporates mass and metal ejection rates from on-the-fly interpolation of lookup tables (retrieved from detailed stellar evolution models). An upgraded velocity kick model is presented, accounting for user-defined fractions of ejected stars (including runaway stars) and natal velocity dispersion. We showcase INFERNO with simulations of dwarf galaxies with varying natal velocity parameters, finding that runaway stars play little to no role in setting the galactic outflows. We discuss why runaway stars have a small effect, particularly in contrast to more massive galaxies (Paper I), and compared to contradicting results from contemporary work with dwarf galaxies. We highlight, for example, the internal properties of the wind (e.g., temperature and velocity) and star formation modeling as future topics to study to address this lack of consensus.

Chapter 1

Fundamental aspects of galaxy theory

"The Universe, what a concept!"
– Tim & Eric Awesome Show, Great Job!

1.1 Introduction

Galaxies serve as a link between the large-scale structure of the Universe[1] and the stars we view in the night sky. To be at the intermediary of this vast range of scales demands that galaxy theory takes into account many intricate processes, connecting widely different aspects of physics. A complete theoretical framework to explain how galaxies form and evolve is therefore often considered one of the grand challenges in natural science.

Galaxies were described by Wright (1750) and later Kant (1755) as isolated, gravitationally supported discs of stars (similar to scaled-up versions of our own Solar System, referred to as *Island Universes*). This description followed the discovery that the Milky Way band stretching over the sky consisted of uncountable numbers of stars (Galilei, 1610). Arguments in favor of and against these *Island Universes* being extra-galactic culminated in *The Great Debate* held at the Smithsonian Museum of Natural History (Washington, D.C.) in 1920 and the subsequent publication by Shapley & Curtis (1921). The extra-galactic origin of the Andromeda galaxy was later confirmed and published by Hubble (1929b). For

[1] When refereeing to *our* Universe or *our* Galaxy, I use convention of upper case first letter.

star-forming spiral galaxies, the idea of *Island Universes* is not far from the modern picture of galaxies (see Veilleux et al., 2020, for more discussion). The current paradigm views galaxies as collections of dark matter, stars, gas, dust, and other forms of matter, such as black holes and highly relativistic particles (cosmic rays). The luminous component (found in various sizes and morphologies) sits at the center of extended dark matter structures. The variety indicates that the evolution of these objects can take many different paths. *How* and *why* these evolutionary paths differ between galaxies is a central question to modern galaxy theory.

Broadly, modern galaxy theory separates into three fundamental aspects of the Universe (see Mo et al., 2010, for a similar, but more detailed description): 1) Cosmology, i.e., what is the framework that sets the spatial and temporal scales for galaxy formation and evolution; 2) Initial conditions, i.e., what is the starting point of the process that eventually leads to an object like the Milky Way; 3) Physical processes, i.e., what laws of nature govern the processes, which along with the first two aspects results in the variety of galaxies that we observe in the Universe.

In this first Chapter, I focus on the current empirical knowledge of galaxies (Section 1.3) and important theoretical concepts necessary for galaxy modeling (Sections 1.4 and 1.5). I briefly introduce a few general cosmology concepts, which are important for galaxy theory (Section 1.2). Finally, I give an overview of how the effects of stellar feedback are typically measured in both observed and simulated galaxies (Section 1.6).

Galaxy theory is an extensive field of research; therefore, I have omitted many details. For the interested reader, I recommend the book *Galaxy Formation and Evolution* by Mo et al. (2010) for a more complete account of the topic.

1.2 Cosmology and initial conditions

Cosmology is the study of how a universe originates and evolves on its largest spatial and temporal scales. Modern cosmological theories about our Universe have their basis in the theory of general relativity (GR) formulated first by Einstein (1915). GR builds on the equivalence principle and describes the forces of gravity as a consequence of curvature in the geometry of the space-time continuum[2]. A fundamental assumption of modern cosmological models is the cosmological principle, which states: "*Viewed on a sufficiently large scale, the properties of the Universe*

[2]Space-time is a four-dimensional manifold which describes locations in terms of three-dimensional space and time.

are the same for all observers." In other words, the Universe is homogeneous and isotropic on large scales. With the cosmological principle, the GR equations describing our Universe simplify greatly. For example, the space-time metric (which describes incremental displacement) is determined by the Robertson-Walker metric (see, e.g., Robertson, 1936; Walker, 1937), which in polar coordinates (r, θ, φ) is

$$\mathrm{d}s^2 = c^2\mathrm{d}t^2 - a^2(t)\left(\frac{\mathrm{d}r^2}{1-Kr^2} + r^2\mathrm{d}\theta^2 + \sin^2(\theta)\,\mathrm{d}\varphi^2\right), \tag{1.1}$$

where c is the speed of light, $a(t)$ is the time-dependent scale factor, and K is a constant that takes values $-1, 0, 1$ for negatively curved, flat, or positively curved geometry, respectively. The scale factor is calculated via the Hubble parameter H, derived from the Friedmann equations (Friedmann, 1922). In the case of a homogeneous and isotropic universe, the Hubble parameter is given by

$$H^2 = \left(\frac{\dot{a}}{a}\right)^2 = \frac{8\pi G}{3}\rho - \frac{Kc^2}{a^2}, \tag{1.2}$$

where the dotted notation denotes time derivatives. In practice, one introduces a scale-free density parameter $\Omega = \rho/\rho_c$, where ρ_c is the critical density that separates a contracting and expanding universe. Using this quantity, we can describe the cosmic evolution of the Universe by five parameters:

$$\left(\frac{H}{H_0}\right)^2 = \Omega_{0,R}a^{-4} + \Omega_{0,m}a^{-3} + \Omega_{0,K}a^{-2} + \Omega_{0,\Lambda}, \tag{1.3}$$

where the zeroth subscript refers to the present-day value of a given parameter, and the density parameters refer to radiation, mass, curvature, and vacuum, in the order from left to right. Interestingly, our Universe expands according to the Hubble–Lemaître law

$$v_r = H_0\, r. \tag{1.4}$$

First published by Lemaître (1927) and later by Hubble (1929a), this law is arguably one of the most important discoveries in modern astrophysics. Furthermore, the relative change in wavelength for photons depends on the expansion of the Universe (i.e., on the scale factor), which allows us to derive cosmological redshift z according to

$$a(t) = \frac{1}{1+z}. \tag{1.5}$$

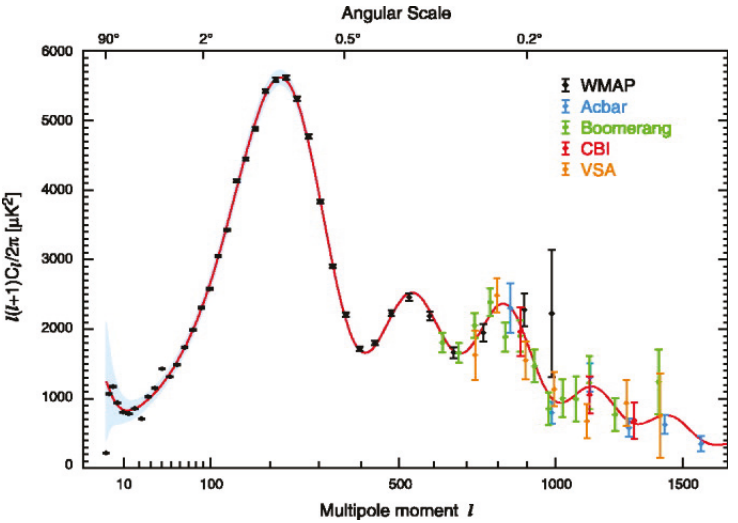

Figure 1.1: Temperature fluctuations in the angular power spectrum of the cosmic background radiation as function of angular scale, with points showing results from WMAP in black (Hinshaw et al., 2007), ACBAR in blue (Kuo et al., 2004), BOOMERANG in green (Jones et al., 2006), CBI in red (Readhead et al., 2004), and VSA in orange (Dickinson et al., 2004). The red lines show a best-fit model assuming ΛCDM cosmology with the light blue band showing the 1σ cosmic variance (Spergel et al., 2007). Figure adapted from Hinshaw et al. (2007). © AAS. Reproduced with permission.

For modern galaxy theory, cosmology is often considered a solved problem. Only a few different cosmological models are frequently applied, the main difference being the model for dark matter (going into Equation 1.3 via Ω_m). Out of these, Λ Cold Dark Matter (ΛCDM) is currently the most widely used cosmological framework for galaxy models. ΛCDM assumes a flat ($\Omega_K = 0$) and expanding Universe (non-zero cosmological constant Ω_Λ), with CDM introducing a significant fraction of non-baryonic, kinematically cold ($v \ll c$), dissipationless and collisionless dark matter. Originally, dark matter was introduced to explain the flat rotation curves of spiral galaxies (first mentions in, e.g., Kapteyn, 1922; Lundmark, 1930). In modern times, the most stringent constraints are derived from the observations of galaxy clusters (e.g., the Bullet cluster, see Clowe et al. 2004) or the cosmic microwave background (CMB).[3] An example of the latter is shown in

[3]The cosmic microwave background is the radiation signature released from the Universe at the epoch of recombination, during which baryonic matter transitioned from ionized to neutral

Figure 1.1, comparing the power spectrum of the CMB temperature structure to a best-fit model of ΛCDM. The fit has since been improved, in particular with the release of the Planck data (Planck Collaboration et al., 2020a,b), and the current parameters are $H_0 = 67.66 \pm 0.42\,\mathrm{km\,s^{-1}\,Mpc^{-1}}$, $\Omega_{0,m} = 0.3111 \pm 0.0056$, $\Omega_{0,K} = 0.0007 \pm 0.0019$, and $\Omega_{0,\Lambda} = 0.6889 \pm 0.0056$. Planck does not provide a direct measurement of $\Omega_{0,R}$, as matter completely dominates radiation in the present Universe. Nonetheless, a value for $\Omega_{0,R}$ can be derived from the redshift when the energy densities of matter and radiation were equal, which Planck finds to be $z_{eq} = 3387 \pm 21$. Furthermore, the matter component is split into baryonic and dark matter, according to $\Omega_{0,m} = \Omega_{0,b} + \Omega_{0,dm}$ ($\Omega_{0,b}h^2 = 0.0224 \pm 0.0001$, $\Omega_{0,dm}h^2 = 0.120 \pm 0.001$, where h is the value of the Hubble parameter in units $100\,\mathrm{km\,s^{-1}\,Mpc^{-1}}$).

The CMB does not only provide a method to determine the parameters for the cosmological model but also provides an estimate of the initial density fluctuations of the early Universe. As such, it can provide us with initial conditions for cosmological simulations.

1.3 The empirical study of galaxies

Galaxies make up roughly 10% of the cosmic baryon budget, fundamental components being dark matter, stars, gas, and dust (see, e.g., Naab & Ostriker, 2017, for a detailed overview). Dark matter forms a halo that encapsulates the galaxy and is the dominant form of mass. Although no direct measurements of dark matter have yet been made, dark matter halos are typically assumed to be radially symmetric, and in the ΛCDM framework the radial profile can be approximated by

$$\rho(r) = \frac{\delta_c \rho_c}{\frac{r}{r_s}\left(1 + \frac{r}{r_s}\right)^2}, \tag{1.6}$$

where δ_c is a dimensionless constant, ρ_c is the aforementioned critical density, and r_s is a characteristic radius (Navarro et al., 1996). This profile is named the NFW[4] profile and is commonly formulated in terms of r_{200} (given by r_s multiplied by a concentration parameter, which is the radius where the density of the

gas (roughly 370 000 years after Big Bang). This radiation has a spectrum of a black body at a temperature of 2.73 K, and is almost perfectly isotropic with fluctuations only at parts per million level. For more details, see, e.g., Samtleben et al. (2007).

[4] After Julio Navarro, Carlos Frenk, and Simon White who originally purposed it

profile is equal to 200 times the critical density). In reality, this profile is a good fit for rotation curves of massive galaxies; however, many dwarf galaxies display a shallower central density profile. This non-universality of dark matter profiles has been a considerable problem for ΛCDM models, often called the *cusp-core problem* (Moore, 1994). Processes such as stellar feedback can transform cuspy profiles (e.g., the NFW profile) into cored ones. Therefore, this problem is typically considered a solved one (see, e.g., Read et al., 2016). Stars make up the optically visible component which is typically described by a spherically shaped central region (bulge) with a de Vaucouleurs profile (de Vaucouleurs, 1948), and a flat, rotationally supported disc with an exponential density profile (see van der Kruit & Freeman, 2011, and references therein). For the Milky Way (as well as many other spiral galaxies), the central region holds a bar-like structure and multiple disc components (see review by Bland-Hawthorn & Gerhard, 2016). Gas and dust constitute a significant fraction of the mass budget for a galaxy ($\sim$ 10% in cold gas for Milky Way-like galaxies and higher in low mass galaxies, Naab & Ostriker 2017). Furthermore, most galaxies host a central supermassive black hole at their center (see e.g., Event Horizon Telescope Collaboration et al., 2019, 2022). These are compact objects with masses in the range 10^5 to 10^{10} $M_\odot$, and the accretion of material onto them makes them extreme sources of radiation, typically referred to as active galactic nuclei (AGN) or quasi-stellar objects (quasars). These are important for a number of astrophysical topics, e.g., as background sources for absorption spectroscopy and feedback in massive galaxies. A thorough description of these is beyond the scope of this thesis (for further reading, see, e.g. Fabian, 2012; King & Pounds, 2015).

Galaxies are classified by their morphology (see the seminal paper by Hubble, 1926), typically quantified by the ratio between the spheroid and disc component (see, e.g., Sandage, 2005). In the original work, Hubble (1926) organized galaxies into a tuning fork, referring to galaxies with smooth elliptical light profiles as early types and galaxies with a spheroid center surrounded by a spiraled disc as late types. Early-type galaxies are denoted E0, E1, E2, etc., in order of increasing ellipticity. Late-type galaxies separate into S for normal and SB for barred galaxies. These are further subdivided by a, b, c, etc., depending on how tight the spiral structure is. Furthermore, Hubble included an intermediate class, S0 (also called lenticular galaxies), and a class of irregular galaxies that did not fit any classification.

A fundamental aspect of galaxy theory is understanding the distribution of galaxies in the Universe. Quantifying galaxies by luminosity L, this distribution is called the galaxy luminosity function $\Phi(L)$. It is commonly fitted by a Schechter

function (Schechter, 1976):

$$\Phi(L) = \Phi_\star \left(\frac{L}{L_\star}\right)^\alpha \exp\left(-\frac{L}{L_\star}\right), \tag{1.7}$$

where the $\Phi_\star$ is a normalizing constant, $L_\star$ is a characteristic luminosity, and α determines the slope of the faint end. $L_\star$ determines the luminosity where the function turns over, and more luminous galaxies become exceedingly rare. If considering galaxies of all types, $L_\star$ corresponds to a magnitude of ~ -21.5. Notably, this is similar to the magnitude of the Milky Way and Andromeda and is often used to refer to galaxies of this size. Examples of empirically fitted luminosity functions on the Schechter form are shown in Figure 1.2, including fits separated by morphological type. In this figure, the most massive galaxies are found to be mostly early-type (E), while most small galaxies are irregular (Irr). Disc galaxies (S0, Sa, Sab, Scd) tend to lie around the turn-over magnitude (c.f., $L_\star$).

1.3.1 The circumgalactic medium

The circumgalactic medium (CGM) surrounding galaxies is typically defined as the medium between the disc and the virial radius $R_{\rm vir}$ of the halo. It primarily consists of gas, although there is the presence of dust (detected through reddening of background quasars, see, e.g., Ménard et al. 2010). The gaseous component has been observed through a variety of methods (see Tumlinson et al., 2017, and references therein). Examples of these methods include investigating absorption spectra of either background sources or with the galaxy itself as a source (the latter referred to as "down the barrel") or emission-line spectroscopy from the CGM gas itself. The latter method has been applied to extensively map the Milky Way's CGM, in particular, using the 21 cm radio line (neutral hydrogen spectral line), but with X-ray and UV/optical as well (Tumlinson et al., 2017). The wide spectral range of the observational methods reveals a medium that includes many different ions, covering orders of magnitude in ionizing energy. Such a wide range of ions implies that the CGM is a highly multi-phase medium, with gas spanning a large range of temperatures and densities. Since the CGM is comprised of material brought to the galaxy (e.g., accretion from the intergalactic medium, see McQuinn 2016) and material ejected from the galaxy in outflows (see details in Section 1.6), this is not surprising. This cyclic process is illustrated in Figure 1.3, which also highlights how the gas flows between the different phases. Furthermore, long cooling times (see Section 1.4.2) of diffuse gas imply that material remains there

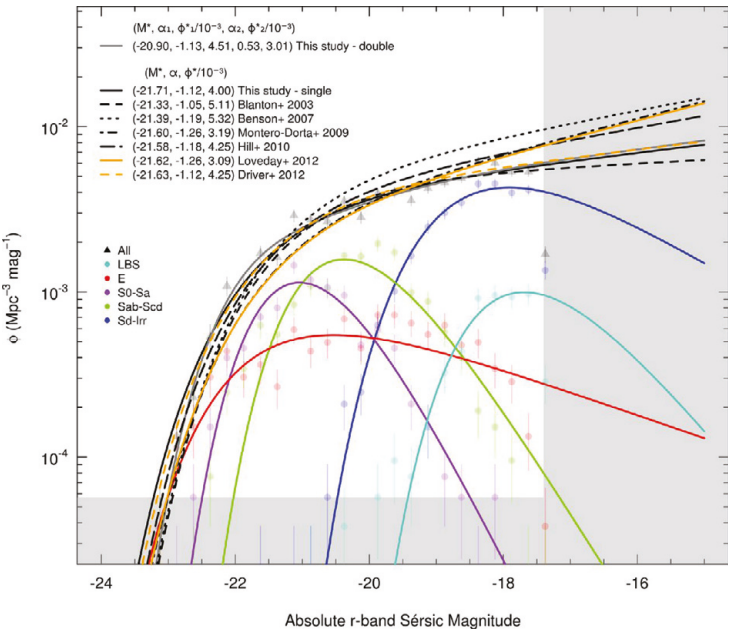

Figure 1.2: Galaxy luminosity function split by morphology and fitted by the Schechter function (Equation 1.7), in this case as a function of magnitude. The fits shown are described in Kelvin et al. (2014), using a collection of different data sets (see legend, Blanton et al., 2003; Benson et al., 2007; Montero-Dorta & Prada, 2009; Hill et al., 2010; Driver et al., 2012; Loveday et al., 2012; Kelvin et al., 2014). Figure adapted from Kelvin et al. (2014) with permission.

for extended periods. This notion is also supported by numerical models (see e.g. Oppenheimer et al., 2016; Esmerian et al., 2021).

A long-standing problem for galaxy theory is the apparent lack of baryonic matter in the present Universe compared to shortly after the Big Bang. At present day, galaxies make up $\sim 10\%$ of the baryonic budget, and the intergalactic medium can be attributed to roughly 50% of the remaining material (see, e.g., Shull et al., 2012; McQuinn, 2016). The CGM is often considered one of the keys to solving this *missing baryons problem*. However, the multi-phase nature of the CGM makes it difficult, if not impossible, to estimate its total mass observationally (Tumlinson et al., 2017; Veilleux et al., 2020). With modern observational facilities and techniques, $\sim 25\%$ of the baryon budget has been accounted for in the CGM, with the vast majority of gas ($15-20\%$ of baryon budget) observed in the cool/warm (10^4-10^5 K) phase, $2-5\%$ in the hot ($>10^6$ K) phase, and small contributions

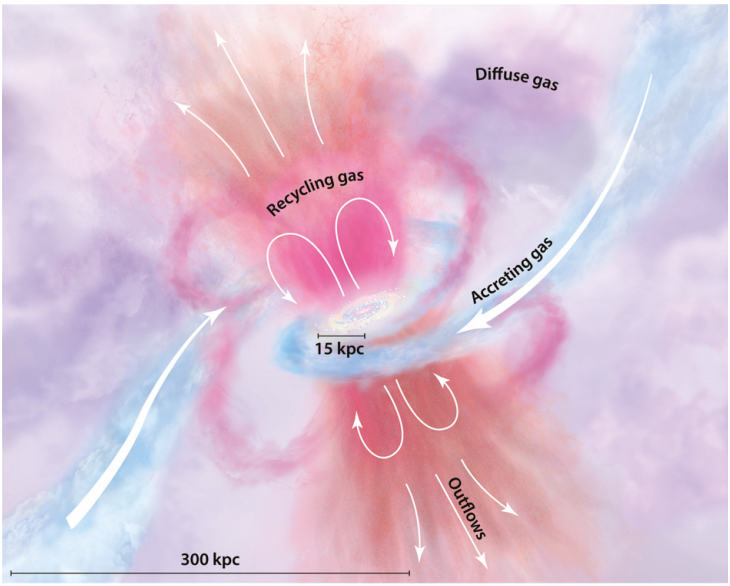

Figure 1.3: Illustration of the circumgalactic medium surrounding an evolving spiral galaxy. Figure adapted from Tumlinson et al. (2017) with permission.

($< 1\%$) in cold ($< 10^4$ K) gas and dust (see Tumlinson et al., 2017, and references therein). Warm ($10^5 - 10^6$ K) gas in the CGM is likely a major contributor to the remaining 15%, however, current observational techniques for this phase cannot place any reliable constraints on what the fraction is. Furthermore, the baryon fraction attributed to the CGM can be severely affected by assumptions regarding the metal content of the gas (Shull et al., 2012).

1.3.2 The interstellar medium

A significant fraction of the galactic disc consists of gas and dust, which reside between the stars. This material is referred to as the interstellar medium (ISM). As with the CGM, gas in this medium is highly multi-phase (i.e., found in molecular, atomic, and ionized states, see, e.g., McKee & Ostriker, 1977). The medium also includes highly energetic particles (cosmic rays). In this thesis, I focus on the gaseous component but note that dust and cosmic rays are not insignificant for the physics of the ISM, as these are important for its chemistry, cooling, and heating (see, e.g., Mo et al., 2010; Krumholz, 2015).

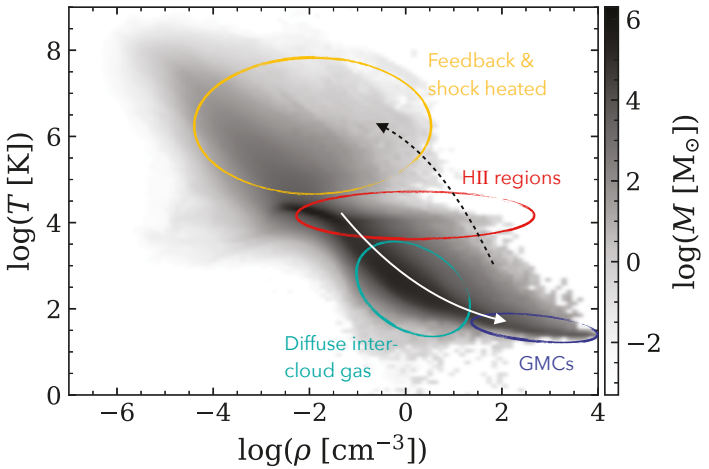

Figure 1.4: Phase diagram weighted by gas mass for the ISM in a galaxy simulation. Mass accumulates in thermally stable regions of this diagram, where gas has long cooling times. Examples are the main cooling track along the white arrow, or the region around 10^4 K, where the cooling rate drops sharply with temperature as hydrogen becomes increasingly inefficient as a coolant (see details in Section 1.4.2). The figure was created using data from one of the simulations in Paper III.

An overview of the phases existing in the ISM is provided in Figure 1.4, showing the mass of gas in the temperature-density space. Molecular gas has temperatures ~ 10 K, while atomic gas is typically described as either cold ($50 - 100$ K) or warm ($6000 - 10^4$ K). Regions around the most massive stars are exposed to strong radiation, which can ionize hydrogen (so-called HII regions). These regions have temperatures around 10^4 K and extend a wide range of densities. Gas is ionized at warm ($\sim 10^4$ K) and hot ($\sim 10^6$ K) temperatures. The most extreme gas temperature ($> 10^5$) is reached primarily by shock heating from supernovae ejecta (see Section 1.5 for details).

Keep in mind that gas is a continuous form of matter, which is in a constant state of flux between different phases, i.e., no permanent gas structures exist in a galaxy. The gas is continuously heated, cooled, mixed, and diluted through converging or diverging flows, shear, and gas instabilities. Therefore, the notion of clouds as discrete objects often leads to confusion.[5] Clouds as discrete objects

[5] This brings to mind the philosophical thought experiment The Ship of Theseus, which in mod-

refer to time-stamps of gas structures that either exceed some density threshold relative to the local medium or are encapsulated by some boundary (e.g., dust column density cuts). For a deeper discussion about observational and theoretical complications regarding this confusion, see Chevance et al. (2022).

Giant molecular clouds

Structures of dense cold gas in the ISM are referred to as giant molecular clouds (GMCs). The term GMC was coined in response to the detection of CO emission organized in large ($10^4 - 10^6$ $M_\odot$) cloud-like structures of cold (10 K) and dense ($\rho_{H_2} \sim 10^2$ cm^{-3}) gas (for early observational work, see e.g., Wilson et al., 1970; Lada, 1976; Blair et al., 1978; Blitz & Thaddeus, 1980; Solomon et al., 1987; Scoville et al., 1987; Dame et al., 1987, 2001). Since then, new observational facilities[6] applying modern techniques, as well as a better theoretical understanding, have led to a significantly improved understanding of GMCs. In particular, large surveys have supplied good empirical constraints on cloud properties, both for the Milky Way (e.g., FUGIN, Umemoto et al. 2017; MWISP, Su et al. 2019, SEDIGISM, Schuller et al. 2021), and for extra-galactic sources (in particular PHANGS, see e.g., Rosolowsky et al., 2021; Lee et al., 2022; Emsellem et al., 2022). In a recent review, Chevance et al. (2022) lists the environmental dependence on the properties, scaling relations, star formation process, lifetime, and destruction of GMCs as the major prospect of GMC studies.

Keeping in mind the continuous nature of gas, there are a few important results that can be derived by viewing GMCs as a population of discrete objects with properties like mass M, radius R, and internal motions σ_v. These properties are estimated via observables. For example, M is typically derived from CO emission (requiring CO mass to H_2 mass conversion X_{CO}), R requires some geometry to convert from cloud area to size (typically assuming spherical clouds), and σ_v is derived from line-of-sight velocity dispersion. This implies that measurements are prone to systematic errors.

Firstly, the mass spectrum of molecular clouds in both the Milky Way and external galaxies can be described by a power-law, which on the form proposed by

ern terms can be described: *If you change all the parts of your car, is it still the same car?* If not, when did it seize to be the same car? If so, what car do you get if you put all the old parts back together?

[6]Some notable examples of modern telescopes are The Atacama Large Millimeter/submillimeter Array (ALMA), the Hubble Space Telescope (HST), the Very Large Telescope (VLT), and more recently the James Webb Space Telescope (JWST).

Williams & McKee (1997) is given by

$$\frac{\mathrm{d}N}{\mathrm{d}\ln M} = N_{\mathrm{u}} \left(\frac{M_{\mathrm{u}}}{M}\right)^{-\gamma}, \quad M \leq M_{\mathrm{u}}, \tag{1.8}$$

where N_{u} is the number of clouds close to the upper mass limit M_{u}. The empirical values for the parameters are $N_{\mathrm{u}} \approx 10$, $M_{\mathrm{u}} \approx 6 \times 10^6$ $\mathrm{M}_\odot$, and $\gamma \approx 0.7$ (see, e.g. Rosolowsky, 2005; Colombo et al., 2014; Heyer & Dame, 2015; Miville-Deschênes et al., 2017; Chevance et al., 2022). Of historical importance are the scaling relations for GMCs derived by Larson (1981). In the original work, these were presented as:

$$\sigma_v = 1.10 \left(\frac{L}{\mathrm{pc}}\right)^{0.38} \mathrm{km\,s^{-1}}, \tag{1.9}$$

$$\sigma_v = 0.42 \left(\frac{m}{\mathrm{M}_\odot}\right)^{0.2} \mathrm{km\,s^{-1}}, \tag{1.10}$$

$$\langle \rho_{\mathrm{H_2}} \rangle = 3400 \left(\frac{L}{\mathrm{pc}}\right)^{-1.10} \mathrm{cm^{-3}}, \tag{1.11}$$

where σ_v is the root mean square of the gas velocity, L is the size, and $\rho_{\mathrm{H_2}}$ is the number density of molecular hydrogen. These results are typically interpreted as GMCs having roughly constant surface density $\Sigma_{\mathrm{mol}} \approx 10^2$ $\mathrm{M_\odot\,pc^{-2}}$, a structure determined by turbulent gas flow ($\sigma_v \propto R^{\mathrm{constant}}$), and an equipartition between gravitational and kinetic energy (Heyer & Dame, 2015). The latter is often rephrased via the virial parameter

$$\alpha_{\mathrm{vir}} = \frac{5R\sigma_v^2}{GM}, \tag{1.12}$$

where $R = L/2$ is the cloud radius (see Section 1.4.3 for details). For self-gravitating clouds ($\alpha_{\mathrm{vir}} \gtrsim 2$ at $M \lesssim 10^5$ $\mathrm{M}_\odot$), one typically finds $\alpha_{\mathrm{vir}} \propto 1/\sqrt{M}$ both in the Milky Way and for extra-galactic clouds (see Chevance et al., 2022, and references therein).

1.3.3 Star formation

Stars are arguably the most fundamental components of galaxies. They are also important sources of energy to the engine that drives gas motions, and thereby galaxy evolution. That stars are a source of energy implies that stellar feedback processes play a fundamental role in regulating their own formation, and thus

star formation is often considered a self-regulating process (see, e.g., McKee & Ostriker, 2007; Agertz et al., 2013; Walch et al., 2015; Hopkins et al., 2018).

Star formation is observed to follow a relation with gas density, the so-called star formation relation or Schmidt-Kennicutt relation (after seminal work by Schmidt 1959; Kennicutt 1989). The original relation $\Sigma_{\rm SFR} \propto \Sigma_{\rm g}^{n}$, is typically found to scale with $n = 1.4$ (Kennicutt, 1998; Kennicutt & Evans, 2012), and was determined as a global trend with data points covering entire galaxies. When resolved spatially (i.e., with data points representing $\lesssim$ kpc patches in resolved galaxies), the relation shows more intricate behavior (see Figure 1.5). At surface densities $\Sigma_{\rm g} > 10\,{\rm M}_{\odot}\,{\rm pc}^{-2}$, the relation is roughly linear in log-space. The linear correlation disappears at low gas density, typically associated with the absence of molecular gas (see, e.g., Bigiel et al., 2008). Theories link this break in the relation to the density structure, nature of turbulence, and surrounding radiation field (see e.g., Schaye, 2004; Krumholz et al., 2009b; Ostriker et al., 2010; Renaud et al., 2012; Salim et al., 2015; Semenov et al., 2017). A class of galaxies called starbursts lies above the linear star formation relation. A separate trend appears at the lowest gas surface densities ($\Sigma_{\rm g} \lesssim 10\,{\rm M}_{\odot}\,{\rm pc}^{-2}$), in particular in irregular dwarf galaxies and the outskirts of spiral galaxies (see, e.g., Bigiel et al., 2010; Bolatto et al., 2011). The origin of this trend is discussed further in Paper II.

The linearity of the star formation relation can be summarized by the depletion time

$$t_{\rm dep} = \frac{\Sigma_{\rm g}}{\Sigma_{\rm SFR}} = \frac{M_{\rm g}}{\dot{M}_{\star}}, \tag{1.13}$$

which is the time to convert the entire gas reservoir into stars. Somewhat misleading, the inverse of depletion time can sometimes be referred to as the star formation efficiency; however, star formation is more appropriately thought of as *slow* and *fast* (see, e.g., Semenov et al., 2018; Renaud et al., 2019). In Figure 1.5, constant depletion time is indicated by diagonal dashed lines, where 100% would correspond to a complete conversion over a timescale of $t_{\rm dep} = 0.1\,{\rm Gyr}$. While the scatter of this parameter is small on galactic scales, cloud scales find significant scatter (see, e.g., Onodera et al. 2010; Leroy et al. 2013, as well as Paper II, Andersson et al. 2021).

On scales of GMCs, star formation is tightly linked to the lifetime and destruction of clouds. A first guess at this timescale is that of free fall collapse (i.e., cloud compression to a point under self-gravity) given by

$$f t_{\rm ff} = \sqrt{\frac{3\pi}{32 G \rho}} = 5.15 \left(\frac{\rho}{10^2\, m_p\, {\rm cm}^{-3}} \right)^{-1/2} {\rm Myr}, \tag{1.14}$$

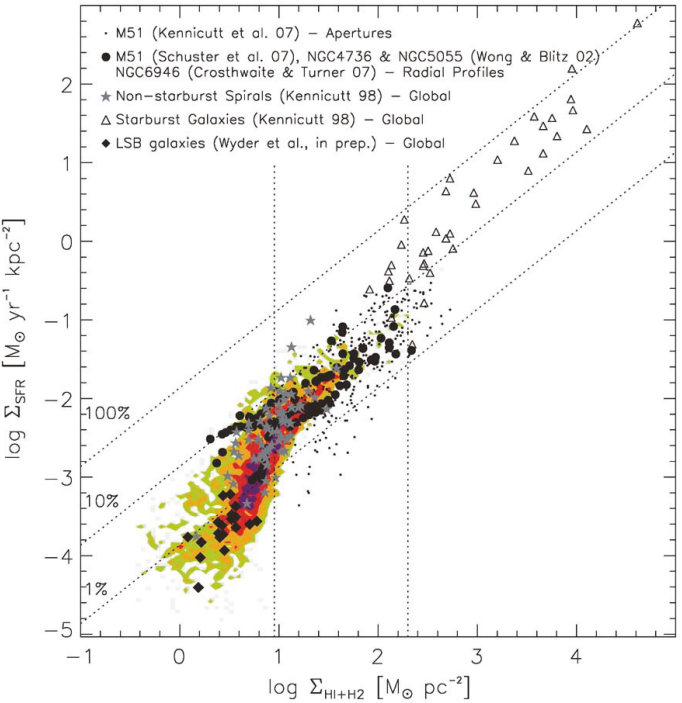

Figure 1.5: The star formation relation of galaxies, i.e., star formation rate surface density $\Sigma_{\rm SFR}$ plotted against gas surface density (in this case neutral and atomic hydrogen), $\Sigma_{\rm HI+H_2}$ The colored regions show the components derived in $750\,{\rm pc}$ wide ISM patches in nearby spiral and dwarf galaxies analyzed by Bigiel et al. (2008). Small black points show the components derived for different apertures (sizes of $0.5-2.5\,{\rm kpc}$) in the M51 galaxy, analyzed by Kennicutt et al. (2007). Large black points show data collected to study radial profiles in the M51, NGC4736, NGC5055, and NGC6946, studied by Wong & Blitz (2002); Crosthwaite & Turner (2007); Schuster et al. (2007). Grey stars and open triangles show global estimates of non-starburst and starburst galaxies, respectively, as studied by Kennicutt (1998). Filled diamonds show global estimates from low surface brightness galaxies studied by Wyder et al. (2009). The dotted sloped lines indicate constant depletion times of 0.1, 1, and $10\,{\rm Gyr}$ from top to bottom, denoted in the figure by its inverse (referred to as star formation efficiency, in this case assuming 100% conversion of gas to stars over a depletion time of $0.1\,{\rm Gyr}$, but see text for discussion). Figure adapted from Bigiel et al. (2008). © AAS. Reproduced with permission.

and represents a lower limit since this assumes a pressureless spherical cloud of gas. In reality, GMCs must have an internal pressure, particularly from thermal energy and the internal magnetic field. Nonetheless, the timescales for dissipation of the internal pressure are typically short compared to that of free-fall, and it is widely used to describe cloud collapse (see Chevance et al. (2022) for a comparison to the lifetime and dispersal time of GMCs).

Often Equations 1.14 and 1.13 are combined to what is often referred to as the efficiency per free-fall time,

$$\epsilon_{\rm ff} = \frac{\dot{M}_\star}{M/t_{\rm ff}}. \tag{1.15}$$

Although its scatter is debated, $\epsilon_{\rm ff}$ is found to have a median value of around 0.01 over a large range of densities, both observationally and in models (see, e.g., Krumholz & Tan, 2007; Grisdale et al., 2019; Chevance et al., 2022, and references therein). This low efficiency is one of the long-standing problems in star formation theory. In terms of depletion time, we can view star formation as a very slow process, with $\tau_{\rm dep} \sim$ few Gyr (see e.g., Bigiel et al., 2008, 2010; Leroy et al., 2013, 2015), which is several orders of magnitude longer than the timescales for collapse on the cloud scales (e.g., free-fall time $t_{\rm ff} \sim$ few Myr). This is the case even when only considering dense clouds of molecular hydrogen (see e.g., Krumholz & Tan, 2007; Evans et al., 2014; Lee et al., 2016).

The long depletion times relative to the rate at which molecular gas is converted into stars on the smallest scales (e.g., $\sim$ 360 Myr on 2 pc scale, Schruba et al. 2017) remains challenging to explain. Semenov et al. (2017) argued that a potential explanation is the small fraction of gas converted in a single star formation event, warranting a large number of such events. Combined with the relatively long time spent outside the star-forming phase, this implies that, if viewed globally, star formation is a slow process.

1.4 Hydrodynamical theory for galaxy evolution

The evolution of galaxies is largely driven by the accretion, ejection, and recycling of gas. The physics of fluid motion is therefore an integral part of galaxy theory. Gas behavior depends on cooling and heating, which sets the conditions for gas collapse and gravitationally induced instabilities. In addition, energy and momentum sources strongly affect gas motions. Stars formed as a consequence of gas collapse can play the role of energy providers, implying an intrinsic coupling between

cooling, heating, and gas motion. On a cosmological scale, interactions between galaxies (in particular galactic mergers) and the large-scale environment play an important role in galaxy evolution (see, e.g., Somerville & Davé, 2015; Naab & Ostriker, 2017). Note that cosmological aspects are not directly addressed in this thesis.

1.4.1 Gas motion and turbulence

The starting point for the theory of gas motion is the fluid equations, derived by taking the moments of the collisionless Boltzmann equation (also called the Vlasov equation). The zeroth moment results in an equation for mass conservation[7] (also known as the equation of continuity), which describes how mass inside an infinitesimal volume only changes via mass transfer in or out of the volume,

$$\frac{\partial \rho}{\partial t} = -\nabla \cdot (\rho \mathbf{v}), \tag{1.16}$$

where ρ is the gas mass density. The momentum evolution (first moment) of the volume includes some additional terms that are needed to account for forces and diffusion,

$$\frac{\partial (\rho \mathbf{v})}{\partial t} = -\nabla \cdot (\rho\, \mathbf{v} \otimes \mathbf{v}) - \nabla P - \rho \nu \nabla^2 \mathbf{v} - \rho \nabla \phi. \tag{1.17}$$

On the right-hand side, the first term describes momentum transport in or out of the volume (similarly to the continuity equation), and the second term the change in momentum due to forces by pressure P. The third term describes the redistribution of momentum to adjacent volumes through diffusion (commonly referred to as viscosity), for which we introduce the kinematic viscosity ν. This term can often be neglected in astrophysical applications concerning galaxy evolution (described later). The last term describes momentum change due to acceleration of the continuum, in this case via forces exerted by the gravitational field Φ.

[7] The collisionless Boltzmann equation is $\mathrm{D}f/\mathrm{D}t = \partial f/\partial t + \nabla f = 0$, where f is the distribution function of positions, velocities, and time. In general, the first two moments are number density $n = \int f \, \mathrm{d}u^3$ (zeroth moment), and momentum density $n\,\mathbf{v} = \int \mathbf{u}\, f \, \mathrm{d}u^3$ (first moment). In Equations 1.16 and 1.17, we introduce gas mass density because of its physical relevance to gravitation forces. Note that the velocity $\mathbf{u}$ refers to a single velocity in the distribution function, which is distinguished from the fluid bulk motion $\mathbf{v}$ (obtained by integrating over the entire velocity space). I will use $\mathbf{v}$ throughout this thesis, leaving u for other purposes.

On the form written in Equations 1.16 and 1.17 (i.e., when considering non-zero diffusion terms), these are known as the Navier-Stokes equations and completely describe the flow of incompressible, isotropic, and homogeneous fluids.[8] Note that in Chapter 2, we will introduce an equation for energy as well, which we simplify by neglecting diffusion (in this case, the equations become the Euler equations).

Note that Equations 1.16 and 1.17 only describe the zeroth and first moments of velocity and are not a closed set of equations (even if introducing an energy equation). These equations do not provide much insight into physical problems unless we introduce some physically constrained closure relation. For astrophysical purposes, the ideal gas law serves this purpose and is given by

$$P = \frac{\rho k_{\mathrm{B}} T}{\mu m}, \tag{1.18}$$

where k_{B} is the Boltzmann constant, T is temperature, μ is mean molecular weight, and m_{p} is the mass on the particle of interest (in our case the mass of a hydrogen atom). We frequently encounter another parameter, namely the speed of sound c_s, at which waves propagate through a given medium. We can find an expression of this quantity by considering the one-dimensional case of a wave propagating through a fluid in a steady flow. First, conservation of mass implies that mass entering and leaving a small volume in the flow must be the same (i.e., $\rho\, v = (\rho + \mathrm{d}\rho)(v + \mathrm{d}v) \approx \rho\, v + \rho\, \mathrm{d}v + v\, \mathrm{d}\rho$, approximating $\mathrm{d}\rho\, \mathrm{d}v \approx 0$). In this case, we approximate $v\mathrm{d}\rho = -\rho \mathrm{d}v$, i.e, constant mass flux through some cross-section. Taking the gradient of fluid pressure to be a force, classical mechanics (Newton's second law) gives

$$\frac{\mathrm{d}v}{\mathrm{d}t} = -\frac{1}{\rho}\frac{\mathrm{d}P}{\mathrm{d}x} \Rightarrow \mathrm{d}P \approx (-\rho\, \mathrm{d}v)\frac{\mathrm{d}x}{\mathrm{d}t} \tag{1.19}$$

or

$$\frac{\mathrm{d}P}{\mathrm{d}\rho} \approx v^2. \tag{1.20}$$

By definition, the velocity in question is the sound speed c_s. Although this is not true in general (for example, we have assumed an isentropic system), it is a good approximation for most applications. Furthermore, from Equation 1.18, we

[8] Finding proof for the existence of smooth, non-singular solutions to this equation is awarded \$1 000 000, as part of the Millenium Prize Problem set by the Clay Mathematics Institute, USA.

obtain the useful relation

$$c_s = \sqrt{\frac{k_{\rm B}T}{\mu m_p}} = \sqrt{\frac{P}{\rho}}. \tag{1.21}$$

To understand some properties of fluid evolution, we can study the Navier-Stokes equations using the relation we found for the sound speed and some characteristic scales denoted ℓ for length and u for velocity (implying characteristic timescale ℓ/u). By neglecting gravitational forces and rewriting Equation 1.17 in terms of these scales, we obtain the following dimensionality relation:

$$\frac{\rho u^2}{\ell} = \frac{\rho u^2}{\ell} - \frac{\rho c_s^2}{\ell} - \frac{\rho \nu\, u}{\ell^2} = \frac{\rho u^2}{\ell}\left(1 - \frac{c_s^2}{u^2} - \frac{\nu}{\ell u}\right). \tag{1.22}$$

In view of this relation, we define two important dimensionless quantities,

$$\mathcal{M} \equiv \frac{u}{c_s}, \quad \mathrm{Re} \equiv \frac{\ell u}{\nu}, \tag{1.23}$$

where $\mathcal{M}$ is called the Mach number, and Re is called the Reynolds number. The Mach number determines whether the fluid is in a supersonic ($\mathcal{M} > 1$) or subsonic state ($\mathcal{M} < 1$). In an astrophysical context, the Mach number is typically used to describe internal cloud motion and is particularly useful for studying turbulence and shock propagation. The Reynolds number describes the ratio between viscous and inertial forces. This number distinguishes between laminar and turbulent flows.

Finally, we can look at the typical values of these quantities in the ISM. As mentioned earlier, GMCs have densities $\rho_{\rm H_2} \sim 10^2\ \mathrm{cm}^{-3}$, and temperatures $T \sim 10\,\mathrm{K}$. If we assume the cloud to consist purely molecular hydrogen ($\mu = 2$), then we find

$$c_s \simeq 0.2\sqrt{\frac{T}{10\,\mathrm{K}}}\,\mathrm{km\,s^{-1}}. \tag{GMC}$$

Along with the Larson (1981) scaling relations, we find that $\mathcal{M}$ is in the range 10 to 30, implying that motions in the clouds are highly supersonic. For typical values of the ionized ISM ($\mu = 0.5$), we find

$$c_s \simeq 6\sqrt{\frac{T}{10^4\,\mathrm{K}}}\,\mathrm{km\,s^{-1}}. \tag{ISM}$$

Note that while the thermal sound speed of the ISM is high compared to that of GMCs, the ISM is highly prone to shocks from, e.g., stellar ejecta, particularly in

regions of star formation. To get an estimate for the Reynolds number, we take the kinetic viscosity of ideal gas, which is on the order of $\nu \sim c_s \lambda$, where λ is the mean free path of the particles in the fluid. Approximating the mean free path as the inverse of density times particle cross-section ($\sim$ nm), we get $\lambda \sim 10^{12}$ cm and

$$\mathrm{Re} \sim \frac{\ell u}{\lambda c_s} = \frac{\ell}{\lambda}\mathcal{M} \sim 10^9, \tag{1.24}$$

implying that viscous forces can be neglected and that the ISM is highly turbulent. Notably, this goes hand-in-hand with the turbulent velocity structure ($\sigma_v \propto R^{\text{constant}}$) mentioned in Section 1.3.2. Another point to note is that because viscous forces are negligible, the equations for fluid motion reduce to the Euler equations (described in Section 2.2.2).

1.4.2 Cooling and heating

For gas to contract and eventually turn into stars requires that the gas cools, while heating inhibits this process. In this way, cooling and heating work in tandem to create a multi-phase medium that makes up, e.g., the ISM. Cooling is mainly driven by radiative processes, while heating comes through various processes, e.g., ambient starlight, cosmic rays, gas compression, and friction, as well as transient processes, such as stellar or black hole feedback. In this section, I will describe microscopic processes that provide the net cooling rate of the gas. Stellar feedback is described in Section 1.5.3 while black hole feedback is not considered in this thesis.[9]

The radiative processes important for cooling ($\mathscr{L}$) can broadly be divided into free-free emission (Bremsstrahlung), recombination, as well as, collisional ionization, and excitation.[10] If these processes generate a photon that can escape the gas, this results in a loss of energy, which in turn causes the gas to cool. Therefore, the magnitude of the cooling rate depends on several factors: 1) high frequency of photon emission (i.e., the abundance of events with a high probability of photon emission); 2) emitted photons have energy that is comparable to or in excess of

[9] Feedback from super-massive black holes is linked to active galactic nuclei and plays an important role in truncating the high mass end of the galaxy mass spectrum. The interested reader likely finds Mo et al. (2010) to be a good starting point for studying this.

[10] Compton scattering plays some role, in particular for the CMB as a radiation source at high redshift. Compton cooling becomes important if the photons of the background radiation field can exchange energy with electrons in the gas, provided that $T_\gamma \gg T_\mathrm{e}$, i.e., the temperature of the radiation field is much higher than the temperature of the electrons in the gas. In this case, electrons lose energy to the radiation field.

the thermal energy; 3) photons can escape the gas (i.e., radiation for which the gas is optically thin). These factors make the cooling rate sensitive to temperature. At high temperatures ($\gtrsim 10^7$ K), electrons accelerated by charged particles frequently emit high-energy photons, making Bremsstrahlung the dominant coolant. At temperatures in the range 10^5 K to 10^6 K, collisional processes and recombination at resonance lines are frequent, with principal species being Fe, Ne, and Si. At $\lesssim 10^5$ K, C and O are the dominant coolants, e.g., via resonance line emission. Although H is the most abundant element, it only plays a dominant role around 10^4 K because transitions from the ground state of hydrogen are highly energetic (13.6 eV to continuum). At temperatures of $\sim 10^3$ K, cooling is instead dominated by meta-stable ions (e.g. Fe^+,Si^+).

In cold gas ($T \lesssim 10^2$), molecules become highly important for cooling, the most important being H_2 and CO. H_2 is the most abundant molecule; however, it has no dipole moment, implying that rotational transitions are forbidden, and radiation leaks out very slowly. Unlike this, rotational transitions are allowed for the CO molecule, although CO is far less abundant compared to H_2. Nonetheless, radiation via the CO molecule is the dominant coolant at ~ 10 K.

Radiation from sources external to the gas in question (as well as radiation that cannot escape the gas) will act as a source of heating ($\mathscr{H}$). The primary source is ionizing radiation from starlight, often modeled as a background heating source (see, e.g., Haardt & Madau, 1996). This is particularly important for re-ionizing the Universe at $z \sim 6$ (see Robertson, 2021, for a review). In addition, cosmic rays and X-rays can also ionize hydrogen, making them important sources for heating. Finally, the photoelectric effect can cause electrons to be released from dust grains that add energy to the gas, which probably makes them the dominant heating source in neutral clouds (Dyson & Williams, 1997).

Because cooling and heating are highly complex, studying these processes is itself a field of research, even within an astrophysical context. Treating these processes in numerical galaxy simulations is therefore often done via a cooling function, with the volumetric net cooling rate given by

$$\Lambda(T) = \frac{\mathscr{L} + \mathscr{H}}{n_{\rm H}^2}, \tag{1.25}$$

where $n_{\rm H}$ is the number density of hydrogen. Typically, $\Lambda(T)$ is evaluated by interpolating a pre-computed table of rates. An example of this is given in Figure 1.6. The rates of cooling and heating are provided in libraries or numerical codes, common examples being Cloudy (Ferland et al., 1998) and GRACKLE (Smith et al., 2017).

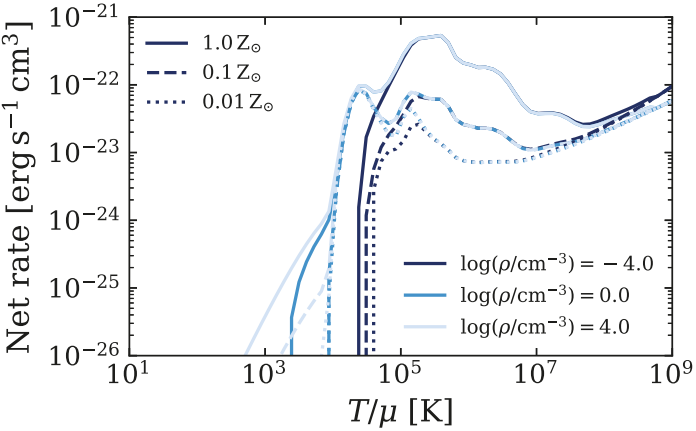

Figure 1.6: Net cooling rate $\Lambda(T)$ as a function of temperature for a few examples of densities and metallicities, as indicated by the legends. The rates shown are combinations of the rated provided by Sutherland & Dopita (1993) for $T > 10^4$ K, and Rosen & Bregman (1995) for lower temperatures. Note that this cooling function is that implemented in the Ramses hydrodynamics code (Teyssier, 2002).

Without an energy supply, gas will cool down, and thermal support will diminish. Thermal pressure balances the gravitational forces. Cooling, therefore, leads to gas contraction. A way to quantify this process is by the cooling time, typically given as

$$t_{\rm cool} = \frac{\rho e}{n_{\rm H}^2 \, \Lambda(T)}, \tag{1.26}$$

where e is the internal thermal energy of the gas. Assuming an ideal mono-atomic gas (adiabatic index $\gamma = 5/3$), we can estimate some order-of-magnitude estimations for different parts of the gaseous galaxy,

$$t_{\rm cool} = \frac{3k_{\rm B}}{2\beta^2} \frac{T}{n\Lambda(T)} \tag{1.27}$$

$$\simeq 0.03\,{\rm Myr} \left(\frac{T}{10^4\,{\rm K}}\right) \left(\frac{n}{10^{-1}\,{\rm cm}^{-3}}\right)^{-1} \left(\frac{\Lambda(T)}{10^{-22}\,{\rm erg\,s^{-1}\,cm^3}}\right)^{-1} \quad ({\rm ISM})$$

$$\simeq 3.21\,{\rm Gyr} \left(\frac{T}{10^6\,{\rm K}}\right) \left(\frac{n}{10^{-3}\,{\rm cm}^{-3}}\right)^{-1} \left(\frac{\Lambda(T)}{10^{-23}\,{\rm erg\,s^{-1}\,cm^3}}\right)^{-1}, \quad ({\rm CGM})$$

where I defined $\beta = n/n_{\rm H}$ ($= 4/9$, for fully ionized gas of primordial composition), as well as a the conversion $n = \rho/\mu m_p$. Notably, the cooling times of the ISM and CGM are vastly different (5 orders of magnitude). Furthermore, the timescale for collapse on small scales is dominated by the free-fall timescale (Equation1.14).

1.4.3 Gas collapse and instabilities

A fundamental aspect of gas dynamics is understanding how the gas behaves under gravitational forces, in particular, the stability criterion that governs whether gas can collapse or not. Theoretical studies of this stability often use the virial theorem or Jeans stability analysis[11]. Following the notes from Krumholz (2015), the virial theorem can be stated

$$\frac{1}{2}\ddot{I} = 2\left(\mathcal{T} - \mathcal{T}_S\right) + \mathcal{B} + \mathcal{W}, \tag{1.28}$$

where I is the mass distribution

$$I = 4\pi \int \rho r^2 \, \mathrm{d}r. \tag{1.29}$$

The left-hand side of Equation 1.28 is written in terms of energy, denoting the kinetic and thermal energy $\mathcal{T}$, the thermal and ram pressure energy $\mathcal{T}_S$ which flows through the surface S of the cloud, the net magnetic energy $\mathcal{B}$ between the internal and external magnetic forces, and finally the gravitational energy $\mathcal{W}$ which accounts for both the internal and external gravitational field. Note that the virial theorem on this form assumes that the cloud mass is conserved, i.e., no gas flows through its surface boundary, and on this boundary, the magnetic field is constant. This idealized set-up provides good physical insight into the system. Firstly, it concerns the acceleration of the mass distribution; hence, the resulting sign on the left-hand side of Equation 1.28 determines whether the cloud contracts or expands. Secondly, an expression for the virial parameter $\alpha_{\rm vir}$ is trivially obtained from this theorem. Since this parameter describes the balance between gravitational forces and thermal plus turbulent forces, we neglect forces from the surface and magnetic field on the left-hand side, which gives

$$\alpha_{\rm vir} \equiv \frac{2\mathcal{T}}{|\mathcal{W}|}. \tag{1.30}$$

[11] Named after James Jeans for his early theoretical study of collapsing spherical nebulae (Jeans, 1902)

For example, in the case of an isolated, uniform, and isothermal cloud, we have

$$\mathcal{T} = \frac{3}{2} M c_s^2, \quad \mathcal{W} = -\frac{3GM^2}{5R}, \tag{1.31}$$

which gives the virial parameter as in Equation 1.12.

Equation 1.28 can also provide a first approximation to the importance of the magnetic field by comparing the magnetic and gravitational terms. As such, a cloud in magneto-static equilibrium obeys $\mathcal{B} = |\mathcal{W}|$. Approximating the magnetic energy to be given by the magnetic flux Φ passing through the magnetized cloud ($\mathcal{B} \approx \Phi^2/6\pi^2 R$, see, e.g., Krumholz 2015 for details), one can find a critical mass via the expression for $\mathcal{W}$ in Equation 1.31:

$$M_B = \sqrt{\frac{5}{2\pi G}}\Phi \approx 1560 \left(\frac{\bar{B}}{30\mu\mathrm{G}}\right)\left(\frac{R}{\mathrm{pc}}\right)^2 \mathrm{M}_\odot, \tag{1.32}$$

where the mass is expressed in terms of the mean magnetic field strength $\bar{B}$ and cloud size R. This mass determines whether the cloud is supercritical ($M > M_B$) or subcritical ($M < M_B$). Clouds that are supercritical can collapse under self-gravity (i.e., the magnetic field cannot halt the gravitational acceleration); however, for subcritical clouds, the magnetic field strength grows as it is confined to smaller radii, eventually forcing the collapse to come to a halt, unless the field changes (through, e.g., ambipolar diffusion). Observations typically find the ISM to be highly magnetized; however, the behavior of the magnetic field on small scales is not well understood, and there is still debate regarding its role in star formation (Crutcher, 2012; Li et al., 2014).

The Jeans theory involves a stability analysis of the fluid equations (Equations 1.16 & 1.17, neglecting the viscosity term), accounting for gravity via the Poisson equation

$$\nabla^2 \phi = 4\pi G \rho. \tag{1.33}$$

To arrive at a solution, one applies a perturbation of a single Fourier mode in density and velocity to an infinite, uniform, and isothermal density field[12] (i.e. $\rho = \rho_0 + \epsilon\rho_a \exp[i(kx - \omega t)]$, where $\epsilon \ll 1$ introduces a small perturbation with initial amplitude ρ_a, and spatial (temporal) frequency k (ω) to background

[12]Note that this is an erroneous assumption (often called the "Jeans swindle") since the Poisson equation cannot be solved for a non-zero infinite density field. Nonetheless, the solution is still approximately correct and other mathematically consistent derivations exists (see e.g., Binney & Tremaine, 2008)

density ρ_0, and similarly for $v = v_0 + \epsilon v_a \exp[i(kx - \omega t)]$). Considering only perturbations along one dimension, and neglecting all terms ϵ^2, algebraic manipulation of the mass and momentum equations leads to the dispersion relation

$$\omega^2 = c_s^2 k^2 - 4\pi G \rho_0. \tag{1.34}$$

In cases when the left-hand side of this relation is negative (small values k, i.e., perturbations on large spatial scales), ω has imaginary roots, and perturbations can grow infinitely. The spatial scale at which such instabilities can start to form ($\omega = 0$) is called the Jeans length

$$\begin{aligned} \lambda_J &= \frac{2\pi}{k_J} = \frac{2\pi c_s}{\sqrt{4\pi G \rho_0}} \\ &= 3.44 \left(\frac{c_s}{0.2\,\mathrm{km\,s^{-1}}} \right) \left(\frac{\rho_0}{10^2\, m_p\,\mathrm{cm^{-3}}} \right)^{-1/2} \mathrm{pc}, \end{aligned} \tag{1.35}$$

with the last equivalence given in terms of values typical for GMCs. Since this is much smaller than the spatial scales of GMCs (see Section 1.3.2 for details), the thermal pressure cannot support such clouds against collapse by self-gravity. The result is a highly fragmented and turbulent ISM, which links back to the Larsson relation ($\sigma_v \propto R^{\text{constant}}$). The Jeans stability criterion is commonly used to distinguish star-forming gas in numerical models (see, e.g., Lahén et al., 2020; Smith et al., 2021; Hislop et al., 2022).

1.5 The formation and evolution of stars

Thermonuclear reactions triggered by pressure from self-gravity are the distinguishing factor when we define what stars are. In the context of galaxy theory, evolving stars provide chemically enriched material, momentum, and energy in the form of radiation, stellar winds, and explosive ejection via supernovae (SNe). Due to the cyclic nature of interactions between gas and stars (implied by birth, evolution, and death of stars), these processes are referred to as stellar feedback.

1.5.1 Star formation

The small-scale physics that determines the processes which turn dense gas cores in GMCs into proto-stars is still not fully understood (Krause et al., 2020). Nonetheless, modern numerical experiments have progressed significantly (see e.g., Haugbølle et al., 2018; Grudić et al., 2021; Pelkonen et al., 2021), and are commonly

used to study for example the origin of the initial mass function (Guszejnov et al., 2021, 2022b), or early star cluster dynamics (Guszejnov et al., 2022a). Of particular interest are the effects of early stellar feedback (radiation and bipolar jets), the transition between the GMC core mass function, and the shape and temporal build-up of the initial mass function.

For modeling purposes, we can arrive at a useful theoretical framework for star formation by considering the efficiency per free-fall time (Equation 1.15) and make the following ansatz (see Schmidt, 1959; Katz, 1992):

$$\dot{\rho}_\star = \epsilon_{\rm ff} \frac{\rho_{\rm g}}{t_{\rm ff}}, \tag{1.36}$$

where $\dot{\rho}_\star$ is the time derivative of the stellar mass density (i.e., a star formation rate density). Keep in mind that $t_{\rm ff}$ (as given by Equation 1.14) has a scale dependence. Furthermore, because Equation1.36 relies on the free-fall stage of gas collapse, it is only applicable above some density threshold. Also note that since $t_{\rm ff} \propto \rho_{\rm g}^{-0.5}$, it follows that $\dot{\rho}_\star \propto \rho^{1.5}$.

To determine the density threshold where Equation 1.36 is applicable, as well as a value for the parameter $\epsilon_{\rm ff}$, is not trivial. One approach is to make an educated guess and compare the outcome with empirical data. This is particularly useful in the Kennicutt-Schmidt formalism, as it original motivated of Equation 1.36 (see Hennebelle & Chabrier, 2011; Padoan & Nordlund, 2011; Renaud et al., 2012, for examples studies of this nature). Section 1.3.3 highlighted the inefficiency of star formation ($\epsilon_{\rm ff} \sim 0.01$). Note that when applied in hydrodynamical simulations, the feedback regulation makes the star formation rate somewhat insensitive to this choice (see, e.g., Grisdale et al., 2017; Hislop et al., 2022), although the numerical method plays a role (Hu et al., 2022). Another approach, suggested by Padoan et al. (2012), is to assume $\epsilon_{\rm ff}$ to scale with Mach number and density, which is particularly important in the cosmological context since the distribution of densities and level of turbulence is affected by, e.g., galactic mergers (Renaud et al., 2014), and hence evolves with redshift (Segovia Otero et al., 2022).

The threshold for star formation is more challenging to estimate empirically, particularly since the 3D density of the gas is not directly observable. For an initial guess to this threshold, we use the Jeans length (described in Section 1.4.3) to derive the density when gas is prone to gravitational instability on some scale. Written as the background density in Equation 1.35, this gives

$$\rho_0 = 1.2 \times 10^3 \left(\frac{c_s}{0.2\,{\rm km\,s^{-1}}} \right)^2 \left(\frac{\lambda_J}{\rm pc} \right)^2 m_p\,{\rm cm^{-3}}. \tag{1.37}$$

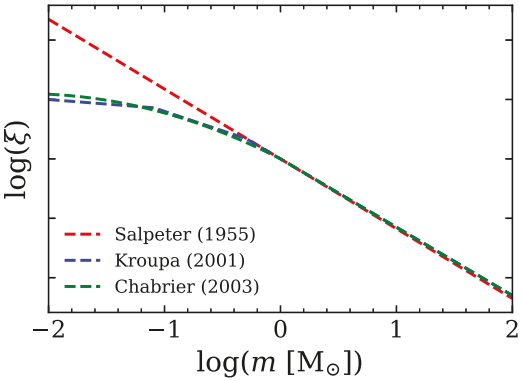

Figure 1.7: Examples of empirically derived initial mass functions, all normalized to have equal ξ at $m = 1\ \mathrm{M}_\odot$. See the main text for details about the different functions (with reference denoted in the legend).

Since numerical simulations work at a given spatial and mass resolution, this threshold can be adapted accordingly.

1.5.2 The initial mass function

The stellar mass sets the gravitational force, which determines the rate of the nuclear processes in the stellar interior. These processes are highly sensitive to temperature (and consequently pressure), making stellar mass an important factor for stellar evolution. For example, the lifespan of individual stars is a heavily dependent function on their mass (massive stars evolve very rapidly compared to those with low mass, see Section 1.5.3 for details). From the perspective of a population, this translates into a stellar mass function, the shape of which evolves rapidly (especially in the early stages of evolution). Therefore, the initial mass function (IMF) is challenging to constrain empirically (observations are limited to young stellar populations). There is also a debate regarding the universality of the IMF (see, e.g., Bastian et al., 2010; Kroupa et al., 2013), in particular with regards to metallicity (see, e.g., Geha et al., 2013; Liang et al., 2021; Prgomet et al., 2022) and environment (see, e.g., Smith, 2020).

Despite the observational challenge, the IMF was assigned the shape of an inverse power-law early on (Salpeter, 1955), a notion which remains valid even today, although with a modification to a shallower slope at lower masses (Kroupa et al., 1993). Therefore, the functional form of the IMF is typically defined as a

split power law:

$$\xi(m) = AC_i m^{-\alpha}, \quad m_i \leq m \leq m_{i+1}, \tag{1.38}$$

where A is a normalizing constant, C_i is a constant which ensures a continues slope, and α_i is the slope in the mass range m_i to m_{i+1}. Except for the original fit by Salpeter (1955), which takes $\alpha = 2.35$ over the entire mass range, the most common examples of IMFs are the one by Kroupa (2001), and Chabrier (2003). Taking an entirely empirical approach, Kroupa (2001) fitted the mass function to three mass ranges: $\alpha_0 = 0.3$ for $0.01 \leq m \leq 0.08\,\mathrm{M}_\odot$; $\alpha_0 = 1.3$ for $0.08 \leq m \leq 0.5\,\mathrm{M}_\odot$; $\alpha_0 = 2.3$ for $m \geq 0.5\,\mathrm{M}_\odot$. Chabrier (2003) instead argued that, if the formation of a coeval stellar population can be considered a process where mass is determined by the product of independent variables, then the central limit theorem states that the logarithm of the mass follows a log-normal distribution (see also Miller & Scalo, 1979; Zinnecker, 1984). Realizing this fits the low-mass, Chabrier invoked a split function with

$$\xi(\log m) = A \exp\left(-\frac{(\log m - \log m_*)^2}{2\sigma_*^2}\right), \quad m \leq 1\,\mathrm{M}_\odot, \tag{1.39}$$

where A is a normalizing constant, $\log m_*$ is the distribution's mean value, and σ_*^2 is its variance. For $m \geq 1\,\mathrm{M}_\odot$, the Chabrier IMF takes the form of Equation 1.38, with $\alpha = 2.3$. Figure1.7 show these three IMFs. Note that the Kroupa and Chabrier IMFs, are almost indistinguishable.

1.5.3 Stellar evolution and feedback

The evolution of a star is determined by an interplay between the pressure generated by self-gravity and that from internal thermonuclear reactions. The role played by self-gravity makes initial stellar mass important. The thermonuclear reactions that take place change throughout the lifetime of a given star, since the fuel used is altered by these reactions. Traditionally, this is studied in one-dimensional geometry, assuming spherical symmetry and hydrostatic equilibrium (Kippenhahn et al., 2013).

Briefly described, a star evolves through many distinct phases: proto-star (or pre-main sequence), main-sequence, sub-giant branch, red giant branch (RGB), horizontal branch, asymptotic giant branch (AGB), post-AGB phase, and super giant phase. Depending on mass, different processes ensue throughout these phases, and not all stars go through all of them. Stellar evolutionary tracks are typically

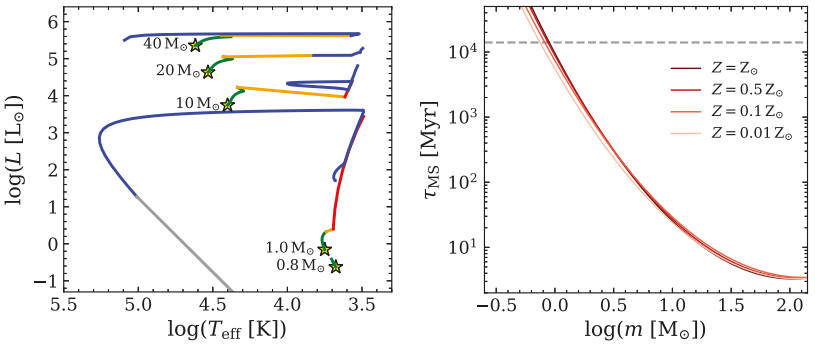

Figure 1.8: *Left:* Evolutionary track of stars at solar metallicity shown in the Hertzsprung–Russell diagram, i.e., stellar luminosity versus effective temperature. Star symbols indicate the starting point, the main sequence indicated in green, with the Hertzsprung gap (orange) separating it from the red giant phase (red). Blue solid lines indicate core helium burning, the first and second asymptotic giant branches. The grey line shows the white dwarf sequence. Tracks computed using the Single Stellar Evolution code by Hurley et al. (2000). *Right:* Main sequence lifetime shown as a function of initial stellar mass, with colors indicating different metallicities. The gray dashed line shows the current age of the Universe. The main sequence lifetime is calculated from the fitting function by Raiteri et al. (1996).

described in the Hertzsprung–Russell diagram. An example of evolutionary tracks for different stellar masses in this diagram is shown to the left in Figure 1.8. The main sequence is marked by hydrogen first fusing into deuterium and then helium via the proton-proton chain. When the core is exhausted of hydrogen, further burning takes place in shells, and the star quickly expands radially, resulting in rapid evolution to the RGB (this rapid evolution appears as a decrease in effective temperature, the so-called Hertzsprung gap). During the RGB, the helium core grows, and some core material is brought up to the surface via convection (first dredge-up). Low- to intermediate-mass stars ($0.6 - 2\,\mathrm{M}_\odot$) have electron degeneracy supported cores, and helium ignites explosively (helium flash), resulting in a significant loss of energy generation. The evolution stalls here, creating a horizontal branch in the Hertzsprung–Russell diagram. After this, stars enter the AGB phase, where the nucleosynthesis of helium from hydrogen proceeds in shells around the core. These reactions result in periodic supplies of helium fuel to the core, triggering thermal pulses, which result in the ejection of material (i.e., stellar wind). For low- to intermediate-mass stars, this eventually leads to the com-

plete stripping of the stellar envelope, revealing the core, which remains as a white dwarf. More massive stars have gravitational fields strong enough to trigger nucleosynthesis of heavier elements (in particular, via the carbon-nitrogen-oxygen cycle). Finally, these stars end their lives through disruptive events, e.g., SNe (resulting in neutron stars, black holes, the complete disruption of the stars, or in more exotic objects, such as naked helium stars.

Of particular interest are SNe, as they are one of the most impactful sources of stellar feedback. Observationally, these transient events are primarily studied via spectral time series and are therefore typically classified by their light curves and spectral features, e.g., SNe type I and type II are distinguished by whether hydrogen lines are visible (type II) or not (type I). Additional sub-classification further split SNe into different groups (see Turatto, 2003, for a review). From a theoretical perspective, an important distinction is whether the explosion has a thermonuclear origin (e.g., the case of type Ia) or is triggered by a core collapse in massive stars (e.g., the case of type II). Mechanisms for core-collapse explosions are detailed in the reviews by Woosley & Bloom (2006); Janka (2012). Core-collapse SNe are typically assumed to be triggered in stars more massive than $8\,\mathrm{M}_\odot$, while thermonuclear explosions are triggered by mass transfer to white dwarfs. The energy released in both these events is $\sim 10^{51}$ erg (Janka, 2012).

It is worthwhile to note that multiplicity in stellar systems (in particular, tight binary stars) plays a role in stellar evolution. The details are beyond the scope of this thesis, and I refer to the work by, e.g., Hurley et al. (2002); Izzard et al. (2006); Eldridge et al. (2008); Eldridge & Stanway (2009) for a deeper discussion.

1.5.4 Natal stellar clusters and runaway stars

Since stars originate from the fragmented collapse of GMCs, young stars are highly clustered (Lada & Lada, 2003; Portegies Zwart et al., 2010). These stars eventually disperse throughout the galaxy by scattering as a result of interactions with, e.g., resonances, spiral arms, GMCs, and star clusters (see, e.g., Sellwood & Binney, 2002; Binney & Tremaine, 2008; Kokaia & Davies, 2019; Mikkola et al., 2020); however, the most massive stars are expected to remain clustered for the majority of their lives (see, e.g., Parker & Goodwin, 2007). The clustering of massive stars (responsible for the majority of energy input) strongly affects the nature of stellar feedback, as it allows feedback-driven bubbles to build up and break out of the ISM (Keller et al., 2014, 2016; Gentry et al., 2017, 2019), channeling energy directly into the CGM (Li & Bryan, 2020).

Nonetheless, there is ample evidence of massive stars outside clusters (see e.g.,

Parker & Goodwin, 2007; Bressert et al., 2012), some of which could have formed in isolation (Krumholz et al., 2009a; Oey et al., 2013; Lamb et al., 2016). In particular, many O and B type stars ($> 2\ M_{\odot}$) travel at high velocities compared to the surrounding stars (so-called runaway stars; see early work by Blaauw 1961; Poveda et al. 1967; Gies & Bolton 1986; Gies 1987; Stone 1991)

The fraction of runaway stars (defined as stars having high peculiar velocities $v_{\rm pec}$) has been highly debated throughout the years. In early work considering O-type stars in the field of the Milky Way, Blaauw (1961) found 21% of stars with $v_{\rm pec} > 40\,{\rm km\,s^{-1}}$, while Stone (1979) found 49% (however, note critique by Gies & Bolton 1986). Later, Stone (1991) updated their claim, applying statistical arguments to account for completeness and arrived at 46% O type runaways. In de Wit et al. (2005), they found that as many as 51% of field O stars have $v_{\rm pec} > 40\,{\rm km\,s^{-1}}$. In the Small Magellanic Cloud, Lamb et al. (2016) found a lower limit at $\sim$ 11% field runaway O stars. In a more recent study using Gaia DR1 (Gaia Collaboration et al., 2016), Maíz Apellániz et al. (2018) found the runaway fraction to be 5.7% (note that accounting for incompleteness likely increases this to $\sim$ 12%, see Tetzlaff et al. 2011). Furthermore, Drew et al. (2021) estimated at least 10% of O stars in Gaia EDR3 (Gaia Collaboration et al., 2021) are runaway stars.

There are currently two different scenarios that explain the origin of runaway stars. The original explanation by Blaauw (1961) suggests that if the primary (most massive) star in a binary system explodes in a supernova, the immediate mass loss from the system can result in a binary breakup, which causes the secondary to escape at high velocity (binary scenario). This scenario implies a stringent time constraint on the first ejection, namely the main sequence lifetime ($\sim 4\,{\rm Myr}$) of the most massive star in a binary system. Furthermore, this results in fairly low fraction of runaway stars ($\sim$ 10%, see e.g. Eldridge et al., 2011; Renzo et al., 2019). The second scenario suggests that velocity kicks are imposed on stars via close dynamical interactions between multiple objects in dense clusters (Poveda et al., 1967). Compared to the binary scenario, the dynamical origin does not impose constraints on the ejection timescale, although it must depend on the occurrence rate for multi-body interactions. In numerical simulations by Oh & Kroupa (2016), the fraction of runaway stars were found to be sensitive to the initial density of the cluster, with up to 30% runaway stars in the most favorable case. Notably, the velocity distribution they found follows an inverse power-law[13].

[13]The resulting distribution is used to model runaway stars in Papers I, II, and III. I describe this in more detail in Section 2.3.2

1.6 The impact of stellar feedback on galaxy evolution

As described in Section 1.5, stars subject their surrounding to feedback. This process significantly affects the evolution of gas, in particular in regions with ongoing star formation. One such region is 30 Doradus, shown in Figure 1.9. In this region, radiation from newly formed stars illuminates the surrounding medium, creating pockets of highly ionized X-ray emitting gas (appearing as blue in Figure 1.9). The gas in these regions has an extremely high temperature ($\sim 10^7$ K), caused by shock-heating from stellar winds and SNe. These pockets disrupt the original GMC, creating a complex and highly fragmented cloud. In Figure 1.9, the cold ($\lesssim 10^4$ K) gas that remains is seen in infrared light (red) and Hα emitting hydrogen gas (combined with photometric V-band data and shown in green). For more information, see Walborn et al. (2002); Townsley et al. (2006).

The inclusion of feedback to regulate the accumulation of gas and effectively the star formation rate of galaxies is one of the major successes for galaxy modeling in the past decades (see seminal work by, e.g., McKee & Ostriker 1977; Dekel & Silk 1986; Katz 1992; Murray et al. 2005, or reviews by Somerville & Davé 2015; Naab & Ostriker 2017). However, many details regarding feedback are still debated (Naab & Ostriker, 2017), in particular how mass, energy, and metals are transported by galactic winds (see e.g., Veilleux et al., 2005, 2020; Fielding et al., 2017; Schroetter et al., 2019). Exploring some aspects of this is the main focus of Papers I and III. In Section 1.6.1, I provide an update on the current state of this field. The loading factors are of particular interest since these estimate how efficiently the wind transports the various quantities.

1.6.1 Galactic winds

Galactic winds are ubiquitous in star-forming galaxies and are typically observed as conical flows of material that leave the galactic disc. The archetypal example is the bipolar outflow expelled from the star-bursting galaxy Messier 82 (see, e.g., Lynds & Sandage, 1963; Shopbell & Bland-Hawthorn, 1998; Leroy et al., 2015), clearly observable in infra-red, optical, and X-ray. Theoretically, outflows are a natural outcome of feedback processes in the ISM.

Winds from galaxies of different masses are often compared using the loading factor. Mass loading is defined by

$$\eta_M = \frac{\dot{M}_{\rm wind}}{\rm SFR}, \tag{1.40}$$

Figure 1.9: Composite image of the Tarantula Nebula (30 Doradus), an active star formation region in the Large Magellanic Cloud. Blue shows X-ray emission captured by Chandra X-ray Observatory, green shows optical light captured by the Hubble Space Telescope, and red shows infrared captured by the Spitzer Space Telescope. Image from public domain. Credit: X-ray: NASA/CXC/PSU/L.Townsley et al.; Optical: NASA/STScI; Infrared: NASA/JPL/PSU/L.Townsley et al.

which is a unit-less quantity comparing the outflow rate $\dot{M}_{\rm wind}$, and the star formation rate SFR. Similarly, for momentum and energy, we define

$$\eta_p = \frac{\dot{p}_{\rm wind}}{p_{\rm SN} \cdot {\rm SFR}}, \quad \eta_E = \frac{\dot{E}_{\rm wind}}{\xi_{\rm SN} \cdot {\rm SFR}}, \tag{1.41}$$

where the nominator takes the outflow rate of momentum $p_{\rm wind}$ or total energy $E_{\rm wind}$ of the outflow and the SFR in the denominator scaled by an appropriate constant. Note that numerical results often split energy and momentum into different components, e.g., kinetic, thermal (in the case of energy), pressure (in the case of momentum), and magnetic (see, e.g., Kim et al., 2020b). Furthermore,

since $\dot{p}_{\rm wind}$ and $\dot{E}_{\rm wind}$ represent the total flow through some geometrically defined region with an inherent thickness, the flux is sometimes used instead. In these cases, the denominator takes the SFR surface density $\Sigma_{\rm SFR}$ (see Kim et al. 2020b for an example). The constant $p_{\rm SN}$ ($\xi_{\rm SN}$) is typically chosen to be the momentum (energy) per unit of stellar mass injected by SNe in a stellar population, as this is the main source of momentum (energy) at the ISM scales. For a stellar population following an Kroupa (2001) IMF, there is one SN per $95.5\,{\rm M}_\odot$ of stellar mass, implying $\xi_{\rm SN} = 10^{51}\,{\rm erg}/95.5\,{\rm M}_\odot \approx 5.27\times10^5\,{\rm km^2\,s^{-2}}$. For momentum, the constant is computed via either the momentum injected by a SN ($p_{\rm SN} = (2\cdot 10\,{\rm M}_\odot\cdot 10^{51}\,{\rm erg})^{0.5}/95.5\,{\rm M}_\odot \approx 3.4\times10^2\,{\rm km\,s^{-1}}$), or the momentum which builds up during the Sedov-Taylor phase the explosion[14] ($p_{\rm SN} = 2\cdot10^{51}\,{\rm erg}/v_{\rm ST} \approx 1.3\times10^3\,{\rm km\,s^{-1}}$, where I used $v_{\rm ST} = 200\,{\rm km\,s^{-1}}$). Note that the two values for $p_{\rm SN}$ differ by almost a factor of 4.

For the metal loading factor, the definition varies in the literature. One definition is

$$\eta_Z = \frac{\dot{M}_{\rm Z}}{Z_{\rm ISM}\cdot{\rm SFR}}, \tag{1.42}$$

where $Z_{\rm ISM}$ is the gas metallicity of the ISM. This quantity evolves in time, unlike $p_{\rm SN}$ and $\xi_{\rm SN}$. An alternative definition that removes this time dependence is

$$\eta_{Z,{\rm SN}} = \frac{\dot{M}_{\rm Z}}{Z_{\rm SN}\cdot{\rm SFR}}, \tag{1.43}$$

where $Z_{\rm SN}$ is the mass of metals injected by SNe per $95.5\,{\rm M}_\odot$ of stellar mass. A typical value for the scaling constant is $Z_{\rm SN} = 2\,{\rm M}_\odot/95.5\,{\rm M}_\odot \approx 0.02$ (e.g. Kim et al., 2020b). These two quantities measure slightly different things. While η_Z depends on non-trivial mixing and sweep-up of ISM material, it accounts for the past enrichment history of the galaxy (encoded by the ISM metallicity). On the other hand, $\eta_{Z,{\rm SN}}$ is a measure of how efficiently metals injected by SNe reach the CGM, provided all material flowing vertically out of the galaxy originates from SNe.

Figure 1.10 shows examples of mass, metal, and energy loading factors from both observational estimates (solid points) and numerical simulations (see legend). Momentum loading is omitted from the figure since different definitions of this

[14] In the seminal work by Sedov (1959) and Taylor (1950) computed the behavior of the shock wave that propagates from an extremely energetic explosion in response the tests of nuclear warheads. Their theory has since been highly successful in describing how SNe evolved shortly after explosions (see e.g., Kim & Ostriker, 2015)

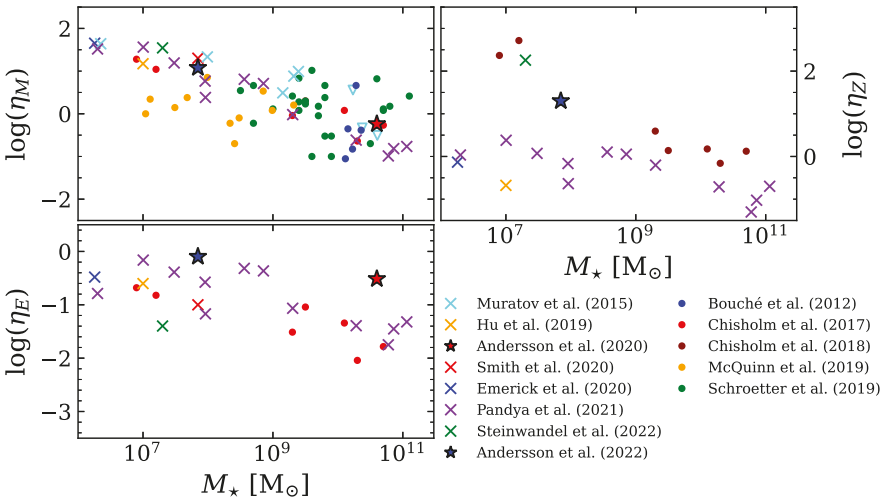

Figure 1.10: Mass, metal, and energy loading factors as a function of galaxy stellar mass, showing observational estimates in filled circles, and numerical results with cross and plus (Papers I and II) symbols. Errors are omitted from the data to keep clarity (see references for more details). Note that loading factors are computed via different tracers (observational results) and at different locations (numerical results), see text for details. Solid points show observational results, while crosses and stars mark numerical results. Inverted triangles in cyan mark upper limits.

quantity in the literature give significantly different values, making comparisons difficult. The observational estimates include outflow properties as traced by background quasar absorption spectra (Bouché et al., 2012; Schroetter et al., 2019), UV absorption spectra (Chisholm et al., 2017, 2018), and via deep Hα mapping (McQuinn et al., 2019). The numerical estimates include a wide range of different models and methods to estimate the loading factor. Muratov et al. (2015) and Pandya et al. (2021) used cosmological zoom-in simulations with the Feedback In Realistic Environment (FIRE, Hopkins et al. 2014) and FIRE2 (Hopkins et al., 2018) models respectively. Both authors estimated loading factors by measuring outflow properties in radial shells at $\sim 0.2\,R_{\rm vir}$, and using Equations 1.40, 1.41, and 1.43 with constants $\xi_{\rm SN} = 5 \times 10^5\,{\rm km^2\,s^{-2}}$, and $Z_{\rm SN} = 0.02$. The markers show the average values for the loading from $z = 0.5 - 0.0$. Note that for Muratov et al. (2015), estimates at $M_\star > 10^{10}\,{\rm M_\odot}$ are upper limits (open inverted triangles). The remainder of the numerical estimates is of galaxies simu-

lated in isolation (i.e., without cosmological context). Hu (2019) and Steinwandel et al. (2022) used the different versions of the Gadget code (Springel, 2005), and computed loading factors similarly to Muratov et al. (2015); Pandya et al. (2021), but measuring outflow properties in cylindrical slabs at ~ 1 kpc from the mid-plane of the disc. Furthermore, in this case, the SFR was computed as the average value over ~ 1 Gyr. Papers I, III, Smith et al. (2020), and Emerick et al. (2020) estimated mass and energy loading (using Equations 1.40 and 1.41 with $\xi_{\rm SN} = 5.27 \times 10^5\,{\rm km^2\,s^{-2}}$) with outflows measured trough cylindrical slabs at 1 kpc vertical distance. Emerick et al. (2020) estimated metal loading factor using Equation 1.43 with $Z_{\rm SN} = 0.02$, while Paper III used Equations 1.42.

As seen in Figure 1.10, loading factors scale with galaxy mass. Furthermore, the scaling between velocity and mass separates winds into momentum driven ($m \sim v^{-1}$), and energy driven ($m \sim v^{-2}$). In the case of momentum-driven wind, one expects $\eta_M \sim \sigma^{-1}$, while for energy-driven winds $\eta_M \sim \sigma^{-2}$, where σ is the velocity dispersion of the galaxy (Somerville & Davé, 2015). While momentum-driven winds produce galaxies that better match the mass-metallicity relation, energy-driven winds typically reproduce the galaxy stellar mass function (see Tumlinson et al., 2017, and references therein). The key to understanding this problem is likely the velocity distribution of the multi-phase wind, which is accessible from numerical experiments. In velocity-temperature space, the winds display a clear dichotomy with the majority of mass ejected in cold gas flows, while hot and diffuse outflows carry the majority of energy and metals (see, e.g., Kim et al., 2020b, , or Paper III). If this allows the metal-rich, highly energetic hot outflows to escape low-mass galaxies while high-mass galaxies retain these winds, it naturally explains the separate mass-metallicity trends between them (Li & Bryan, 2020). Separating the cool and hot outflow is therefore important for the outflow properties (see, e.g., Kim et al., 2020a). Note that this is no easy task since mixing and entrainment between the different gases is highly challenging for numerical simulations and is not a solved problem (see, e.g., Scannapieco & Brüggen, 2015; Naab & Ostriker, 2017).

Chapter 2

The necessity and numerical challenge of star-by-star feedback models

"Is it better to do things fast and wrong, or slow and correct?"
– Anonymous RAMSES user

2.1 Introduction

Simulating galaxies is non-trivial for several reasons: 1) the build-up of structure in the Universe by highly non-linear gravitational clustering; 2) the extreme dynamic range of galaxy evolution, both in time and space; 3) interconnected processes involving both continuous and discrete forms of matter makes the problem highly complex. As a result, a trade-off between the level of detail, control, and statistics for numerical models is necessary. To this end, there is a wide range of modeling approaches, each targeting the different aspects of the problem. With an increasing level of explicit treatment of physical processes (and consequently numerical effort), the most common methods used are analytical models, semi-analytical models (SAMs), and numerical hydrodynamical techniques. In this Chapter, I describe the technical aspects of the research presented in Part II, namely hydrodynamical simulations with adaptive resolution. For details on the other methods, I recommend the reviews Somerville & Davé (2015) and Naab & Ostriker (2017).

The main technical challenge of my thesis work has been developing and implementing the star-by-star model that eventually got called INFERNO (INdivid-

ual stars with Feedback, Enrichment, and Realistic Natal mOtions). INFERNO is implemented in the hydrodynamics+N-body code RAMSES, which was first published in Teyssier (2002). Although RAMSES is publicly available for download[1], my implementation is currently not part of the public repository. I intend to keep implementing additional features to the INFERNO model.

The main challenge of star-by-star models is bridging the gap between the research topic of stars with that of galaxies. Although these two topics are tightly intertwined, stars as individual objects and galaxies evolve on very different scales. As for galaxy models in general, this necessitates a trade-off between the level of detail which is affordable for the stellar model, and the scope of the simulations. With INFERNO, the intention is to address problems covering the scales of entire galaxies and, ideally, the cosmological context (although presently, this remains computationally unfeasible for all but the smallest galaxies in the Universe).

In this Chapter, I describe the numerical aspects of my thesis work. In Section 2.2, I briefly describe the fundamental aspects of numerical hydrodynamics in RAMSES. Section 2.3 describes the star-by-star model INFERNO.

In this Chapter, I describe the numerical aspects of my thesis work. In Section 2.2, I briefly describe the fundamental aspects of numerical hydrodynamics as they are solved in RAMSES. Section 2.3 describes the star-by-star model INFERNO.

2.2 Computational hydrodynamics and N-body problems

The foundation of any hydrodynamical galaxy simulation is to solve the motions of particles and continuous matter (fluids). In our case, the former depends on non-relativistic and non-collisional gravitational forces. This problem is well-understood but numerically expensive. Hydrodynamical modeling is both numerically costly and challenging since astrophysical gases are highly multi-phase with complex cooling and heating processes. Systems are also prone to shocks, instabilities, and turbulence, driven by many different mechanisms (see Chapter 1). These aspects need consideration when designing a numerically stable hydrodynamics solver.

The first challenge of gas dynamics is to describe the continuous nature of fluid, i.e., tracing gas properties at every point in the region of interest. There are two formal descriptions for this: Lagrangian formalism, describing variations of fluid properties in the reference frame of moving gas particles; Eulerian formalism, describing variations of fluid properties with respect to a fixed reference frame. Both

[1] https://bitbucket.org/rteyssie/ramses/wiki/Home

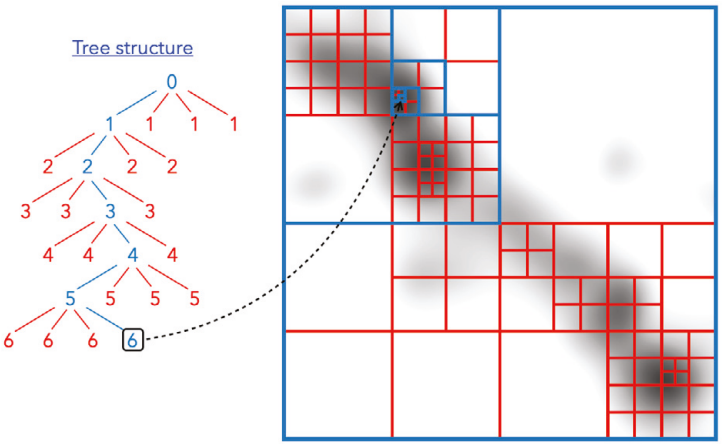

Figure 2.1: Example of AMR grid with tree-structure to find a specific cell (marked in blue) illustrated on top of a dark matter surface density image. The tree structure is illustrated to the left and shows the hierarchy to find the blue cells. Note that every leaf cell has a similar tree structure which leads to the root (level 0).

of these descriptions are common within the astrophysical community. An example of a Lagrangian method is smoothed-particle-hydrodynamics (SPH), often successfully employed for galaxy simulations (see, e.g., GADGET Springel, 2005). However, in its base form, this method has problems dealing with gas mixing and instabilities (Agertz et al., 2007). Such mechanisms are better handled in Eulerian (grid-based) codes, although at the cost of numerical diffusion. Here, I will focus on an example of the latter, the adaptive-mesh-refinement (AMR) method implemented in Ramses. For other codes widely applied in galaxy simulations, a list is provided in Hopkins (2015), with an example of a code comparison in Roca-Fàbrega et al. (2021).

2.2.1 Adaptive mesh refinement

Following the Eulerian description, AMR builds a grid structure for tracking the evolution of the hydrodynamic equations. The grid (also called mesh) is a collection of cells in a three-dimensional structure. In the AMR technique, the mesh has a non-uniform hierarchical structure of Cartesian cells (see two-dimensional example in Figure 2.1). This hierarchy is constructed via levels of refinement, where the size of a cell decreases with increasing level (i.e., the resolution increases with level). The zeroth level defines the entire computational domain (box), and each

integer increase in level splits the domain of the level above through its center. In three-dimensional space, this implies cell splitting into 8 new cells (oct) when refined by one level. The resolution of a cell (side length Δx) is thereby

$$\Delta x = \frac{\text{size of box}}{2^{\text{level}}}. \tag{2.1}$$

A cell is subject to refinement based on some predefined criterion. Except for the zeroth level (root), cells have a parent (the cell which spawned the cell of interest), siblings (cells with the same parent), and can have children (cells created by refinement). A cell without any children is called a leaf. Figure 2.1 shows an example of an AMR hierarchy. In this two-dimensional example, cells have one parent, four children, and three siblings. The tree-like structure (shown to the left in Figure 2.1) implies that searching for a given cell is an $\mathcal{O}(N)$ operation.

A given simulation has a minimum level of refinement (all cells have at least this resolution) and a maximum refinement level that stops arbitrarily high resolution. Between these levels, the refinement adapts, typically to keep a similar mass in all cells (resulting in more cells in dense regions) and/or to have a fixed number of particles in each cell. Other examples include geometrically defined criteria or flagging cells for refinement with some property advected with the fluid.

2.2.2 Solving the hydrodynamic equations

Recall the Euler equations (Equations 1.16, 1.17), which describe the evolution of gas as viewed in an infinitesimal volume of space. Including an equation for the energy evolution, these equations can be written as a single equation in vector form

$$\frac{\partial}{\partial t}\mathbf{U} + \nabla \mathbf{F} = \mathbf{S}, \tag{2.2}$$

where we introduced a state vector **U**, a flux vector **F**, and a source vector **S**. Note that we now disregard the viscosity term. These vectors are defined

$$\mathbf{U} = \begin{bmatrix} \rho \\ \rho \mathbf{v} \\ \rho e \end{bmatrix}, \quad \mathbf{F} = \begin{bmatrix} \rho \mathbf{v} \\ \rho\, \mathbf{v} \otimes \mathbf{v} + P \\ \mathbf{v}\,(\rho e + P) \end{bmatrix}, \quad \mathbf{S} = \begin{bmatrix} 0 \\ -\rho \nabla \phi \\ -\rho\, \mathbf{v} \cdot \nabla \phi \end{bmatrix}, \tag{2.3}$$

where ρ is mass density, $\mathbf{v}$ is the velocity vector for fluid flow, P is internal gas pressure, e is the total specific energy, and ϕ is the gravitational potential.

To close the set of the hydrodynamical equations, we will assume an equation of state. This equation is that of an ideal fluid with an adiabatic index $\gamma = 5/3$,

providing an equation for pressure

$$P = (\gamma - 1)\rho(e - \frac{1}{2}v^2). \tag{2.4}$$

In Section 1.4, we found that viscosity can be disregarded, motivating the choice of an ideal fluid. However, cooling and heating make the gas non-adiabatic. Therefore, the adiabatic assumption only applies when these equations are solved, and between solutions, the fluid is regarded as non-adiabatic. In the remainder of this section, we focus on how these equations are discretized and solved numerically.

The finite volume method, the Riemann problem, and Godunov solvers

To numerically evolve Equation 2.2, we use the finite volume method, where we consider numerical approximations of the vectors, discretized in space by Δx and in time by Δt. Note that both Δx and Δt take values specific for a given level of the AMR grid. We consider the discretized space as cells i on the grid, with left and right boundaries denoted $x_{i-1/2}$ and $x_{i+1/2}$, respectively. A step forward in time is denoted by superscript n, i.e. $t^n \rightarrow t^{n+1}$. The left illustration in Figure 2.2 shows how this is set up. In this description, Equation 2.2 can be expressed discretely as

$$\frac{U_i^{n+1} - U_i^n}{\Delta t} + \frac{F_{i+1/2}^{n+1/2} - F_{i-1/2}^{n+1/2}}{\Delta x} = S_i^{n+1/2}, \tag{2.5}$$

where we consider the time-centered values for the flux at the boundary.

When searching for a solution to Equation 2.5, the source term is assumed to be zero. This solution is later corrected by adding gravitational acceleration as a non-stiff source term (i.e., ensuring numerical stability, although at the loss of energy conservation). In this way, the system of equations becomes an initial value problem, solvable by a Riemann solver. For the remainder of this section, the focus is to describe how this proceeds. The gravitational potential is described in Section 2.2.3.

In one spatial dimension, the Riemann problem consists of a conservation equation and a set of initial conditions,

$$\frac{\partial}{\partial t}\mathbf{U} + \frac{\partial}{\partial x}\mathbf{F} = 0; \quad \mathbf{U} = \begin{cases} \mathbf{U}_L, & x \leq 0 \\ \mathbf{U}_R, & x > 0 \end{cases}. \tag{2.6}$$

A discontinuity at $x = 0, t = 0$ separates a left ($\mathbf{U}_L$) and a right state ($\mathbf{U}_R$), e.g., the interface between two cells to the left in Figure 2.2. The goal is to find the flux

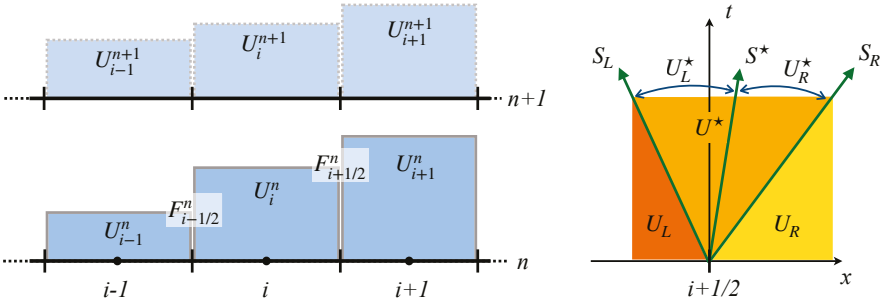

Figure 2.2: *Left:* Illustration of how the finite volume discretizes a continuous medium, such as gas. The properties of each cell (with center denoted by i) at time step n is represented by state vector U_i^n, and the flux across boundaries which arises due to the discontinuity is represented by flux vector $F_{i\pm1/2}^n$. *Right:* Illustration of how the solution of the Riemann problem evolves in a space-time diagram, taking the solution to be that approximated by the HLLC solver. The HLLC solver assumes that three waves propagate from the discontinuity at the cell boundary, one going toward the left (S_L), one toward the right (S_R), and one at the contact point S^*. Since these waves limit the propagation of information, the evolution of the state vector is confined to different regions (colored in different shades of orange), separated by the trajectories of these waves (green arrows).

$\mathbf{F}^*$ at $x = 0$, which arises as waves start to propagate away from the discontinuity. As an example, we can consider the case of the linear hydrodynamic equation, written

$$\frac{\partial}{\partial t}\mathbf{U} + \mathbf{A}\frac{\partial}{\partial x}\mathbf{U} = 0; \quad \mathbf{U} = \begin{bmatrix}\rho \\ v\end{bmatrix}, \quad \mathbf{A} = \begin{bmatrix}0 & \rho_0 \\ c_s^2/\rho_0 & 0\end{bmatrix}, \tag{2.7}$$

where ρ_0 is an initial density, and c_s is the velocity that waves propagate at in the medium (speed of sound). A detailed derivation of the solution to this problem is found in Toro (2009), but briefly described, the system of equations is solved for $t > 0$ with eigenvalue decomposition and shown to be

$$\mathbf{U}(x,t) = \begin{bmatrix}\rho(x,t) \\ v(x,t)\end{bmatrix} = \begin{cases}\mathbf{U}_L, & 0 < t \le -x/c_s \\ \mathbf{U}^*, & 0 \le |x|/c_s < t \\ \mathbf{U}_R, & 0 < t \le x/c_s\end{cases}, \tag{2.8}$$

where

$$\mathbf{U}^* = \frac{c_s\rho_R - \rho_0 v_R}{2c_s\rho_0}\begin{bmatrix}\rho_0\\ -c_s\end{bmatrix} + \frac{c_s\rho_L + \rho_0 v_L}{2c_s\rho_0}\begin{bmatrix}\rho_0\\ c_s\end{bmatrix}. \tag{2.9}$$

This solution is called the Piecewise Constant solution, and as seen in Equation 2.8, the space-time evolution of the state vector splits into three different domains.

The Euler equations is a set of quasi-linear equations[2]. To solve this set of equations applied to the Riemann problem, we make use of the Godunov scheme (see Godunov & Bohachevsky, 1959). This scheme solves conservation equations iteratively in the finite volume approximation (i.e., for discrete values $\mathbf{U}_i^n = \frac{1}{\Delta x}\int \mathbf{U}(t^n, x)\,\mathrm{d}x$, where the integral is taken between volume boundaries $x_{i\pm1/2}$), taking a step in time with the forward Euler method,

$$\mathbf{U}_i^{n+1} = \mathbf{U}_i^n + \frac{\Delta t}{\Delta x}\left(\mathbf{F}_{i-\frac{1}{2}} - \mathbf{F}_{i+\frac{1}{2}}\right), \tag{2.10}$$

where the flux at the interfaces is calculated via the Riemann solution, e.g., $\mathbf{F}_{i-1/2} = \mathbf{F}^*_{i-1/2}$, and vice versa. The challenge is to find an estimate of the time-average flux at the boundaries. To first-order, one can find an exact solution, as with the example of Equation 2.7 (see Toro, 2009); however, since this solution is only first-order accurate in time and space, it suffers from significant numerical diffusion. Instead, variations of the Godunov method look for an approximate solution to be solved iteratively to achieve accuracy. An example of such a method is the HLLC Riemann solver, used in the numerical simulations presented in Part II of this thesis. This method extends the Harten, Lax, and van Leer (HLL) solver (described in Harten et al. 1983), by introducing a contact wave (C) to the Riemann solution.

Briefly described, HLL solves the Riemann problem by studying the wave structure which arises around the discontinuity, accounting only for the two fastest traveling waves S_L and S_R (not to be confused with the source term in, e.g., Equation 2.5), going toward the left and right states, respectively. In a shock tube problem (with higher density in the left state), the two waves are the shock wave propagating to the right and the rarefaction wave propagating to the left. Note that this solution is only correct for hyperbolic systems of two equations (e.g., Equation 2.7), and for the Euler equations, this solution can be highly inaccurate (Toro, 2009). The HLLC method improves the solution drastically by introducing a third wave to the solution, namely a contact wave. This wave S^* introduces left

[2] Quasi-linearity of the Euler equations means that if written on the same form as in Equation 2.7, the matrix $\mathbf{A}$ is a function of U, x, and t.

and right star states (U_L^*, U_R^*), with corresponding flux vectors. An illustration is shown to the right in Figure 2.2 by a so-called Riemann fan.

Timestep conditions

To evaluate Equation 2.10, one needs values for Δx and Δt. Δx is set by the AMR grid (see Section 2.2.1). Δt is limited to small values to ensure a stable and accurate solution for the Euler step. For fluid dynamics, the strongest constraint is the Courant–Friedrichs–Lewy condition, which states that solutions to partial differential equations are stable only if

$$CLF = \Delta t \sum_{i}^{\text{ndim}} \frac{v_i}{\Delta x_i} \leq CLF_{\text{max}}, \tag{2.11}$$

where the sum goes over all dimensions ndim. The constant CLF_{max} depends on the numerical solver, but explicit solvers typically demand $CLF_{\text{max}} \lesssim 1$. The physical interpretation of this condition is that information propagated in the fluid flow at velocity v_i, cannot be displaced further than the distance between two adjacent cells in a discrete timestep Δt. In practice, the timesteps are synchronous on each AMR level, i.e., the maximum velocity found on the grid limits the timestep of each level. Note that the timestep is often constrained further by other conditions, e.g., conditions set by the gravity solver described in Section 2.2.3.

2.2.3 Gravitational forces

For astrophysical problems, both fluids and particles need to be co-evolved. For example, galaxies are built-up by gas (fluid), stars (particles), and dark matter (typically particles). All these components contribute to the gravitational potential. Furthermore, the potential also corrects the Godunov solution for the Euler equations (described in the previous section). Particles behave as a N-body problem of collisionless (smoothed forces) particles. In this section, I first describe the equations governing particle motions. Second, I describe the mapping between particles and fluids to obtain the gravitational potential. Note that the collisionless nature of dark matter is a fundamental assumption in ΛCDM; however, stars only behave collisionless on large physical scales. This problem is discussed further in Section 2.3.

Gravity between particles

Particle motions are described by the Vlasov-Poisson equations

$$\mathbf{v}_\mathrm{p} = \frac{\mathrm{d}\mathbf{x}_\mathrm{p}}{\mathrm{d}t}, \quad \mathbf{a}_\mathrm{p} = \frac{\mathrm{d}\mathbf{v}_\mathrm{p}}{\mathrm{d}t} = -\nabla\phi, \tag{2.12}$$

where the subscript p distinguishes particle properties from cell properties. The Poisson equation

$$\nabla^2\phi = 4\pi G\rho, \tag{2.13}$$

is used to calculate the gradient of the gravitational potential. Ramses employs a second-order midpoint method, which is a simple, but efficient algorithm to solve Equations 2.12 numerically. The algorithm first takes a predictive step and then corrects the solution, following the procedure

$$\begin{aligned}
\mathbf{v}_\mathrm{p}^{n+1/2} &= \mathbf{v}_\mathrm{p}^{n} - \frac{\Delta t^n}{2}\nabla\phi^n, \\
\mathbf{x}_\mathrm{p}^{n+1} &= \mathbf{x}_\mathrm{p}^{n} - \Delta t^n\, \mathbf{v}_\mathrm{p}^{n+1/2}, \\
\mathbf{v}_\mathrm{p}^{n+1} &= \mathbf{v}_\mathrm{p}^{n+1/2} - \frac{\Delta t^n}{2}\nabla\phi^{n+1}.
\end{aligned} \tag{2.14}$$

This implicit solution to the equations of motion conserves their energy. In our case, the timestep adapts between iterations (for constant timesteps, the method is referred to as a Leapfrog scheme). Therefore, each particle remembers the level of where it resided at the previous iteration to achieve the correct corrector step. Note that similarly to the CLF condition, the timestep is limited such that particles can only travel a fraction of the cell size.

Gravitational potential field

In Ramses, the potential is calculated by projecting the distribution of particles on the mesh grid and then solving the Poisson equation discretely. This class of methods is referred to as the particle-mesh method (Hockney & Eastwood, 1988). The first goal is to map particles onto the grid. The mapping is performed using the cloud-in-cell technique, which distributes the mass of a particle in cells within one cell size distance of the particle (referred to as the cloud of that particle). The mass contribution to a cell within the scope of the particle is the fraction of mass in the volume $(\Delta x)^3$ around the particle which overlaps with that cell.

This problem is straightforward to solve on a uniform grid; however, the particle assignment is not trivial for an AMR structure. To this end, particle assignment

is performed at each level, considering first the contribution from particles within the boundaries of that level. After this initial assignment, particles that reside in the neighbors of the parent cell can contribute to the cell density if their clouds overlap with that cell. This assignment continues until the highest level in the hierarchy is reached (unless specifying a maximum level for particle mass assignment), thereby generating a density field at each level (identical to one of a uniform grid at that level). This procedure limits the resolution of the potential to be that of the AMR structure (i.e., the potential is smoothed on the scale of the mesh grid).

With the density structure in place, the Poisson equation (2.13) is readily solvable. In discrete form, the equation is

$$\frac{\phi_{i-1} - 2\phi_i + \phi_{i+1}}{(\Delta x)^2} = 4\pi G \rho_i, \tag{2.15}$$

where indexing follows a similar convention as in Section 2.2.2. Since the number of unknowns (ϕ_i) is the same as the number of equations, the set of equations can be solved algebraically. To do so, Equation 2.15 is rewritten as a linear set of equations, and solved via matrix inversion using Gauss-Seidel iterations (see Springel, 2016, for details). To increase the computational speed, Ramses uses a multi-grid method, performing the Gauss-Seidel iterations on the AMR hierarchy (Guillet & Teyssier, 2011). The course level (low resolution) solution can be solved efficiently due to a smaller number of cells and is then used to correct the solution at higher levels. Furthermore, the method accounts for the adaptive timestep, and course levels do not need to be evolved with the timestep at finer levels.

2.2.4 Sub-grid models for unresolved physics

For galaxy simulations, the vast number of astrophysical processes are impossible to treat from a first principle. For example, gas heating and cooling (see Section 1.4.2) is typically solved by tabulating values for the net cooling rate. These rates are applied on the grid of the simulations. Methods of this kind, which treat physical processes that take place below the grid resolution of the simulation, are referred to as *sub-grid models*.

Another example of sub-grid physics in galaxy simulations is the evolution of stars. Because galaxies like the Milky Way have stellar masses that are more than 10 order of magnitude larger than that of individual stars, resolving individual stars introduces high computational cost. Traditionally, this problem is relieved by introducing a macroscopic model for stars, where stars formed together are treated as mono-age populations, which dynamically evolve as a point. Thereby,

stellar components are tracked at some mass resolution, with appropriate subgrid models to treat how they interact with their surroundings. Oftentimes, these models assume feedback injection rates which are averaged over the IMF (see, e.g., Smith, 2021, for a discussion and examples of inherent problems of this approach), sometimes without regard for the timescales of when stars inject different types of feedback. This imposes a severe limitation on galaxy modeling. In the remainder of this chapter, I describe a method that relives many of these limitations.

2.3 The star-by-star model INFERNO

At the end of the previous section, I described the macroscopic model of stars as mono-age stellar populations. While this approach is still necessary to achieve computationally feasible cosmological simulations of large galaxies (including zoom-in simulations), galaxy simulations frequently achieve a resolution in baryons of a few tens of solar masses (see, e.g., Wheeler et al., 2019; Agertz et al., 2020; Smith et al., 2021). In these cases, star particle masses are comparable to those of individual stars, and the macroscopic description of stars is only a limitation rather than a trick to increase computational efficiency. Tracing individual stars allows for detailed modeling of when and *where* stars inject feedback. For example, it enables the inclusion of runaway stars (described in Section 1.5.4), which play a role in galactic scale processes such as outflows (Andersson et al., 2020, 2022), and star formation relations (Andersson et al., 2021).

In this section, I describe the star-by-star model INFERNO, developed, implemented, and used to explore how individual stars affect galaxies of different masses (results presented in Part II). Compared to the description of this model provided as part of the published research, I describe the broader context in which the model was developed and discuss numerical details which not in the publications.

2.3.1 Star formation and sampling the initial mass function

Star formation is modeled by employing a Schmidt-like recipe (see Section 1.5.1). Each cell with cold ($T < T_0$) gas density that exceeds a threshold ρ_0 is flagged as eligible for star formation. This condition, combined with Equation 1.36, gives the

$$\dot{\rho}_\star = \epsilon_{\rm ff} \frac{\rho_{\rm g}}{t_{\rm ff}}, \quad \rho_{\rm g} > \rho_0,\ T < T_0, \tag{2.16}$$

where $t_{\rm ff}$ is computed from Equation 1.14. Typical values for the parameters are $\epsilon_{\rm ff}$ in the range 0.01 to 0.1, ρ_0 in the range $100 - 500\, m_p$ cm^{-3}, and $T_0 \leq 10^4$ K

(see Section 1.5.1 for details). To convert the star formation rate density to discrete mass quanta, the model computes a star formation mass $m_\star = \dot{\rho}_\star \Delta x \Delta t$ and uses a Poisson sampling procedure to compute the number of such quanta that should spawn in a given star formation event. The procedure follows the definition of the Poisson distribution

$$\mathcal{P}_i(n_i) = \frac{\lambda_i^{n_i}}{n_i!} \mathrm{e}^{-\lambda_i}, \tag{2.17}$$

with $\lambda = m_\star / m_0$, where m_0 is a parameter used to set the total mass for each sampling procedure of individual stars.

To sample individual stars from m_0, the model assumes some IMF and employs a Poisson sampling procedure similar to that used for star formation (see Sormani et al. (2017) for details). It is not computationally feasible to include all stars as individual particles. Therefore, the IMF is only *resolved* above some mass threshold $m_{\star,\mathrm{min}}$, splitting particles into two types, one tracing populations of low-mass stars and one tracing high-mass stars as individual particles. To do this, the IMF is pre-defined in mass bins; one bin for all low mass stars ($< m_{\star,\mathrm{min}}$), and N bins for the high mass range ($> m_{\star,\mathrm{min}}$). The number of stars spawned in each high mass bin is determined by sampling the Poisson distribution (Equation 2.17), with each bin indexed i is associated with a Poisson parameter

$$\lambda_i = f_i \frac{m_0}{m_i}, \tag{2.18}$$

where m_i is the mass of stars in the bin, and f_i is the fraction of mass in the bin relative to the m_0, calculated via

$$m_i = \frac{\int_i m \cdot \xi(m)\, \mathrm{d}m}{\int_i \xi(m)\, \mathrm{d}m}, \tag{2.19}$$

$$f_i = \frac{\int_i m \cdot \xi(m)\, \mathrm{d}m}{\int_{\mathrm{IMF}} m \cdot \xi(m)\, \mathrm{d}m}, \tag{2.20}$$

where the integrals indexed i cover the mass range of the bin, and the integral in the denominator of f_i spans the entire mass range of the IMF. Note that because this is a stochastic method, the total mass sampled is only equal to m_0 on average. To conserve mass, the sampling process is performed by sampling the bins from low to high mass, stopping the procedure (and removing the last sampled star) when the sampled mass exceeds m_0. Compared to the targeted IMF, this results in a slightly bottom-heavy one. There are methods to handle this problem (see

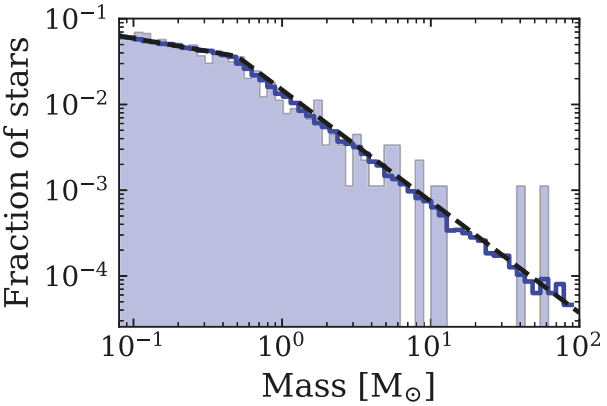

Figure 2.3: Initial mass function with the analytical model from Kroupa (2001) in black dashed line, and using the sampling prescription from Sormani et al. (2017) in blue. The filled histogram shows the result of one sampling procedure of 500 $M_\odot$ of mass, while the blue line shows the sum of 200 such samples.

e.g Smith, 2021). In contrast to treating the IMF as a probability distribution and directly drawing random mass, this procedure provides control of the total number of random numbers generated in each sampling process and better handling of computer memory.

As an example, Figure 2.3 shows mass function of stars sampled with this method for a Kroupa (2001) IMF (see Section 1.5.2) and $m_0 = 500$ $M_\odot$. While this m_0 is too small to provide a well sampled IMF for an individual event (blue histogram), the average IMF (solid blue line) in a given simulation approaches the theoretical model (black dashed line).

2.3.2 Natal stellar velocities

Since gravitational forces between particles scale as the inverse square of their separation, the gravitational potential must be softened to avoid extreme forces (which makes the gravity solver unstable, see Section 2.2.3). Softening removes dynamic interactions on scales below the cell size. Since the dynamics which result in runaway stars (see Section 1.5.4) are below this scale, these types of stars cannot generate self-consistently. INFERNO uses a *sub-grid* model to assign velocities at stellar birth to solve this problem.

The velocity of all newly formed stars is initially that of the gas in the cell where

they originate. In addition, individual stars receive a perturbation to this velocity. The model introduces velocity perturbations of two different kinds: 1) a small velocity dispersion applied to all individual stars (`stir`); 2) velocity kicks which reproduce the velocity distribution of stars that escape the natal cluster (`kick`). Velocities are applied isotropically. The escaping stars are referred to as runaway stars if their velocity is $> 30\,\mathrm{km\,s^{-1}}$), and walkaway stars otherwise (note that this definition varies in the literature, see Section 1.5.4).

The `stir` method applies a velocity dispersion σ_v at birth, assuming a Gaussian distribution for the velocities

$$\mathcal{N}(v) = \frac{1}{\sqrt{2\pi}\sigma_v} \exp\left[-\frac{(v - \langle v \rangle)^2}{2\sigma_v^2}\right]. \tag{2.21}$$

The implementation samples this distribution for the magnitude of the `stir` velocity, taking the mean velocity $\langle v \rangle = 0$. To find the direction of the velocity, the model employs a mathematical trick based on properties of the same distribution. For a random variable r centered around 0 and standard deviation $\sigma = \sqrt{1/2}$, Equation 2.21 simplifies to

$$\mathcal{N}(r) = \frac{1}{\sqrt{\pi}} \exp\big[-r^2\big] = \frac{1}{\sqrt{\pi}} \exp\big[-(x^2 + y^2 + z^2)\big], \tag{2.22}$$

where the last equivalence follows from the coordinate change between spherical and Cartesian coordinates. The last term is equivalent to the product of individual Gaussian distribution for coordinates x, y, z. Furthermore, the transformation is independent of the angle coordinates in the spherical coordinate system, and a vector of three Gaussian numbers (representing the Cartesian coordinates) is isotropic with the origin at $r = 0$. The full procedure is

$$\mathbf{v} = v\hat{\mathbf{r}} = v\frac{[x, y, z]}{\sqrt{x^2 + y^2 + z^2}}, \tag{2.23}$$

where x, y, z are sampled from some random number generator with a Gaussian distribution, and v is the magnitude of the velocity.

While the `stir` method can be considered a numerical trick to allow stars with otherwise perfectly overlapping trajectories to disperse over time (hence σ_v ought to be very small), the `kick` method aims to model walkaway and runaway stars. To do so, INFERNO implements isotropic kicks sampled from some distribution. As discussed in Section 1.5.4, the initial velocity distribution of these stars

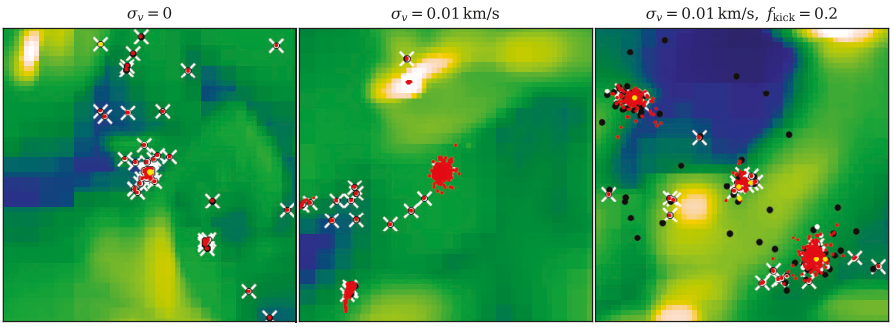

Figure 2.4: Positions of stellar objects with ages < 100 Myr shown on top of density projection in 200 pc width panels for three examples of different natal kick models, denoted by the title of each panel. Each panel is centered on the oldest stellar population in the sample. The two left-most panels do not include the `kick` model. White crosses show particles representing unresolved stellar population (< 2 M$_\odot$), red points show main sequence stars, yellow points show post-main-sequence giants, white points show white dwarfs, and black points show black holes. The data used to produce the plot is from the simulations presented in Paper III.

is challenging to ascertain. In Oh & Kroupa (2016), the authors studied the fraction of ejected stars and their velocity distribution for a set of natal star clusters. They found that in the first 3 Myr of dynamical evolution, a cluster with a mass $10^{3.5}$ M$_\odot$ ejected roughly 20% of its stars, with velocities distributed according to

$$f_v \propto v^{-\beta}, \quad 3 \leq v \lesssim 385\,\mathrm{km\,s^{-1}}, \tag{2.24}$$

where β had a value around 1.8. The peak of the ejection rate occurred around 1 Myr after the start of their simulation. Notably, massive stars are more prone to ejection from the cluster.

For our model, we sample velocities from Equation 2.24 and apply it to a fraction $f_{\rm kick}$ of all newly born massive (8 M$_\odot$) stars. In Paper I and II, we assumed $f_{\rm kick} = 1$, while Paper III explores different values for this parameter. To sampling procedure for `kick` velocities is fairly straightforward. Since the cumulative density distribution of f_v is

$$F_v = \int_0^v f_v(v)\,\mathrm{d}v \propto v^{1-\beta}, \tag{2.25}$$

a random number X from a uniform distribution will result in a velocity following

the distribution f_v, if given by

$$v = v_{\rm min}(1 - X)^{\frac{1}{1-\beta}}. \tag{2.26}$$

The lower limit in velocity is obtained for $X = 0$. To truncate the distribution at an upper limit for velocity, the upper bound for X is

$$X_{\rm max} = 1 - \left(\frac{v_{\rm min}}{v_{\rm max}}\right)^{1-\beta}. \tag{2.27}$$

For $\beta = 1.8$, this sampling procedure results in $\sim 14\%$ of stars with velocities $> 30\,{\rm km\,s^{-1}}$. The directions of the velocities are computed in the same way as for `stir`. Note that `kick` and `stir` are mutually exclusive.

As an example, Figure 2.4 shows the distribution of stars (points) around stellar populations (white crosses) which formed < 100 Myr before the snapshot, using data from the simulations in Andersson et al. (2022). The left panel shows that coeval stars remain on identical trajectories indefinitely unless perturbations are applied. The center panel shows an example of `stir`, with a minuscule velocity dispersion ($\sigma_v = 0.01\,{\rm km\,s^{-1}}$). In this case, stars remain on similar trajectories for a long time, although strong interactions with clouds or other star clusters can lead to their disruption (such populations are found in the center and lower left corner of the middle panel). The third panel includes the `kick` model with $f_{\rm kick} = 0.2$, with 3% runaway stars and 17% walkaway stars. In this case, some stars and many black holes (black points) are in isolation.

2.3.3 Stellar feedback

The feedback model implemented in INFERNO incorporates the injection of mass, momentum, and energy from stars as they evolve through different stages (see details in Section 1.5). This model includes the injection of chemically enriched material, as described in Section 2.3.4. The current implementation is described briefly in the two following paragraphs.

Based on the initial mass, metallicity, and age of an individual star, INFERNO computes the feedback associated with fast ($\sim 1000\,{\rm km\,s^{-1}}$) stellar winds launched by massive ($> 8\,{\rm M_\odot}$) stars, slow ($\sim 10\,{\rm km\,s^{-1}}$) stellar winds launched by giant branch stars, and explosions via core-collapse supernovae (CCSNe) of massive stars. The main-sequence lifetime determines the timing of the feedback. The fast winds are launched at constant mass-loss rates when the star is on the main sequence, and CCSN occurs just after. Each CCSN results in the release of 10^{51} erg

of energy, except for the most massive (> 30 $M_\odot$) stars, in which case we assume direct collapse to a black hole. Low-mass stars remain inactive during the main sequence and start launching winds upon entering the giant branch. These winds have a constant mass loss rate until the entire envelope is expelled. The total mass ejected during the various scenarios is computed by interpolating the tables from the NuGrid collaboration (Pignatari et al., 2016; Ritter et al., 2018).

The main sequence lifetime is computed from the fitting function of Raiteri et al. (1996), expressed

$$\log \tau_{\rm MS} = a_0(Z) + a_1(Z) \log m + a_2(Z)(\log m)^2, \tag{2.28}$$

where m is the initial stellar mass, Z is the stellar metallicity, and the coefficients are given by

$$\begin{aligned} a_0(Z) &= 10.13 + 0.07547 \log Z - 0.008084(\log Z)^2, \\ a_1(Z) &= -4.424 - 0.7939 \log Z - 0.1187(\log Z)^2, \\ a_2(Z) &= 1.262 + 0.3385 \log Z + 0.05417(\log Z)^2. \end{aligned} \tag{2.29}$$

This function is fitted to data of the H and He burning times of stars in the mass range 0.6 to 120 $M_\odot$, and metallicity (total metal mass fraction) range 0.0004 to 0.05, computed using the Padova model (Alongi et al., 1993; Bressan et al., 1993; Bertelli et al., 1994).

In addition to feedback from individual stars, inferno accounts for feedback from explosions associated with supernovae type Ia (SNeIa). As with CCSNe, these events release 10^{51} erg of energy, with an explosion rate determined by a delay-time distribution fitted to empirical data (Maoz & Graur, 2017). The mass injected in SNeIa events is 1.4 $M_\odot$, i.e., the Chandrasekhar mass (Chandrasekhar, 1931). The particles representing unresolved low-mass stars determine the locations of these explosions.

Figure 2.5 shows a comparison between the cumulative energy injection rate of the inferno model and the stellar population evolution code StarBurst99 (SB99) (Leitherer et al., 1999; Vázquez & Leitherer, 2005; Leitherer et al., 2010, 2014). Both models include the same IMF and core-collapse progenitor mass range and assume solar metallicity for all stars. The SB99 data assumes the stellar wind model from the Padova group, including a wind model for AGB stars. The energy budget from CCSNe is similar; however, inferno underestimates the energy from fast winds (OB stars) compared to SB99. inferno does not include a wind model for super-giant stars ($8 - 12$ $M_\odot$) active in the time between the

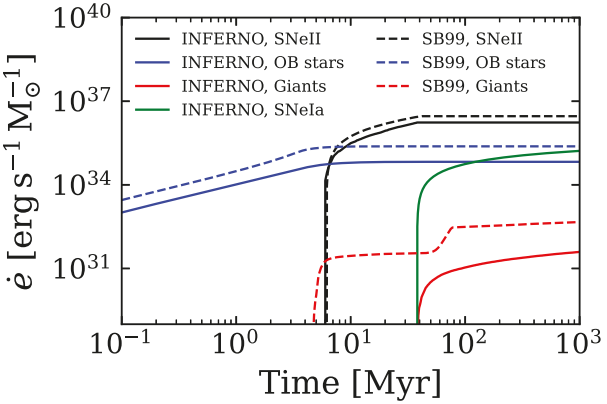

Figure 2.5: Cumulative injection rate of specific energy for a 10^5 $M_\odot$ mono-age population of stars as a function of time. Feedback from different sources according to the legend.

first SNe ($\sim$ 6 Myr) and the onset of the AGB phase ($\sim$ 40 Myr), explaining the discrepancy in wind energy between the models during this period. While there are some differences, the overall feedback budget is similar (except for SNeIa), highlighting that the star-by-star model INFERNO employed on galaxy simulations includes details comparable to population synthesis codes.

2.3.4 Chemical enrichment

In addition to providing energy to the stellar interior, the nucleosynthesis inside stars produces elements heavier than He (metals). Since feedback ejects material from stars, this process becomes one of the dominant sources of chemical evolution. As described in Section 1.5, the stellar interior is complex (particularly mixing between various layers within the star). Furthermore, because the mass loss from stars changes drastically throughout this evolution, different stars provide distinct chemical signatures. Studying these signatures to disentangle the history of the Galaxy is a highly active field of modern astrophysical research (see, e.g., Bland-Hawthorn & Gerhard, 2016; Helmi et al., 2018; Helmi, 2020). Furthermore, missions like the Gaia satellite (Gaia Collaboration et al., 2022)) and large spectroscopic surveys like APOGEE (Jönsson et al., 2020) and GALAH (Buder et al., 2021) are dedicated to this task.

However, understanding the implications of chemical signatures observed in,

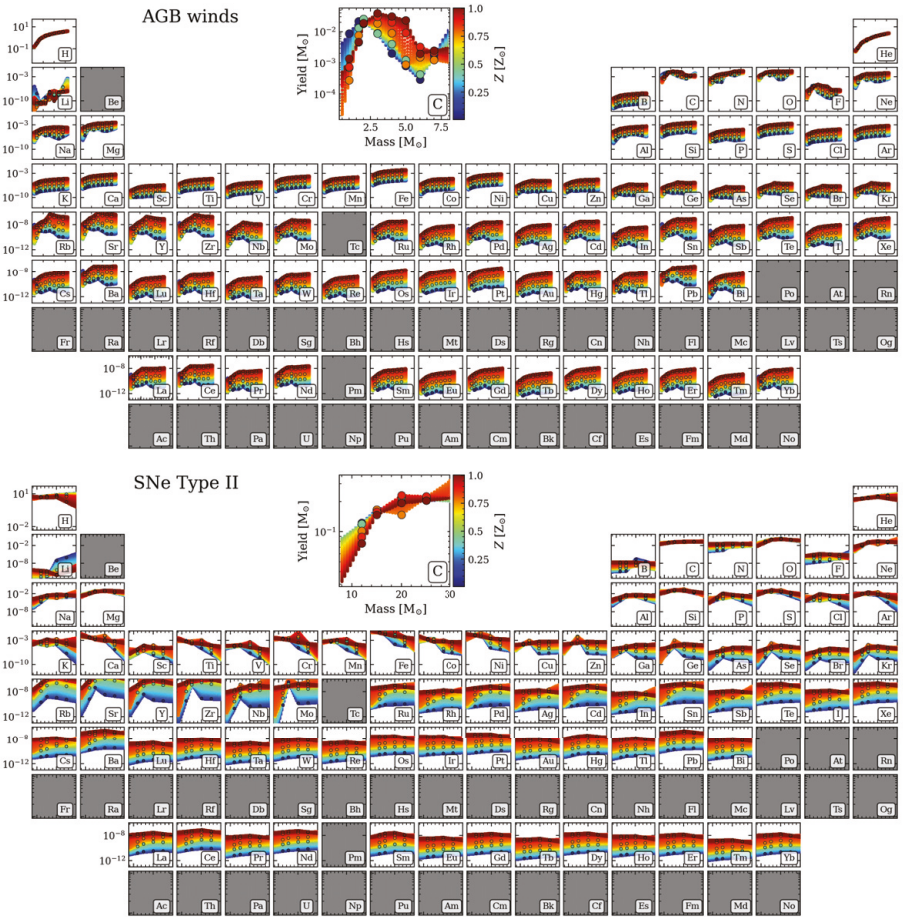

Figure 2.6: Total yield as a function of initial stellar mass (colored by the metal mass fraction) for all elements implemented in the INFERNO model, showing mass injected via AGB winds in the upper periodic table and for CCSNe in the lower one. An inset showing carbon yields provides a detailed example. Each tile (including inset) shows the data points from NUGRID (Pignatari et al., 2016; Ritter et al., 2018) (filled circles) and results from the bilinear method used to interpolate yields in INFERNO (colored scatter points).

e.g., the Milky Way necessitates a theoretical basis for galactic scale chemical evolution. On the one hand, SAMs can be used to investigate the effects of, e.g., chemical yield models, stellar population properties (e.g., IMF), and analytically prescribed star formation rates, gas flow, and radial migration (see, e.g., Chiappini et al., 1997; Kobayashi et al., 2006, 2020; Spitoni et al., 2010; Spitoni & Matteucci, 2011). On the other hand, hydrodynamical models can describe the signatures of complex merger histories resulting from the cosmological environment (Ma et al., 2017; Mackereth et al., 2018; Agertz et al., 2021; Buck et al., 2021; Renaud et al., 2021). However, due to the numerical cost of the latter, the chemistry is often traced only for a hand full of elements, with simplified models to treat the injection of elements from stars.

Chemical enrichment in INFERNO accounts for the star-by-star prescription, with yields that depend on initial stellar mass and metallicity. Furthermore, yields are separated by injection mechanism (see details in Section 2.3.3). Similarly to the total mass loss in winds and SNe, yields are calculated via bilinear interpolation of pre-determined values from the NuGrid tables (Pignatari et al., 2016; Ritter et al., 2018). For SNeIa (not included in NuGrid), INFERNO use yields from Seitenzahl et al. (2013). This approach enables metals ejection from individual stars at the time of expected mass loss. Figure 2.6 show the yields of AGB winds and CCSNe, which are two important sources of enrichment. While the majority of elements in the periodic table are implemented, a given simulation is often memory limited to tracing only a subset of them. To handle this problem, a subset of elements is selected on initialization via input parameters. Furthermore, the yield tables are provided at this stage, enabling the user to use the yield data they prefer.

2.4 Outlook

Star-by-star model is a natural step toward high-resolution galaxy simulations, which allow for a more complete model for the formation and evolution of galaxies. This is particularly applicable for modern galaxy simulations now reaching baryonic mass resolution comparable to (and sometimes smaller than) the masses of individual stars. Star-by-star models allow for a detailed account of when and where individual stars inject feedback on their surroundings, which plays a role in setting crucial properties of galaxies, e.g., galactic scale winds (Paper I and III) and observed star formation relations in galactic outskirts (Paper II). So far, only a limited number of models implement star-by-star calculations for simulations on scales of entire galaxies (see, e.g., Hu et al., 2016; Emerick et al., 2018; Andersson

et al., 2020, 2021, 2022; Gutcke et al., 2021, 2022b,a; Hirai et al., 2021; Calura et al., 2022; Hislop et al., 2022).

With INFERNO, I foresee several future projects, some of which are already in preparation. As part of the "Engineering Dwarfs at Galaxy formation's Edge" (EDGE) project, current efforts toward a cosmological simulation of an ultra-faint dwarf galaxy with individual stars are underway. These galaxies are the essential building blocks of galaxy formation, and their small sizes make them sensitive to feedback details (Agertz et al., 2020; Rey et al., 2020; Orkney et al., 2022; Prgomet et al., 2022). Furthermore, their low surface brightness makes them notoriously difficult to observe (Vargas et al., 2013; Simon, 2019). The star-by-star treatment, in combination with the detailed chemical model of INFERNO, enables highly detailed studies to compare observations and simulations. A project of this kind is currently ongoing.

A near-future improvement to the INFERNO model is implementing a radiation model for individual stars. Radiation feedback from massive stars affects star formation (Hislop et al., 2022) and outflows (Smith et al., 2021), effectively calming the evolution of dwarf galaxies, with significant effects on the mass-metallicity relation of ultra-faint galaxies Agertz et al. (2020). Adding radiation feedback to INFERNO is made easier by using the radiation transport model already implemented and tested in RAMSES-RT (Rosdahl et al., 2013). The difficulty lies in updating the model to incorporate the spectral energy distribution of individual stars. In principle, these spectra are available from various stellar evolution codes (e.g., SB99, Leitherer et al., 1999). With such an advanced radiation model, INFERNO would allow for studies of how radiation feedback affects, e.g., outflows, but also detailed hydrodynamical studies of Strömgren sphere evolution around individual stars in a full galactic context. To the best of my knowledge, no such studies have yet been conducted.

As a final remark, star-by-star models will become an important part of the next generation of galaxy simulations. In the past decades, shifts toward a theoretical understanding of the Universe have been facilitated by linking different fields of astrophysical research. Star-by-star models will serve as the link between stars as individual objects and as collections that make up galaxies.

References

Agertz O., et al., 2007, MNRAS, 380, 963

Agertz O., Kravtsov A. V., Leitner S. N., Gnedin N. Y., 2013, ApJ, 770, 25

Agertz O., et al., 2020, MNRAS, 491, 1656

Agertz O., et al., 2021, MNRAS, 503, 5826

Alongi M., Bertelli G., Bressan A., Chiosi C., Fagotto F., Greggio L., Nasi E., 1993, A&AS, 97, 851

Andersson E. P., Agertz O., Renaud F., 2020, MNRAS, 494, 3328

Andersson E. P., Renaud F., Agertz O., 2021, MNRAS, 502, L29

Andersson E. P., Agertz O., Renaud F., Teyssier R., 2022, arXiv e-prints, p. arXiv:2209.06218

Bastian N., Covey K. R., Meyer M. R., 2010, ARA&A, 48, 339

Benson A. J., Džanović D., Frenk C. S., Sharples R., 2007, MNRAS, 379, 841

Bertelli G., Bressan A., Chiosi C., Fagotto F., Nasi E., 1994, A&AS, 106, 275

Bigiel F., Leroy A., Walter F., Brinks E., de Blok W. J. G., Madore B., Thornley M. D., 2008, AJ, 136, 2846

Bigiel F., Leroy A., Walter F., Blitz L., Brinks E., de Blok W. J. G., Madore B., 2010, AJ, 140, 1194

Binney J., Tremaine S., 2008, Galactic Dynamics: Second Edition. Princeton University Press

Blaauw A., 1961, Bulletin of the Astronomical Institutes of the Netherlands, 15, 265

Blair G. N., Evans N. J. I., Vanden Bout P. A., Peters W. L. I., 1978, ApJ, 219, 896

Bland-Hawthorn J., Gerhard O., 2016, ARA&A, 54, 529

Blanton M. R., et al., 2003, ApJ, 592, 819

Blitz L., Thaddeus P., 1980, ApJ, 241, 676

Bolatto A. D., et al., 2011, ApJ, 741, 12

Bouché N., Hohensee W., Vargas R., Kacprzak G. G., Martin C. L., Cooke J., Churchill C. W., 2012, MNRAS, 426, 801

Bressan A., Fagotto F., Bertelli G., Chiosi C., 1993, A&AS, 100, 647

Bressert E., et al., 2012, A&A, 542, A49

Buck T., Rybizki J., Buder S., Obreja A., Macciò A. V., Pfrommer C., Steinmetz M., Ness M., 2021, MNRAS, 508, 3365

Buder S., et al., 2021, Monthly Notices of the Royal Astronomical Society, 506, 150

Calura F., et al., 2022, MNRAS,

Chabrier G., 2003, PASP, 115, 763

Chandrasekhar S., 1931, ApJ, 74, 81

Chevance M., Krumholz M. R., McLeod A. F., Ostriker E. C., Rosolowsky E. W., Sternberg A., 2022, arXiv e-prints, p. arXiv:2203.09570

Chiappini C., Matteucci F., Gratton R., 1997, ApJ, 477, 765

Chisholm J., Tremonti C. A., Leitherer C., Chen Y., 2017, MNRAS, 469, 4831

Chisholm J., Tremonti C., Leitherer C., 2018, MNRAS, 481, 1690

Clowe D., Gonzalez A., Markevitch M., 2004, ApJ, 604, 596

Colombo D., et al., 2014, ApJ, 784, 3

Crosthwaite L. P., Turner J. L., 2007, AJ, 134, 1827

Crutcher R. M., 2012, ARA&A, 50, 29

Dame T. M., et al., 1987, ApJ, 322, 706

Dame T. M., Hartmann D., Thaddeus P., 2001, ApJ, 547, 792

Dekel A., Silk J., 1986, ApJ, 303, 39

Dickinson C., et al., 2004, MNRAS, 353, 732

Drew J. E., Monguió M., Wright N. J., 2021, MNRAS, 508, 4952

Driver S. P., et al., 2012, MNRAS, 427, 3244

Dyson J. E., Williams D. A., 1997, The physics of the interstellar medium. Institute of Physics Publishing, doi:10.1201/9780585368115

Einstein A., 1915, Sitzungsberichte der Königlich Preußischen Akademie der Wissenschaften (Berlin, pp 844–847

Eldridge J. J., Stanway E. R., 2009, MNRAS, 400, 1019

Eldridge J. J., Izzard R. G., Tout C. A., 2008, MNRAS, 384, 1109

Eldridge J. J., Langer N., Tout C. A., 2011, MNRAS, 414, 3501

Emerick A., Bryan G. L., Mac Low M.-M., 2018, ApJL, 865, L22

Emerick A., Bryan G. L., Mac Low M.-M., 2020, arXiv e-prints, p. arXiv:2007.03702

Emsellem E., et al., 2022, A&A, 659, A191

Esmerian C. J., Kravtsov A. V., Hafen Z., Faucher-Giguère C.-A., Quataert E., Stern J., Kereš D., Wetzel A., 2021, MNRAS, 505, 1841

Evans Neal J. I., Heiderman A., Vutisalchavakul N., 2014, ApJ, 782, 114

Event Horizon Telescope Collaboration et al., 2019, ApJL, 875, L1

Event Horizon Telescope Collaboration et al., 2022, ApJL, 930, L12

Fabian A. C., 2012, ARA&A, 50, 455

Ferland G. J., Korista K. T., Verner D. A., Ferguson J. W., Kingdon J. B., Verner E. M., 1998, PASP, 110, 761

Fielding D., Quataert E., Martizzi D., Faucher-Giguère C.-A., 2017, MNRAS, 470, L39

Friedmann A., 1922, Zeitschrift fur Physik, 10, 377

Gaia Collaboration et al., 2016, A&A, 595, A2

Gaia Collaboration et al., 2021, A&A, 649, A1

Gaia Collaboration et al., 2022, arXiv e-prints, p. arXiv:2206.05534

Galilei G., 1610, Sidereus Nuncius

Geha M., et al., 2013, ApJ, 771, 29

Gentry E. S., Krumholz M. R., Dekel A., Madau P., 2017, MNRAS, 465, 2471

Gentry E. S., Krumholz M. R., Madau P., Lupi A., 2019, MNRAS, 483, 3647

Gies D. R., 1987, ApJS, 64, 545

Gies D. R., Bolton C. T., 1986, ApJS, 61, 419

Godunov S., Bohachevsky I., 1959, Matematičeskij sbornik, 47, 271

Grisdale K., Agertz O., Romeo A. B., Renaud F., Read J. I., 2017, MNRAS, 466, 1093

Grisdale K., Agertz O., Renaud F., Romeo A. B., Devriendt J., Slyz A., 2019, MNRAS, 486, 5482

Grudić M. Y., Guszejnov D., Hopkins P. F., Offner S. S. R., Faucher-Giguère C.-A., 2021, MNRAS, 506, 2199

Guillet T., Teyssier R., 2011, Journal of Computational Physics, 230, 4756

Guszejnov D., Grudić M. Y., Hopkins P. F., Offner S. S. R., Faucher-Giguère C.-A., 2021, MNRAS, 502, 3646

Guszejnov D., Markey C., Offner S. S. R., Grudić M. Y., Faucher-Giguère C.-A., Rosen A. L., Hopkins P. F., 2022a, MNRAS, 515, 167

Guszejnov D., Grudić M. Y., Offner S. S. R., Faucher-Giguère C.-A., Hopkins P. F., Rosen A. L., 2022b, MNRAS, 515, 4929

Gutcke T. A., Pakmor R., Naab T., Springel V., 2021, MNRAS, 501, 5597

Gutcke T. A., Pfrommer C., Bryan G. L., Pakmor R., Springel V., Naab T., 2022a, arXiv e-prints, p. arXiv:2209.03366

Gutcke T. A., Pakmor R., Naab T., Springel V., 2022b, MNRAS, 513, 1372

Haardt F., Madau P., 1996, ApJ, 461, 20

Harten A., Lax P. D., Leer B. v., 1983, SIAM review, 25, 35

Haugbølle T., Padoan P., Nordlund Å., 2018, ApJ, 854, 35

Helmi A., 2020, ARA&A, 58, 205

Helmi A., Babusiaux C., Koppelman H. H., Massari D., Veljanoski J., Brown A. G. A., 2018, Nature, 563, 85

Hennebelle P., Chabrier G., 2011, ApJL, 743, L29

Heyer M., Dame T. M., 2015, ARA&A, 53, 583

Hill D. T., Driver S. P., Cameron E., Cross N., Liske J., Robotham A., 2010, MNRAS, 404, 1215

Hinshaw G., et al., 2007, ApJS, 170, 288

Hirai Y., Fujii M. S., Saitoh T. R., 2021, PASJ, 73, 1036

Hislop J. M., Naab T., Steinwandel U. P., Lahén N., Irodotou D., Johansson P. H., Walch S., 2022, MNRAS, 509, 5938

Hockney R. W., Eastwood J. W., 1988, Computer Simulation Using Particles. CRC Press, doi:https://doi.org/10.1201/9780367806934

Hopkins P. F., 2015, MNRAS, 450, 53

Hopkins P. F., Kereš D., Oñorbe J., Faucher-Giguère C.-A., Quataert E., Murray N., Bullock J. S., 2014, MNRAS, 445, 581

Hopkins P. F., et al., 2018, MNRAS, 480, 800

Hu C.-Y., 2019, MNRAS, 483, 3363

Hu C.-Y., Naab T., Walch S., Glover S. C. O., Clark P. C., 2016, MNRAS, 458, 3528

Hu C.-Y., et al., 2022, arXiv e-prints, p. arXiv:2208.10528

Hubble E. P., 1926, ApJ, 64, 321

Hubble E., 1929a, Proceedings of the National Academy of Science, 15, 168

Hubble E. P., 1929b, ApJ, 69, 103

Hurley J. R., Pols O. R., Tout C. A., 2000, MNRAS, 315, 543

Hurley J. R., Tout C. A., Pols O. R., 2002, MNRAS, 329, 897

Izzard R. G., Dray L. M., Karakas A. I., Lugaro M., Tout C. A., 2006, A&A, 460, 565

Janka H.-T., 2012, Annual Review of Nuclear and Particle Science, 62, 407

Jeans J. H., 1902, Philosophical Transactions of the Royal Society of London Series A, 199, 1

Jones W. C., et al., 2006, ApJ, 647, 823

Jönsson H., et al., 2020, AJ, 160, 120

Kant I., 1755, Allgemeine Naturgeschichte und Theorie des Himmels

Kapteyn J. C., 1922, ApJ, 55, 302

Katz N., 1992, ApJ, 391, 502

Keller B. W., Wadsley J., Benincasa S. M., Couchman H. M. P., 2014, MNRAS, 442, 3013

Keller B. W., Wadsley J., Couchman H. M. P., 2016, MNRAS, 463, 1431

Kelvin L. S., et al., 2014, MNRAS, 439, 1245

Kennicutt Robert C. J., 1989, ApJ, 344, 685

Kennicutt Robert C. J., 1998, ApJ, 498, 541

Kennicutt R. C., Evans N. J., 2012, ARA&A, 50, 531

Kennicutt Robert C. J., et al., 2007, ApJ, 671, 333

Kim C.-G., Ostriker E. C., 2015, ApJ, 802, 99

Kim W.-T., Kim C.-G., Ostriker E. C., 2020a, ApJ, 898, 35

Kim C.-G., et al., 2020b, ApJL, 903, L34

King A., Pounds K., 2015, ARA&A, 53, 115

Kippenhahn R., Weigert A., Weiss A., 2013, Stellar Structure and Evolution. Springer Berlin, Heidelberg, doi:10.1007/978-3-642-30304-3

Kobayashi C., Umeda H., Nomoto K., Tominaga N., Ohkubo T., 2006, ApJ, 653, 1145

Kobayashi C., Karakas A. I., Lugaro M., 2020, ApJ, 900, 179

Kokaia G., Davies M. B., 2019, MNRAS, 489, 5165

Krause M. G. H., et al., 2020, SSRv, 216, 64

Kroupa P., 2001, MNRAS, 322, 231

Kroupa P., Tout C. A., Gilmore G., 1993, MNRAS, 262, 545

Kroupa P., Weidner C., Pflamm-Altenburg J., Thies I., Dabringhausen J., Marks M., Maschberger T., 2013, The Stellar and Sub-Stellar Initial Mass Function of Simple and Composite Populations. Springer Netherlands, doi:10.1007/978-94-007-5612-0_4

Krumholz M. R., 2015, arXiv e-prints, p. arXiv:1511.03457

Krumholz M. R., Tan J. C., 2007, ApJ, 654, 304

Krumholz M. R., Klein R. I., McKee C. F., Offner S. S. R., Cunningham A. J., 2009a, Science, 323, 754

Krumholz M. R., McKee C. F., Tumlinson J., 2009b, ApJ, 699, 850

Kuo C. L., et al., 2004, ApJ, 600, 32

Lada C. J., 1976, ApJS, 32, 603

Lada C. J., Lada E. A., 2003, ARA&A, 41, 57

Lahén N., Naab T., Johansson P. H., Elmegreen B., Hu C.-Y., Walch S., Steinwandel U. P., Moster B. P., 2020, ApJ, 891, 2

Lamb J. B., Oey M. S., Segura-Cox D. M., Graus A. S., Kiminki D. C., Golden-Marx J. B., Parker J. W., 2016, ApJ, 817, 113

Larson R. B., 1981, MNRAS, 194, 809

Lee E. J., Miville-Deschênes M.-A., Murray N. W., 2016, ApJ, 833, 229

Lee J. C., et al., 2022, ApJS, 258, 10

Leitherer C., et al., 1999, The Astrophysical Journal Supplement Series, 123, 3

Leitherer C., Ortiz Otálvaro P. A., Bresolin F., Kudritzki R.-P., Lo Faro B., Pauldrach A. W. A., Pettini M., Rix S. A., 2010, ApJS, 189, 309

Leitherer C., Ekström S., Meynet G., Schaerer D., Agienko K. B., Levesque E. M., 2014, ApJS, 212, 14

Lemaître G., 1927, Annales de la Socièacute;tèacute; Scientifique de Bruxelles, 47, 49

Leroy A. K., et al., 2013, AJ, 146, 19

Leroy A. K., et al., 2015, ApJ, 814, 83

Li M., Bryan G. L., 2020, ApJL, 890, L30

Li H. B., Goodman A., Sridharan T. K., Houde M., Li Z. Y., Novak G., Tang K. S., 2014, in Beuther H., Klessen R. S., Dullemond C. P., Henning T., eds, Protostars and Planets VI. p. 101 (arXiv:1404.2024), doi:10.2458/azu_uapress_9780816531240-ch005

Liang F.-H., Li C., Li N., Zhou S., Yan R., Mo H., Zhang W., 2021, ApJ, 923, 120

Loveday J., et al., 2012, MNRAS, 420, 1239

Lundmark K., 1930, Meddelanden fran Lunds Astronomiska Observatorium Serie I, 125, 1

Lynds C. R., Sandage A. R., 1963, ApJ, 137, 1005

Ma X., Hopkins P. F., Wetzel A. R., Kirby E. N., Anglés-Alcázar D., Faucher-Giguère C.-A., Kereš D., Quataert E., 2017, MNRAS, 467, 2430

Mackereth J. T., Crain R. A., Schiavon R. P., Schaye J., Theuns T., Schaller M., 2018, MNRAS, 477, 5072

Maíz Apellániz J., Pantaleoni González M., Barbá R. H., Simón-Díaz S., Negueruela I., Lennon D. J., Sota A., Trigueros Páez E., 2018, A&A, 616, A149

Maoz D., Graur O., 2017, ApJ, 848, 25

McKee C. F., Ostriker J. P., 1977, ApJ, 218, 148

McKee C. F., Ostriker E. C., 2007, ARA&A, 45, 565

McQuinn M., 2016, ARA&A, 54, 313

McQuinn K. B. W., van Zee L., Skillman E. D., 2019, ApJ, 886, 74

Ménard B., Scranton R., Fukugita M., Richards G., 2010, MNRAS, 405, 1025

Mikkola D., McMillan P. J., Hobbs D., 2020, MNRAS, 495, 3295

Miller G. E., Scalo J. M., 1979, ApJS, 41, 513

Miville-Deschênes M.-A., Murray N., Lee E. J., 2017, ApJ, 834, 57

Mo H., van den Bosch F. C., White S., 2010, Galaxy Formation and Evolution. Cambridge University Press, doi:10.1017/CBO9780511807244

Montero-Dorta A. D., Prada F., 2009, MNRAS, 399, 1106

Moore B., 1994, Nature, 370, 629

Muratov A. L., Kereš D., Faucher-Giguère C.-A., Hopkins P. F., Quataert E., Murray N., 2015, MNRAS, 454, 2691

Murray N., Quataert E., Thompson T. A., 2005, ApJ, 618, 569

Naab T., Ostriker J. P., 2017, ARA&A, 55, 59

Navarro J. F., Frenk C. S., White S. D. M., 1996, ApJ, 462, 563

Oey M. S., Lamb J. B., Kushner C. T., Pellegrini E. W., Graus A. S., 2013, ApJ, 768, 66

Oh S., Kroupa P., 2016, A&A, 590, A107

Onodera S., et al., 2010, ApJL, 722, L127

Oppenheimer B. D., et al., 2016, MNRAS, 460, 2157

Orkney M. D. A., et al., 2022, MNRAS, 515, 185

Ostriker E. C., McKee C. F., Leroy A. K., 2010, ApJ, 721, 975

Padoan P., Nordlund Å., 2011, ApJ, 730, 40

Padoan P., Haugbølle T., Nordlund Å., 2012, ApJL, 759, L27

Pandya V., et al., 2021, MNRAS, 508, 2979

Parker R. J., Goodwin S. P., 2007, MNRAS, 380, 1271

Pelkonen V. M., Padoan P., Haugbølle T., Nordlund Å., 2021, MNRAS, 504, 1219

Pignatari M., et al., 2016, ApJS, 225, 24

Planck Collaboration et al., 2020a, A&A, 641, A1

Planck Collaboration et al., 2020b, A&A, 641, A6

Portegies Zwart S. F., McMillan S. L. W., Gieles M., 2010, ARA&A, 48, 431

Poveda A., Ruiz J., Allen C., 1967, Boletin de los Observatorios Tonantzintla y Tacubaya, 4, 86

Prgomet M., Rey M. P., Andersson E. P., Segovia Otero A., Agertz O., Renaud F., Pontzen A., Read J. I., 2022, MNRAS, 513, 2326

Raiteri C. M., Villata M., Navarro J. F., 1996, A&A, 315, 105

Read J. I., Agertz O., Collins M. L. M., 2016, MNRAS, 459, 2573

Readhead A. C. S., et al., 2004, ApJ, 609, 498

Renaud F., Kraljic K., Bournaud F., 2012, ApJL, 760, L16

Renaud F., Bournaud F., Kraljic K., Duc P. A., 2014, MNRAS, 442, L33

Renaud F., Bournaud F., Agertz O., Kraljic K., Schinnerer E., Bolatto A., Daddi E., Hughes A., 2019, A&A, 625, A65

Renaud F., Agertz O., Read J. I., Ryde N., Andersson E. P., Bensby T., Rey M. P., Feuillet D. K., 2021, MNRAS, 503, 5846

Renzo M., et al., 2019, A&A, 624, A66

Rey M. P., Pontzen A., Agertz O., Orkney M. D. A., Read J. I., Rosdahl J., 2020, MNRAS, 497, 1508

Ritter C., Herwig F., Jones S., Pignatari M., Fryer C., Hirschi R., 2018, MNRAS, 480, 538

Robertson H. P., 1936, ApJ, 83, 257

Robertson B. E., 2021, arXiv e-prints, p. arXiv:2110.13160

Roca-Fàbrega S., et al., 2021, ApJ, 917, 64

Rosdahl J., Blaizot J., Aubert D., Stranex T., Teyssier R., 2013, MNRAS, 436, 2188

Rosen A., Bregman J. N., 1995, ApJ, 440, 634

Rosolowsky E., 2005, PASP, 117, 1403

Rosolowsky E., et al., 2021, MNRAS, 502, 1218

Salim D. M., Federrath C., Kewley L. J., 2015, ApJL, 806, L36

Salpeter E. E., 1955, ApJ, 121, 161

Samtleben D., Staggs S., Winstein B., 2007, Annual Review of Nuclear and Particle Science, 57, 245

Sandage A., 2005, ARA&A, 43, 581

Scannapieco E., Brüggen M., 2015, ApJ, 805, 158

Schaye J., 2004, ApJ, 609, 667

Schechter P., 1976, ApJ, 203, 297

Schmidt M., 1959, ApJ, 129, 243

Schroetter I., et al., 2019, MNRAS, 490, 4368

Schruba A., et al., 2017, ApJ, 835, 278

Schuller F., et al., 2021, MNRAS, 500, 3064

Schuster K. F., Kramer C., Hitschfeld M., Garcia-Burillo S., Mookerjea B., 2007, A&A, 461, 143

Scoville N. Z., Yun M. S., Clemens D. P., Sanders D. B., Waller W. H., 1987, ApJS, 63, 821

Sedov L. I., 1959, Similarity and Dimensional Methods in Mechanics. Academic Press, New York

Segovia Otero Á., Renaud F., Agertz O., 2022, MNRAS, 516, 2272

Seitenzahl I. R., et al., 2013, MNRAS, 429, 1156

Sellwood J. A., Binney J. J., 2002, MNRAS, 336, 785

Semenov V. A., Kravtsov A. V., Gnedin N. Y., 2017, ApJ, 845, 133

Semenov V. A., Kravtsov A. V., Gnedin N. Y., 2018, ApJ, 861, 4

Shapley H., Curtis H. D., 1921, Bulletin of the National Research Council, 2, 171

Shopbell P. L., Bland-Hawthorn J., 1998, ApJ, 493, 129

Shull J. M., Smith B. D., Danforth C. W., 2012, ApJ, 759, 23

Simon J. D., 2019, ARA&A, 57, 375

Smith R. J., 2020, ARA&A, 58, 577

Smith M. C., 2021, MNRAS, 502, 5417

Smith B. D., et al., 2017, MNRAS, 466, 2217

Smith R. J., et al., 2020, MNRAS, 492, 1594

Smith M. C., Bryan G. L., Somerville R. S., Hu C.-Y., Teyssier R., Burkhart B., Hernquist L., 2021, MNRAS, 506, 3882

Solomon P. M., Rivolo A. R., Barrett J., Yahil A., 1987, ApJ, 319, 730

Somerville R. S., Davé R., 2015, ARA&A, 53, 51

Sormani M. C., Treß R. G., Klessen R. S., Glover S. C. O., 2017, MNRAS, 466, 407

Spergel D. N., et al., 2007, ApJS, 170, 377

Spitoni E., Matteucci F., 2011, A&A, 531, A72

Spitoni E., Calura F., Matteucci F., Recchi S., 2010, A&A, 514, A73

Springel V., 2005, MNRAS, 364, 1105

Springel V., 2016, Saas-Fee Advanced Course, 43, 251

Steinwandel U. P., Bryan G. L., Somerville R. S., Hayward C. C., Burkhart B., 2022, arXiv e-prints, p. arXiv:2205.09774

Stone R. C., 1979, ApJ, 232, 520

Stone R. C., 1991, AJ, 102, 333

Su Y., et al., 2019, ApJS, 240, 9

Sutherland R. S., Dopita M. A., 1993, ApJS, 88, 253

Taylor G., 1950, Proceedings of the Royal Society of London Series A, 201, 159

Tetzlaff N., Neuhäuser R., Hohle M. M., 2011, MNRAS, 410, 190

Teyssier R., 2002, A&A, 385, 337

Toro E., 2009, Riemann Solvers and Numerical Methods for Fluid Dynamics: A Practical Introduction. Springer Berlin Heidelberg, `https://books.google.se/books?id=SqEjX0um8o0C`

Townsley L. K., Broos P. S., Feigelson E. D., Brandl B. R., Chu Y.-H., Garmire G. P., Pavlov G. G., 2006, AJ, 131, 2140

Tumlinson J., Peeples M. S., Werk J. K., 2017, ARA&A, 55, 389

Turatto M., 2003, in Weiler K., ed., , Vol. 598, Supernovae and Gamma-Ray Bursters. Springer Berlin Heidelberg, pp 21–36, doi:10.1007/3-540-45863-8_3

Umemoto T., et al., 2017, PASJ, 69, 78

Vargas L. C., Geha M., Kirby E. N., Simon J. D., 2013, ApJ, 767, 134

Vázquez G. A., Leitherer C., 2005, ApJ, 621, 695

Veilleux S., Cecil G., Bland-Hawthorn J., 2005, ARA&A, 43, 769

Veilleux S., Maiolino R., Bolatto A. D., Aalto S., 2020, A&A Rv, 28, 2

Walborn N. R., Maíz-Apellániz J., Barbá R. H., 2002, AJ, 124, 1601

Walch S., et al., 2015, MNRAS, 454, 238

Walker A. G., 1937, Proceedings of the London Mathematical Society, 42, 90

Wheeler C., et al., 2019, MNRAS, 490, 4447

Williams J. P., McKee C. F., 1997, ApJ, 476, 166

Wilson R. W., Jefferts K. B., Penzias A. A., 1970, ApJL, 161, L43

Wong T., Blitz L., 2002, ApJ, 569, 157

Woosley S. E., Bloom J. S., 2006, ARA&A, 44, 507

Wright T., 1750, An Original Theory or New Hypothesis of the Universe, Founded upon the Laws of Nature

Wyder T. K., et al., 2009, ApJ, 696, 1834

Zinnecker H., 1984, MNRAS, 210, 43

de Vaucouleurs G., 1948, Annales d'Astrophysique, 11, 247

de Wit W. J., Testi L., Palla F., Zinnecker H., 2005, A&A, 437, 247

van der Kruit P. C., Freeman K. C., 2011, ARA&A, 49, 301

Part II

Scientific publications

Author contributions

A summary of my contribution to each paper included in this thesis.

Paper I

How runaway stars boost galactic outflows

E.P. Andersson, O. Agertz, F. Renaud (2020)
Monthly Notices of the Royal Astronomical Society, vol. 494, 3328 (14 pp.)

Oscar Agertz (OA) provided the original idea for this project. The project was led by Eric Andersson (EA), and the project idea evolved through weekly discussions including EA, OA and Florent Renaud (FR). Numerical simulations for the project was conducted with a modified version of the public code RAMSES (provided by OA), and further developed by EA to suit the needs of the project. Simulations were performed and analyzed by EA. Final paper was written by EA, with comments and corrections provided by OA and FR.

Paper II

Runaway stars masquerading as star formation in galactic outskirts

E.P. Andersson, F. Renaud, O. Agertz (2021)
Monthly Notices of the Royal Astronomical Society, vol. 502, L29 (6 pp.)

The project idea was an extension of results found by EA in Paper I, which was given a broader context by OA. The project evolved through discussions between EA, FR and OA. The project was led by EA, who performed all analysis, and wrote the final paper. Comments and corrections were provided by FR and OA.

Paper III

INFERNO: Galactic winds in dwarf galaxies with star-by-star simulations including runaway stars

E.P. Andersson, O. Agertz, F. Renaud, R. Teyssier (2022)
Submitted to MNRAS (17 pp.)

The original idea came through discussions between EA and OA. The project was led by EA. The code used (RAMSES) was adapted to suit the needs of the project by EA, initial conditions for the simulations was provided by Romain Teyssier (RT), and all numerical simulations was performed by EA. Data was analyzed by EA, who wrote the final paper. Comments and corrections provided by OA, FR, and RT.

Paper I

Monthly Notices of the ROYAL ASTRONOMICAL SOCIETY

MNRAS **494,** 3328–3341 (2020) doi:10.1093/mnras/staa889
Advance Access publication 2020 April 7

How runaway stars boost galactic outflows

Eric P. Andersson ,★ Oscar Agertz and Florent Renaud
Department of Astronomy and Theoretical Physics, Lund Observatory, Box 43, SE-221 00 Lund, Sweden

Accepted 2020 March 26. Received 2020 March 26; in original form 2020 February 17

ABSTRACT

Roughly 10 per cent of OB stars are kicked out of their natal clusters before ending their life as supernovae. These so-called runaway stars can travel hundreds of parsecs into the low-density interstellar medium, where momentum and energy from stellar feedback is efficiently deposited. In this work, we explore how this mechanism affects large-scale properties of the galaxy, such as outflows. To do so we use a new model that treats OB stars and their associated feedback processes on a star-by-star basis. With this model, we compare two hydrodynamical simulations of Milky Way-like galaxies, one where we include runaways, and one where we ignore them. Including runaway stars leads to twice as many supernovae explosions in regions with gas densities ranging from 10^{-5} cm^{-3} to 10^{-3} cm^{-3}. This results in more efficient heating of the inter-arm regions, and drives strong galactic winds with mass loading factors boosted by up to one order of magnitude. These outflows produce a more massive and extended multiphase circumgalactic medium, as well as a population of dense clouds in the halo. Conversely, since less energy and momentum is released in the dense star-forming regions, the cold phase of the interstellar medium is less disturbed by feedback effects.

Key words: stars: massive – galaxies: evolution – galaxies: star formation.

1 INTRODUCTION

The Λ-cold dark matter has been highly successful in explaining and predicting a variety of observed properties, such as large-scale structure, halo clustering, and galaxy scaling relations (Eisenstein et al. 2005; Springel et al. 2005; Viel et al. 2008; Reid et al. 2010; Klypin, Trujillo-Gomez & Primack 2011; Komatsu et al. 2011; Somerville & Davé 2015). None the less, this model has also encountered challenges related to the 'baryon cycle', i.e. how galaxies accrete and expel their gas. Galaxy formation is an inefficient process, with at most $\sim$1/3 of the cosmological baryon fraction being turned into stars in galaxies as massive as the Milky Way, and significantly less in dwarf galaxies (e.g. Behroozi et al. 2019). This notion has been notoriously difficult to predict by numerical simulations of galaxy formation, which historically have suffered from excessive gas cooling and loss of angular momentum, leading to simulated galaxies with little in common with observations (for a review on this topic, see Naab & Ostriker 2017).

Galactic outflows, driven by stellar feedback (Dekel & Silk 1986) and active galactic nuclei (Benson et al. 2003), are commonly believed to be instrumental for solving these problems (Somerville & Davé 2015). In the past decades, many studies have explored ways of numerically capturing the impact of stellar feedback processes on the interstellar medium (ISM), e.g. effects from supernovae (SNe) explosions, stellar winds, radiation from young stars (see e.g. Katz 1992; Stinson et al. 2006; Agertz et al. 2013; Keller et al. 2014; Simpson et al. 2015; Hopkins et al. 2018). This effort has made it possible to model galactic outflows in a cosmological context as an emergent property of clustered star formation, with simulations now matching a range of observed galaxy properties (e.g. Hopkins et al. 2014; Agertz & Kravtsov 2015, 2016), as well as properties of the turbulent ISM and giant molecular clouds (GMCs; Grisdale et al. 2017, 2018, 2019).

Adding to the success of stellar feedback models, simulations of entire galaxies have improved significantly in the recent years with parsec, or even sub-parsec spatial resolution and mass resolution reaching a few solar masses enabling models to capture the dense, cold ISM (see e.g. Renaud et al. 2013; Rosdahl et al. 2017; Wheeler et al. 2019; Agertz et al. 2020). State-of-the-art simulations can now resolve most of the cooling radii of individual SN explosions that allows them to capture the build-up of momentum during the Sedov–Taylor phase which is crucial for robustly modelling SNe feedback (Kim & Ostriker 2015; Martizzi, Faucher-Giguère & Quataert 2015a). Furthermore, recent numerical studies have reached high enough resolution for individual stars to be modelled in galaxy scale simulations (Hu et al. 2017; Wheeler et al. 2019; Su et al. 2018; Emerick, Bryan & Mac Low 2019; Lahén et al. 2019). We stress however that despite the improvements in galaxy modelling in the past decade, (subgrid) stellar feedback still operates at the resolution level, with its coupling to the ISM not yet being fully understood (Ohlin, Renaud & Agertz 2019).

While the actual process of star formation is not yet captured in galactic context, these simulations allow for star particles to represent individual stars, all sampled from an initial mass function (IMF) with subsequent feedback processes emerging on a star-by-star basis rather than from macro particles representing entire stellar populations. However, while galaxy simulations have started to resolve the stellar component star by star, they are still far from treating the stars *collisionally*. While a collisionless approximation is valid on galactic scales, star–star interactions drive the internal

★ E-mail: eric@astro.lu.se

dynamics of dense star clusters. As a result, some fraction of OB stars are kicked out of their natal star clusters with velocities large enough to move them out of the dense star-forming gas before exploding as SNe (e.g. Gies & Bolton 1986; Gies 1987; Stone 1991; Hoogerwerf, de Bruijne & de Zeeuw 2000; Schilbach & Röser 2008; Jilinski et al. 2010; Silva & Napiwotzki 2011; Maíz Apellániz et al. 2018). Simulation of clusters (e.g. Oh & Kroupa 2016) reveal that such velocity kicks originates from gravitational interactions (Poveda, Ruiz & Allen 1967), including the disruption of binaries through SNe (Blaauw 1961). None of these effects can be taken into account self-consistently without collisional dynamics, which currently is computationally infeasible in galaxy scale simulations.

Massive runaway stars have been suspected to impact galaxy evolution through efficient injection of energy into low-density gas (Naab & Ostriker 2017). Coupling energy from SNe to gas depends both on the phase of the gas (Katz 1992; Ceverino & Klypin 2009) and on the structure of the ISM (Kim & Ostriker 2015; Martizzi, Faucher-Giguère & Quataert ; Walch & Naab 2015; Iffrig & Hennebelle 2015; Ohlin et al. 2019). Because runaway stars move away from their natal regions, SN energy from these objects ought to couple differently compared to the stars that remains in closer proximity to the dense star-forming gas. Typically, explosions in low-density gas generate a hot bubble that expands and leaves the galaxy as an outflow (Korpi et al. 1999; de Avillez 2000; de Avillez & Breitschwerdt 2004; Joung & Mac Low 2006). A similar effect has also been studied by comparing feedback from SNe positioned at density peaks compared to random positioning (see e.g. Korpi et al. 1999; de Avillez 2000; de Avillez & Breitschwerdt 2004, 2005; Joung & Mac Low 2006; Walch et al. 2015; Girichidis et al. 2016; Martizzi et al. 2016; Gatto et al. 2017). Although these experiments are idealized, targeting only a small patch of the galaxy, they demonstrate that feedback from randomly located SN tends to drive stronger outflows compared to explosions in density peaks. This potentially impact the way the host galaxy forms and evolves across cosmic time.

In this paper, we present a new model for treating individual stars, focusing on the effect of runaways. The model has been applied to simulations of an isolated disc galaxy with properties similar to the Milky Way. We describe how we model individual stars as well as our treatment of runaway stars in Section 2. The numerical set-up and results are described in Sections 3 and 4, respectively, while we discuss their implications in Section 5. Finally, we summarize in Section 6.

2 STAR FORMATION AND STELLAR FEEDBACK

In order to probe the effects of runaway stars, we implement a new recipe for treating massive stars as individual particle that evolves during the simulation. In this section, we describe the method used for sampling stars from an IMF, how feedback via winds and SNe is treated and how it chemically enriches the ISM.

2.1 Sampling the IMF

Treating massive stars as individual particles requires a method to sample stellar masses. To do this efficiently, we employ the method by Sormani et al. (2017). In a mass bin indexed by i, a number of stars n_i is determined through realizations of a Poisson distribution given by

$$\mathcal{P}_i(n_i) = \frac{\lambda_i^{n_i}}{n_i!} e^{-\lambda_i}, \tag{1}$$

where the mean of the distribution, λ_i, is given for each bin by

$$\lambda_i = f_i \frac{M}{m_i}, \tag{2}$$

where for bin i, in which stars have an average mass of m_i, there is a fraction of mass f_i out of the total mass M, available for star formation. The total stellar mass generated in N bins is then

$$M_{\rm sampled} = \sum_{i=1}^{N} n_i m_i, \tag{3}$$

which is approximately equal to the mass M, due to the stochastic sampling, but converges towards M for large numbers of stars. There are two properties of this method that makes it ideal for our simulations. First, the computational expense is determined by the number of adopted mass bins, since the method only samples one random number for each bin and not for every star. Secondly, the bin-sizes can be chosen arbitrarily, which allows for stars below a certain mass threshold to be grouped in a single bin, while stars above this mass are sampled at high-mass resolution.

A problem with this method is the non-zero probability of sampling a population of stars with mass larger than the available gas mass. To avoid this, we sample the IMF starting from the low-mass end until either reaching the most massive stars defined by the mass bins or until the available gas is depleted. In the first case, we return the extra mass to the gas parcel where it was initially collected, while in the second case we remove the most massive stars such that the stellar mass formed does not exceed the initial gas mass. This results in an IMF which is slightly more bottom heavy than the one originally targeted, which in principle could lead to weaken stellar feedback. None the less, this effect is negligible compared to the uncertainties in the models for stellar feedback.

Our model uses of the three part IMF from Kroupa (2001), where the number of stars of mass m is given by

$$\xi(m) = A C_j m^{-\alpha_j} \quad \text{for} \quad m_j \leq m < m_{j+1}, \tag{4}$$

where A is a normalization factor and C_j are constants that ensures continuity in the intersections given by $C_1 = 1$, $C_2 = C_1 m_2^{\alpha_2 - \alpha_1}$, and $C_3 = C_2 m_3^{\alpha_3 - \alpha_2}$. The three different parts are split into mass regimes given by $m_1 = 0.01$ M$_\odot$, $m_2 = 0.08$ M$_\odot$, $m_3 = 0.5$ M$_\odot$, and $m_4 = M_{\rm max}$, with slopes $\alpha_1 = 0.3$, $\alpha_2 = 1.3$, and $\alpha_3 = 2.3$. The normalization is determined for stars with masses between $M_{\rm min} = 0.01$ M$_\odot$ and $M_{\rm max} = 120$ M$_\odot$.

In this work, we sample stars from the aforementioned IMF at each star formation event. We divide stars into high-mass stars (HMS) and low-mass stars (LMS). The HMS are defined to have stellar masses larger than 8 M$_\odot$, sampled up to 40 M$_\odot$ using 100 equisized bins (giving a mass resolution of $\sim$0.3 M$_\odot$). We do not include stars more massive than 40 M$_\odot$ in our model. Such stars are both exceedingly rare and their short lifetimes means that the distance travelled by very massive runaway stars is short. However, these are extremely luminous important sources of feedback, especially in regards to stellar winds. Our model for stellar winds (described in detail in Section 2.3) has a strong scaling with stellar mass, and including these most massive stars can result in too strong early feedback. Furthermore, we assume core-collapse SNe for all HMS, which is unrealistic for too massive stars. In the code, all HMS are treated individual particles. Since we are interested in the effect of feedback from massive (>8 M$_\odot$) runaway stars, the rest of the IMF, defining

the LMS, are lumped together into a single macroparticle to reduce the computational cost.

2.2 Runaway stars

In the simulations, particles are treated in a collisionless manner. To simulate runaway stars, we give velocity kicks to all particles representing individual stars (i.e. $\geq$8 $M_\odot$) at their formation. The collisional effects leading to kicks operate on spatial scales many orders of magnitudes below the gravitational softening length of our simulations, warranting a 'sub-grid' approach.

The method assumes kicks distributed isotropically with velocities, v, sampled from a power-law distribution,

$$f_v \propto v^{-\beta}, \tag{5}$$

where the β is a free parameter in our model. The value of β depends on several factors. Dynamical scattering events that generate kicks typically involve the interaction between a hard binary and a third star. The frequency of such encounters will therefore not only depend on the relaxation time of the cluster, but must also be sensitive to the binary fraction. Moreover, as mentioned earlier, the kicks can also originate from the disruption of binary system caused by the SNe of one of the two components. This corroborates that binary fraction is an important parameter of the distribution of velocities. Furthermore, these processes imply a delay between the formation of a star and the time when it gets a kick. Because of the complexity of this problem, estimates of β typically demand the use of N-body simulations (see e.g. Eldridge, Langer & Tout 2011; Perets & Šubr 2012; Oh & Kroupa 2016; Renzo et al. 2019), but estimates from observations also exist (e.g. Hoogerwerf et al. 2000; Hoogerwerf, de Bruijne & de Zeeuw 2001). Furthermore, Banerjee, Kroupa & Oh (2012) found that the velocity distribution shows some dependence on the mass of the runaway stars, with more massive stars reaching higher velocities (in agreement with Oh & Kroupa 2016).

In this work, we choose a value of $\beta = 1.8$ and normalize the distribution for values between 3 and 385 km s^{-1}, which we apply to all HMS particles at formation without adding any time delay. This leads to $\sim$14 per cent stars with velocities $>$30 km s^{-1}. This choice is motivated by model MS3UQ_SP in Oh & Kroupa (2016), corresponding to runaways from a clusters with a mass of $10^{3.5}$ $M_\odot$ and half mass radii of 0.3 pc. Early observations indicated values for the runaway fraction of 30 per cent (Stone 1991); however, this is large compared to more recent work. As noted by Maíz Apellániz et al. (2018, see also Silva & Napiwotzki 2011), the results of Stone overestimate this fraction. Maíz Apellániz et al. found observational evidence that 10$-$12 per cent of O stars and a few per cent of B stars are so-called runaway stars with significant peculiar velocities ($>$30 km s^{-1}) with respect to their natal environment (in agreement with models by Eldridge et al. 2011; Renzo et al. 2019). Furthermore, the sampled velocities applied to the stars will change through gravitational forces acting on the stars throughout their lifetime. This change depends on the local gravitational field and the entire galactic potential for stars with long enough life times. This sensitivity to environment, together with the difficulty of comparing the observed population of runaway stars to the un-evolved velocity distribution, makes a simple universal model (e.g. equation 5) uncertain. The reader should be cautious of this and note that the results we present could overestimate the effect of runaway stars.

As a first approximation, one can naively compute the distance stars travel before exploding as SNe by multiplying their mean velocity with the average main-sequence lifetime in the appropriate mass range. Using the velocity distribution given by equation (5), we find that stars in the mass range of 8–40 $M_\odot$ with $Z = Z_\odot$[1] travels roughly 350 pc before exploding as supernova. This simple model does not take into account deceleration from the gravitational field of the cluster from which it escapes, and is therefore an upper limit on the travel distance. None the less, it is of the same order of magnitude as more detailed studies (see e.g. Eldridge et al. 2011; Renzo et al. 2019). The distance is significant, being an order of magnitude larger than the average size of star-forming molecular clouds in the Milky Way (e.g. Heyer et al. 2009), and of the same order of magnitude as the scale height of the cold gas disc.

2.3 Stellar feedback

HMS particles are considered as individually evolving stars and we consider mass-loss, enrichment, momentum- and energy-injection from fast winds and core-collapse SNe. In massive stars ($\geq$8 $M_\odot$), radiation pressure is significant enough to push away their outer envelopes, giving rise to strong stellar winds for their entire main-sequence evolution (see e.g. Cassinelli & Lamers 1987; Willis & Garmany 1987). For this work, we employ a model with a mass-loss rate based on Dale & Bonnell (2008) given by

$$\dot{M} = 10^{-5} \left(\frac{M_\mathrm{b}}{30\,\mathrm{M}_\odot} \right)^4 Z^\gamma \,\mathrm{M}_\odot\,\mathrm{yr}^{-1}, \tag{6}$$

where M_b is the birth mass of the star. The scaling to the metallicity[2] was added to the mass-loss rate to account for the metallicity dependence of the photon coupling to the stellar envelope, which drives the wind. The metallicity exponent γ has been shown to range between 0.5 and 0.8 (Kudritzki, Pauldrach & Puls 1987; Vink, de Koter & Lamers 2001; Mokiem et al. 2007; Vink 2011) and in this work we adopt $\gamma = 0.5$. The velocity of the fast winds typically ranges between 1000 and 3000 km s^{-1} in the literature (see e.g. Leitherer, Robert & Drissen 1992; Lamers & Cassinelli 1999). We use a value $v_\mathrm{w} = 1000$ km s^{-1} for our model and inject the wind into the surrounding gas as a continuous source of momentum during the star's main sequence lifetime.

HMS stars explode as core-collapse SNe at the end of their main sequence. The main-sequence lifetime, t_MS, for a star given its mass and metallicity Z (here expressed as the total mass fraction in elements heavier than He). To determine t_MS our model uses a stellar age–mass–metallicity fit by Raiteri, Villata & Navarro (1996), who found

$$\log t_\mathrm{MS} = a_0(Z) + a_1(Z)\log m + a_2(Z)(\log m)^2, \tag{7}$$

where the coefficients are given by

$$\begin{aligned} a_0(Z) &= 10.13 + 0.07547\log Z - 0.008084(\log Z)^2, \\ a_1(Z) &= -4.424 - 0.7939\log Z - 0.1187(\log Z)^2, \\ a_2(Z) &= 1.262 + 0.3385\log Z + 0.05417(\log Z)^2. \end{aligned} \tag{8}$$

Note that this gives very similar main-sequence lifetimes compared to the single-star evolution (SSE) formulae by Hurley, Pols & Tout (2000). When a star explodes, we deposit 10^{51} erg of energy into the gas at the location of the star particle. If the SNe cooling radius

[1] In this work, we adopt $Z_\odot = 0.02$.

[2] We track iron (Fe) and oxygen (O) abundances separately, and advect them as passive scalars. To construct a total metal mass M_Z to use for feedback and cooling, via the metallicity $Z = M_Z/M_\mathrm{gas}$, we adopt $M_Z = 2.09M_\mathrm{O} + 1.06M_\mathrm{Fe}$ according to the mixture of α (C, N, O, Ne, Mg, Si, S) and iron (Fe, Ni) group elements relevant for the sun (Asplund et al. 2009).

is not resolved, hence the momentum built up during the Sedov–Taylor phase is not captured self-consistently, we explicitly inject the momentum from this phase following the scheme by Kim & Ostriker (2015, see also Martizzi et al. 2015). Our implementation is identical to that of Agertz, Romeo & Grisdale (2015) and Rhodin et al. (2019) and we refer the reader to these works for more details.

For LMS particles, we consider mass-loss, enrichment, momentum, and energy injection for type Ia SNe and asymptotic giant branch (AGB) winds. Details of the scheme can be found in Agertz et al. (2013), with the adopted Kroupa IMF (equation 4) truncated at the LMS upper mass limit (8 $M_\odot$).

3 NUMERICAL SET-UP

We have implemented the method described above in the *N*-body+Adaptive Mesh Refinement (AMR) code RAMSES (Teyssier 2002). RAMSES treat stars and dark matter through collisionless dynamics using the particle-mesh method (Hockney & Eastwood 1981; Klypin & Shandarin 1983), with the gravitational potential calculated by solving the Poisson equation using the multi-grid method (Guillet & Teyssier 2011) for all refinement levels. The fluid dynamics of the gas is calculated using a second-order unsplit Godunov method with an ideal mono-atomic gas with adiabatic index $\gamma = 5/3$. The code accounts for metallicity dependent cooling by using the tabulated cooling functions of Sutherland & Dopita (1993) for gas temperatures of $10^{4\text{-}8.5}$ K, and rates from Rosen & Bregman (1995) for cooling down to lower temperatures.

We have carried out two simulations of an isolated star forming galaxy: one where the high-mass single stars are initiated with the velocity kick from the velocity distribution given by equation (5) using $\beta = 1.4$ (referred to as `runaways`), and a control simulation where high-mass single stars are not assigned any velocity kick (referred to as `no runaways`) as in traditional galaxy simulations.

The initial conditions are those of the isolated disc galaxy in the AGORA project (Kim et al. 2014, 2016), set up to approximate a Milky Way-like galaxy following the methods described in Hernquist (1993) and Springel (2000). Briefly, the dark matter halo has a concentration parameter $c = 10$ and virial circular velocity $v_{200} = 150$ km s^{-1}. This translates into a halo virial mass $M_{200} = 1.1 \times 10^{12}$ $M_\odot$ within $R_{200} = 205$ kpc. The total baryonic disc mass is $M_{\rm disc} = 4.5 \times 10^{10}$ $M_\odot$ with 20 per cent in gas. The initial stellar and gaseous components follow exponential surface density profiles with scale lengths $r_{\rm d} = 3.4$ kpc and scale heights $h = 0.1 r_{\rm d}$. The bulge-to-disc mass ratio is 0.125. The bulge mass profile is that of Hernquist (1990) with scale-length $0.1 r_{\rm d}$. The halo and stellar disc are represented by 10^6 particles each, and the bulge consists of 10^5 particles.

The galaxies are simulated in a box with sides 600 kpc with adaptive mesh refinement allowing for a minimum cell size of 9 pc. The refinement strategy uses a quasi-Lagrangian approach that ensures a roughly constant number of particles ($\sim$8) in each cell that reduces discreteness effects (Romeo et al. 2008). Furthermore, the AMR scheme splits cells into eight new cells, each with mass $m_{\rm refine} = 4014$ $M_\odot$, when their sum of stellar and gas mass exceeds $8 \times m_{\rm refine}$. Star formation uses a standard procedure with the star formation rate density in cells exceeding a density threshold, $\rho_\star$, given by

$$\dot{\rho}_\star = \epsilon_{\rm SF} \frac{\rho_{\rm g}}{t_{\rm ff}} \text{ for } \rho_{\rm g} > \rho_\star, \quad (9)$$

where $\epsilon_{\rm SF}$ is the star formation efficiency per free-fall time, $\rho_{\rm g}$ is the cell gas density, and $t_{\rm ff} = \sqrt{3\pi/32G\rho}$ is the local gas free-fall time (see Agertz et al. 2013 for details). For this work, we adopt $\rho_\star = 100$ cm^{-3} and sample star particles with a mass resolution of 500 $M_\odot$, from which we remove mass for the HMS sampling at each star formation event. For the simulations considered here we use a constant $\epsilon_{\rm SF} = 5$ per cent. Observationally, the efficiency per free-fall time averages 1 per cent in Milky Way GMCs (Krumholz & Tan 2007), albeit with a large spread (Murray 2011; Lee, Miville-Deschênes & Murray 2016).

4 RESULTS

We re-emphasize that including runaway stars provides a means to relocate massive stars away from their dense formation sites before they end their lives in SNe, and our goal here is to explore how this process affects the evolution of a Milky Way-mass spiral galaxy.

The two galaxies are evolved for 250 Myr, a time during which they both are actively star forming. In the first 80 Myr the galaxies adjust to their initial conditions, and in the case of the `runaways` simulation there is a suppression in star formation after 120 Myr (approximately one orbital time at the disc scale radius). After these 120 Myr both simulations has stable star formation rate. In this work, all results taken as averages over time exclude this early phase unless otherwise stated.

Fig. 1 shows projections along the line of sight for luminosity, gas density, and temperature for the galaxies at time $t = 250$ Myr. Focusing first on the luminosity of the two galaxies, we find qualitative agreement between the two simulations, although we highlight that the `runaways` simulation has more stars in the inter-arm region as well as above and below the disc mid-plane. This indicates that the effect of runaway stars is subtle in the luminosity of the galaxy. However, the projected gas density and temperature largely differ between the two cases. Here runaway stars give rise to large ($\sim$ kpc), hot ($T > 10^6$ K) bubbles in the interarm regions, as well as more prominent outflows (as seen on the edge-on views) compared to the `no runaways` model. In general, the gaseous halo is more structured with warm ($T < 10^6$ K) clouds found far away from the disc ($\gtrsim$5 kpc) in the `runaways` simulation.

4.1 Star formation rates and ISM properties

We next consider the star formation rate (SFR) of the two simulations, shown in the upper panel of Fig. 2. Excluding the initial transient, both simulations have similar SFR (8–9 $M_\odot$ yr^{-1}) for the first 120 Myr, followed by a decrease to a SFR of 5–6 $M_\odot$ yr^{-1} in the `runaways` simulation for the remaining time. This decrease is linked to the depletion of cold ($T < 10^4$ K) gas, which is shown in the lower panel of Fig. 2. The simulation with runaway stars features less mass in the cold phase at all times, which ultimately leads to a decline in the SFR.[3]

During the period of high SFRs for both models (80 Myr $< t <$ 120 Myr), more cold gas disappears in the `runaways` simulation compared to the `no runaways` simulation. Quantitatively, the total cold gas mass decreases at approximately 30 and 15 $M_\odot$ yr^{-1} for `runaways` and `no runaways`, respectively. Since the SFR is similar in both simulations at this epoch (thus having similar amounts

[3]We note however that many other factors e.g. the level of gas turbulence, local star formation efficiency, GMC mass function will play a role in setting the global SFR.

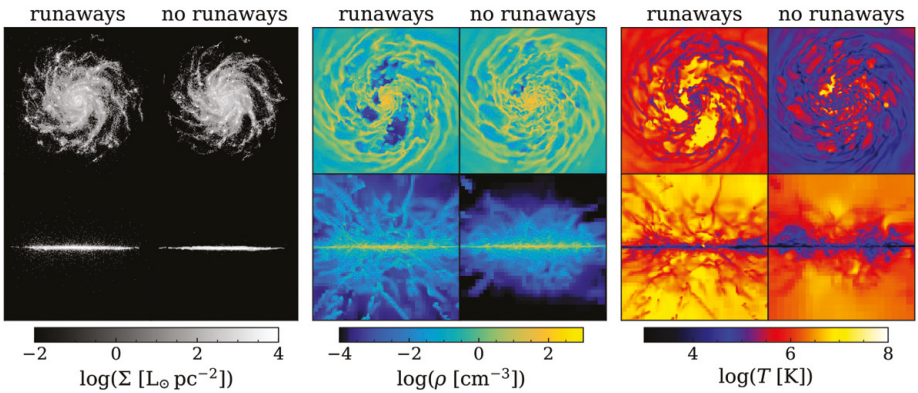

Figure 1. Projections of the stellar luminosity, gas density, and temperature for face-on view (top row) and edge-on view (bottom row) from the last output of the simulations, i.e. after 250 Myr of evolution. The side of each panel is 24 kpc. For each quantity, we show the simulation taking runaway stars into consideration to the left, whereas the simulation ignoring these stars is shown to the right.

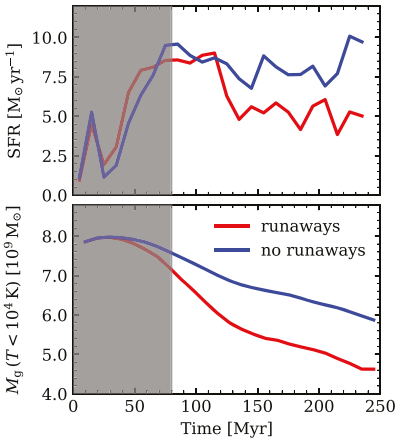

Figure 2. *Top*: Star formation rate as function of time for the simulations with and without runaway stars. We neglect the transient caused by the simulation adjusting to initial conditions (grey region). Both simulations reach a steady state after approximately 120 Myr, before which we see a quasi-stable period with enhanced SFR (starting at ≈80 Myr). There is a suppression in star formation at 120 Myr in the model including runaway stars. *Bottom:* Total mass of the cold ($< 10^4$ K) gas as function of time for the simulations, measured in a cylinder with a radii of 15 kpc and a thickness of 2 kpc.

of cold gas turning into stars), the `runaways` model must reduce the net gas mass more efficiently, either by removing it from this cold phase or inhibit warm gas from cooling more strongly compared to the `no runaways` model. To some extent both of these likely play a role. After 120 Myr, the cold gas mass-loss rate changes to 7–10 $M_\odot$ yr^{-1} in both simulations, with the `runaways` simulation now having less cold gas in total. For the `runaways` simulation, this transition coincides with the decrease in SFR. This implies that even at low SFR, more cold gas is lost per unit of stellar mass formed in the `runaways` simulation.

To understand why the model with runaway stars predicts a more rapid removal of the cold ISM from the galaxy, we focus to the runaway mechanism, namely the effect of relocating SNe progenitors. Fig. 3 shows the projected gas density for the cold ISM ($T < 10^4$ K). We selected outputs where both simulations included visible SN bubbles ($t = 200$ Myr). The propensity of feedback from runaway stars to create large bubbles in the inter-arm regions is evident. For the `runaways` simulation, there are young massive stars present in the voids, whereas for the `no runaways` all massive stars overlap with the low-mass star particles by design.

Initially, density contrasts are generated by stellar feedback and large-scale gravitational instabilities, some of which evolve into bubbles. A crucial difference is that with the inclusion of runaway stars, the bubbles are resupplied with SN progenitors that keep injecting energy and momentum into them even though actual star formation is impossible in those regions. This repeated injection gives rise to kpc-scale bubbles in the `runaways` model, and as we will discuss later it leads to energy venting into the CGM. Throughout the `runaways` simulation, many such bubbles form, albeit with seemingly random timing.

Quantitatively, we find a clear excess of SNe explosions in gas with 10^{-5} cm^{-3} $< \rho < 10^{-3}$ cm^{-3} when including runaways, peaking at more than twice as many explosions at $\rho \sim 10^{-4}$ cm^{-3} with respect to the `no runaways` case. This implies a direct injection of energy in low-density regions in contrast with the typical injection sites of SNe. This mechanism is visible in Fig. 3, and the resulting heating is visible in the face-on projection of the gas temperature in Fig. 1. Finally, we note that the `no runaways` simulation features, not surprisingly, more SNe in gas with higher density compared to the `runaways` simulation.

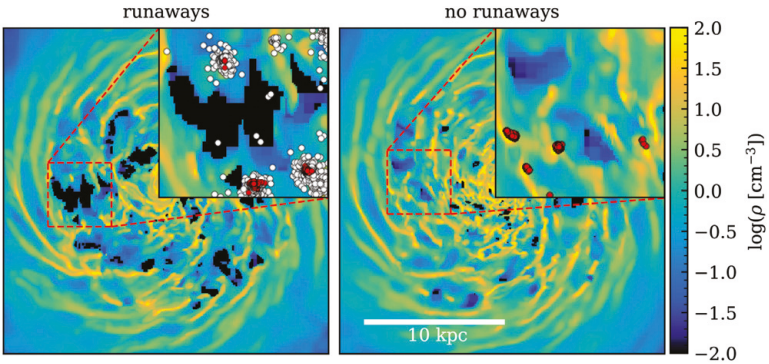

Figure 3. Projection plots of density for gas with temperature $<10^4$ K for the model with (left) and without (right) runaway stars. The zoom in regions (4.7 kpc wide) show the positions of young (<10 Myr, pre-SNe) star particles located within 50 pc of the mid-plane, with HMS particles in white and LMS particles in red. By construction, the two types exactly overlap in the no runaways case. In the runaways simulation, a few HMS have travelled to regions completely void of $<10^4$ K gas. These stars are likely to explode inside the bubble.

Despite this seemingly violent impact on the cold ISM, the overall structure of the disc remains intact. To some degree, runaway stars alleviate the dense star-forming gas from part of the feedback. This is demonstrated in Fig. 4 where we show the structure of the cold gas in the disc. The left plot shows the vertical distance from the mid-plane of the disc within which half of the cold gas mass is located as function of radius. In the right plot, we show the gas mass as function of vertical distance z. Although the introduction of runaway stars cause large bubbles in the inter-arm gas, the overall structure of the cold ISM is very similar in both simulations. In fact, runaway stars produce a slightly thinner disc. Furthermore, the vertical velocity dispersion of the cold gas is $\sigma_z \sim 20$ km s^{-1} at radius $R = 5$ kpc for both simulations, with a roughly linear decrease to $\sim$5 km s^{-1} at 10 kpc after which it flattens out. This is in close agreement with observed H I kinematics in nearby spiral galaxies (Tamburro et al. 2009). Hence, while runaway stars drive strong turbulence and creates large bubbles it does not strongly alter the morphology of the cold disc. This allows for the co-existence of thin galactic stellar discs and strong galactic outflows, an otherwise challenging aspect of galaxy models (e.g. Agertz, Teyssier & Moore 2011; Roškar et al. 2014).

In summary, runaway stars induce in more efficient coupling of feedback to diffuse gas. The more rapid depletion of the cold ISM found above is then a result of more vigorous galactic outflows that we quantify in the next section.

4.2 Galactic outflows

The top panel of Fig. 5 shows the vertical outflow rate as a function of time for both models. The rates are computed by summing cell-by-cell contributions in a cylindrical region with a radius of 12 kpc centred on the galaxy for 4 kpc $< |z| <$ 6 kpc, considering only gas flowing in the vertical direction away from the mid-plane. The galaxy with runaway stars features significantly stronger outflows at all times, and right after the onset of the galactic wind ($t > 80$ Myr) the mass-loss rate is more than 10 times higher than without runaway stars. This strong outflows in the runaways simulation is likely linked to the reduction in cold gas mass, causing the reduced SFR. At 150 Myr this wind calms down, although it still removes mass at roughly twice the rate of the no runaways model. Furthermore, there are burst of outflows (the largest of which takes place at 200 Myr) linked to runaway stars generating a number of large (>kpc) bubbles (apparent in the middle panel in Fig. 1).

In the bottom panel of Fig. 5, we present the evolution of the mass loading factor, defined as

$$\eta = \frac{\langle \dot{M} \rangle}{\mathrm{SFR}}. \tag{10}$$

Since η is very sensitive to the height where it is measured, we show it for three different $|z|$ corresponding to roughly 0.025, 0.25, and 0.5 times the virial radius of the galaxy. For a given model, η varies up to three orders of magnitude depending on where it is measured. However, the ratio between the simulations is mostly independent of where we measure it. We will return to this notion later as well in this section, as compare our models to observations in Section 5.3.

Focusing on the innermost measurement, we find that at 100 Myr, η reaches its maximum at $\approx$0.5 in the no runaways simulation. With the stronger outflows measured in the runaway model, combined with the reduced SFR, the mass loading factor is significantly higher throughout the entire duration of the simulation, with periods of η reaching values of $\sim$5–10. As we discuss further in Section 5.1, such an efficient wind driving implies a markedly different long-term evolution for the galaxy.

Higher outflow rates do not necessarily imply faster galactic winds. In fact, in the runaways simulation we find that warm outflows ($2 \times 10^4 < T < 10^6$ K) carry more mass but travel at a lower velocity (see the solid line in the bottom panel of Fig. 6) than in the no runaways simulation. If the galactic winds were purely momentum driven, the outflow mass would depend on the wind velocity as $m \propto 1/v$. We measure the velocity to be less than twice as high in the runaways that then would imply an outflow mass no more than twice as high. However, the strong outflows in runaways yield $\sim$3 times more gas mass in the halo (as shown in Section 4.3). Therefore, this feedback is not momentum driven. Conversely, in the case of purely energy-driven winds, one would expect $m \propto 1/v^2$, i.e.

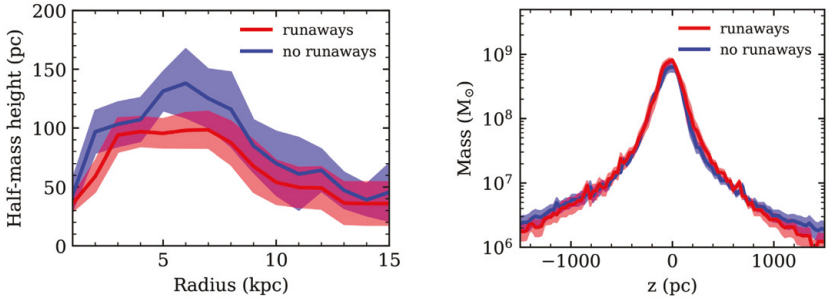

Figure 4. *Left:* Half-mass height of the cold ($< 10^4$ K) gas mass as function of radius. Solid line shows the mean of all outputs and coloured areas show the standard deviation. *Right:* Vertical profile of the gas mass in the `runaways` simulation (red) and the `no runaways` simulation (blue). The filled line shows the mean of all outputs and the coloured region is the standard deviation.

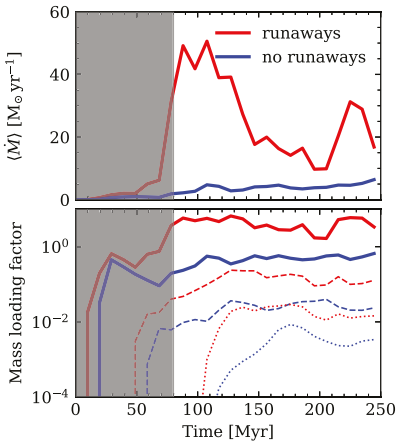

Figure 5. *Top*: Vertical gas outflow rate as function of time for the two models, measured in cylinders of radius 12 kpc and thickness 2 kpc, centred on ±5 kpc from the mid-plane. The grey region is neglected, since the simulation is still adjusting to the initial conditions during this time. When measuring $\langle \dot{M} \rangle$ at different heights we see a similar time profile but re-scaled, i.e. both lines are shifted down by the same amount when measuring at larger height. The `runaways` simulation features epochs of very strong outflows due to the production of large bubbles, which keeps growing due to injection of supernovae energy by runaway stars. *Bottom:* Mass loading factor as function of time for the two models, computed by dividing the outflow rate with the SFR, which quantifies the efficiency of the stellar feedback in driving outflows. We show this for three different heights: 5 kpc with 2 kpc thickness, i.e. identical to top panel (thick lines); 50 kpc with 10 kpc thickness (thin dashed line); 100 kpc with 20 kpc thickness (think dotted line). The selected distances corresponds to roughly 0.025 R_{200}, 0.25 R_{200}, and 0.5 R_{200}.

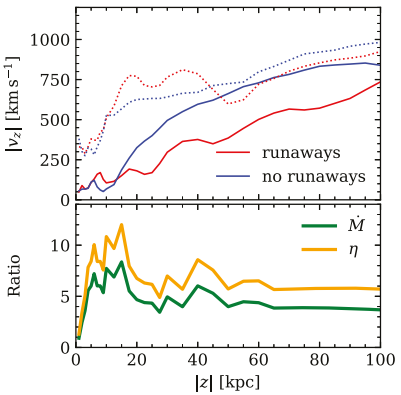

Figure 6. *Top*: Mean vertical velocity of the gas as function of vertical height, with warm gas ($2 \times 10^4 < T < 10^6$ K) as solid lines and hot gas ($10^6 < T < 10^8$ K) as dotted lines. *Bottom*: Ratio of outflow rates (green) and mass loading factor (orange) between the two simulations (`runaways` divided by `no runaways`) as function of vertical distance. To compute the outflow rates we used bin heights of 1 kpc for $|z| < 10$ kpc, 2.5 kpc for 10 kpc $< |z| < 30$ kpc, and 5 kpc for $|z| > 30$ kpc in order to account for the decreasing resolution with increased vertical height. The lines shows the mean of all simulation outputs ignoring the first 80 Myr.

at most four times more in the `runaways`, which is compatible with our mass measurements.

In both models, v_z increases with vertical distance, indicating that outflowing gas is accelerated by the continuously shock heated hot phase. Moreover, in contrast to `no runaways`, the `runaways` simulation features epochs of vigorous winds, with bursts of fast moving, hot ($T > 10^6$ K) gas originating from the large bubbles described earlier.

In the top panel of Fig. 6, we compare the mean outflow properties between the two models as function of vertical distance after 120 Myr. Regardless of vertical distance from the disc, the model accounting for runaway stars always features an increased mass-loss rate as well as mass loading factor. The impact of runaway stars on winds is hence not restricted to a narrowly defined region, but rather acts like an outflow strength 'multiplier' all the way up to ≈100 kpc. If generic, we note that this effect could allow for a simple treatment of the effect

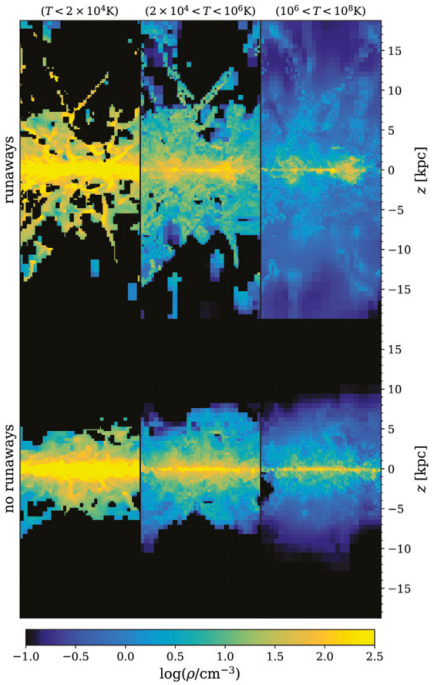

Figure 7. Projected density of gas in different temperature ranges (left-hand panel: molecular gas; middle panel: warm ionized gas; right-hand panel: hot gas) shown in panels with widths of 15 kpc in the edge-on view. In all three phases, the outflows caused by the inclusion runaway stars provide a significantly larger vertical scale. When comparing the time evolution of the two simulations in this view, we find repeated large bubbles (most clearly seen here in the hot gas) in the `runaways` simulation. These are absent in the `no runaways` simulation. The snapshot shown here is the last output (250 Myr).

of runaway stars in semi-analytical models of galaxy formation (see e.g. Somerville & Davé 2015) or cosmological simulations with phenomenological treatments of galactic winds (e.g. Vogelsberger et al. 2013).

4.3 Structure of gaseous halo

As already shown, runaway stars drive a strong galactic winds, launching large quantities of gas out in the halo. Despite the absence of cosmic inflows in our simulations and low resolution (∼100 pc) in the halo, the circumgalactic medium (CGM) produced by the outflows does play a crucial role in the long-term evolution of the galaxy, e.g. by determining the recycling of gas used for star formation. Unless otherwise stated, we focus now on gas within 40 kpc of the galaxy centre from which we remove the disc (±2 kpc vertically and 15 kpc radially).

Fig. 7 shows the projected density shown for three different temperature ranges. Runaway stars produce a CGM which is more extended with the presence of long gas filaments and small clouds. The clouds rise from the disc and dissipate on time-scales of tens of Myrs, in agreement with models of lifetimes of high velocity clouds around the Milky Way (Heitsch & Putman 2009). In our `runaways` simulation, the motion of the clouds varies with some clouds being accreted back on to the disc, some buoyantly floating above the plane and some lifted outwards until dissipation. The filaments are the result of ram pressure exerted on these clouds by the hot medium.

At $t = 250$ Myr, the gas mass in the considered halo region is 9.0×10^8 $M_\odot$ and 2.9×10^8 $M_\odot$ in the `runaways` and `no runaways` models, respectively. The excess mass in the `runaways` model is in very hot ($>10^6$ K), low density ($<10^{-2}$ cm^{-3}) gas, shown in the contours of Fig. 8 (as well as the histograms). The background colour of this plot gives the mass ratio between `runaways` and `no runaways` in different phases, where we see that the `runaways` model gives over one order of magnitude more gas mass in this phase, demonstrating the more efficient coupling of SNe energy to the halo.

In the density histogram of Fig. 8, we also see more mass for $\rho \approx 1$ cm^{-3} in the `runaways` model. This is gas with temperature $\sim 10^4$ K that sits in clouds and the filamentary structures. Finally, we note that in the `no runaways` simulation there is more diffuse ($\rho \sim 10^{-5}$ cm^{-3}) gas in the range $10^5 < T < 10^7$ K than in the `runaways` simulation.

5 DISCUSSION

5.1 Implications for long-term galactic evolution

We have demonstrated that simulations incorporating massive runaway stars feature galactic outflows with higher mass loading factors compared to models without. This leads to a more massive and structured galactic halo, and an overall reduction of the mass in the cold ISM.

The star-forming ISM is not only regulated more efficiently by galactic outflows, some fraction of the runaway stars travel far enough to deposit energy into the inter-arm regions and the inner galactic halo. This increases the thermal energy in diffuse gas, which in turn reduces the gas accretion rate of the galaxy and thus acts as a preventive feedback. Such a process is energetically more efficient than mechanically ejecting the same amount of gas from the ISM. This means that stellar feedback with runaway stars does not only lead to increased mass loading factors in galactic winds, but that it also includes a higher energy deposition into halo gas (Li & Bryan 2020).

Although our simulations have only been carried out for 250 Myr due to the high computational cost associated with treatment of individual stars, the above mechanisms imply a more efficient regulation of star formation over Gyr time-scales, and hence, an overall impact on galaxy evolution over a Hubble time. Applying our model in fully cosmological simulations, even for a limited amount of time, would be of great interest for shedding light on how runaway stars affect earlier phases of galaxy formation ($z > 1$) when gas accretion rates are significantly higher than at the current epoch and efficient stellar feedback is known to be important (e.g. Agertz & Kravtsov 2016). Runway star physics may therefore aid in explaining the inefficiency of galaxy formation from e.g. abundance matching (Behroozi et al. 2019), and will impact the precise galaxy mass range over which AGN feedback dominates stellar feedback (Benson et al. 2003).

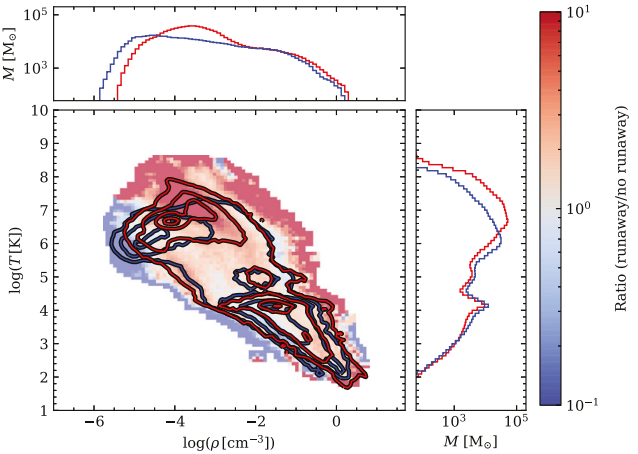

Figure 8. Comparison between the `runaways` (red) and `no runaways` (blue), as seen in the phase of the halo gas at the end of the simulation. The lines show the mass distribution in gas phase, where contours are given for 1 per cent, 10 per cent, 40 per cent, and 80 per cent and histograms show the sum of all values along a given axis value. The background map shows the ratio between the models, coloured such that red indicated excess in `runaways` and blue indicated excess in `no runaways`.

5.2 Comparison to other work

The literature on galaxy-scale simulations including runaway stars is limited due to the high computational cost of treating individual stars. Previous studies have therefore used alternative methods to overcome this challenge. Simulations of vertically stratified patches of discs have been used to compare clustered and random placement of SNe (see e.g. Korpi et al. 1999; de Avillez 2000; de Avillez & Breitschwerdt 2004, 2005; Joung & Mac Low 2006; Walch et al. 2015; Girichidis et al. 2016; Martizzi et al. 2016; Gatto et al. 2017). Early works studied SNe placement based on density thresholds (Korpi et al. 1999) and showed that some SN explosions must occur in isolation in order to produce a realistic multiphase ISM (see e.g. de Avillez 2000; de Avillez & Breitschwerdt 2004; Joung & Mac Low 2006; Walch et al. 2015; Li, Bryan & Ostriker 2017). In agreement with our results, these authors have found an increased effect from stellar feedback as a result of randomly placed SNe. In fact, models with stellar feedback injected over a broad range of densities leads to a very turbulent ISM and an overall reduction of star formation. Additionally, Kim & Ostriker (2018) found an increased mass loading factor as a result of including runaway stars, especially for hot gas, although this depends quantitatively on the vertical structure of the disc (Li et al. 2017).

The volume filling factor of gas with different temperatures has, not surprisingly, been shown to be affected by randomly placed SNe (see e.g. de Avillez & Breitschwerdt 2004; Walch et al. 2015). This is also the case in our work, with more of the volume filled by hot gas ($T > 3 \times 10^5$ K) in the disc when including runaway stars (71 per cent versus 54 per cent). We find that the opposite is true for the halo, where the dense clouds expelled by the strong winds somewhat reduce the volume filling factor in hot gas.

For our model, we account for the entire galactic disc, although this imposes constraints on the spatial resolution we can afford. As was pointed out by Martizzi et al. (2016), not accounting for the global geometry of the disc, as is the case for ISM patches, leads to unreliable wind properties due to incorrect treatment of the gravitational potential and the disc rotation.

To our knowledge, no other simulation works of entire disc galaxies have included treatment of individual runaway stars, although alternative methods have been studied. A model by Ceverino & Klypin (2009), also used in simulations by Ceverino et al. (2014) and Zolotov et al. (2015), includes the effect of runaway stars by applying velocity kicks to 10–30 per cent of all stellar particles (with masses $>10^4$ M$_\odot$), representing entire stellar populations rather than individual massive stars. Ceverino et al. (2014) showed that their model depend strongly on resolution with its effect disappearing at low-resolution (60 pc) compared to high-resolution (14 pc) simulations. This is not unexpected since the mean travel distance of OB runaway stars is of the order of 100 pc (see Section 2.2) that sets a characteristic scale that needs to be resolved for these stars to differ from massive stars remaining in their natal regions.

In order to alleviate the computational expense required by tracing the trajectory of individual stars, an intermediate step could be to distribute SNe explosions around their natal stellar population. Tress et al. (2020) used this approach by injecting SNe energy at locations randomly sampled from a 5 pc Gaussian distribution. Although this captures some aspects like the spatial extent of star clusters, this is not representative of runaway stars that can travel significantly further and yield more complex distance distributions.

5.3 Comparisons to observations

Observational evidence for strong galactic winds is today ubiquitous e.g. in starburst galaxies (Veilleux, Cecil & Bland-Hawthorn 2005; Rupke 2018). In this section, we discuss how our simulations compare with the current observational data. We note that this comparison

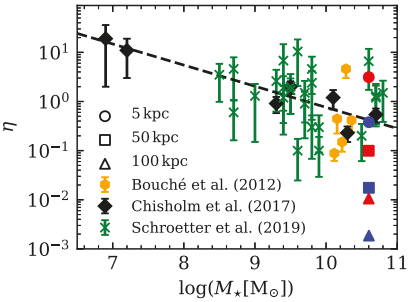

Figure 9. Mass loading factor as function of stellar mass comparing the results of our simulations to values observed. Our simulations, with `runaways` in red and `no runaways` in blue, are shown measured at three different vertical heights (see Fig. 5 for details). Orange markers show data for galaxies at redshift ∼0.1 from Bouché et al. (2012). Black diamonds show data from nearby star-forming galaxies from Chisholm et al. (2017) with mass loading estimates computed from maximum outflow rates divided by star formation rates derived from UV spectra. The scaling relation derived in their work is shown as the dashed black line. The green crosses show measurements from galaxies at redshift ∼0.1 by Schroetter et al. (2019). Although η depends strongly on the where outflows are measured the ratio between the two simulations remain the same.

should be treated with caution since our simulations are idealized, isolated disc galaxies without their cosmological environment.

Mass loading factors in external galaxies have been observed to depend on galaxy mass, although there is a considerable spread with mass loading factors ranging between $\eta \sim 0.01$–10, even at a fixed stellar mass (Martin 1999; Bouché et al. 2012; Chisholm et al. 2017; Schroetter et al. 2019). Mass loading factors are difficult to extract from observations due the incomplete census of various gas phases as well as their sensitivity to where in the galaxy one measures them. Since observations typically use quasars absorption spectra to study winds in external galaxies the random positioning of the quasar with respect to star-forming galaxies makes this a challenging endeavour. In Fig. 9, we show a composite of observationally derived mass loading factors as function of stellar mass including a fit from Chisholm et al. (2017) together with our results. The data indicate a negative trend with stellar mass, as well as a large scatter. We show the final values of our results at three different heights above the disc plane. These values are in broad agreement with the entire spread in the observations, with the exception of the outermost measurements of the `no runaways` simulation. This implies that the spread in our simulations is due to either height above the disc plane or the different stellar physics we consider, i.e. runaway stars. In the absence of information on the height of measurements (due to uncertain inclination of the disc), it is not possible to disentangle these two possibilities.

Other simulation work have modelled self-consistent driving of galactic outflows from stellar feedback in massive galaxies. Notably, Muratov et al. (2015) analysed the FIRE simulation suite and found that for $M_\star \gtrsim 10^{10}$ M$_\odot$, mass loading factors were consistent with $\eta \sim 0$ when measured at $0.25R_{\rm vir} \approx 50$ kpc (see their Fig. 6). This is incompatible with the observations compiled in Fig. 9, and illustrates that the role of stellar feedback-driven winds in galaxies of this mass is not yet understood. The results of Muratov et al. may indicate a lack of additional physics such as runaway stars as our `no runaways` simulation also produce low, albeit non-zero, mass loading factors.

Another striking effect of the runaway stars is the more structured and extended gas halo. The CGM is indeed observed to be highly structured (e.g. Werk et al. 2014, and references therein), with stellar feedback leaving a specific imprint on the properties of the circumgalactic gaseous haloes (e.g. Liang, Kravtsov & Agertz 2016). To date, no consensus exists on what is driving the fine scale structure of the CGM, partly due to the fact that galaxy scale simulations are far from resolving the (likely) parsec scale clouds that make up the halo on small scales (see discussion in Section 5.5). We leave a study of the impact of run-away stars on halo absorber column density profiles and covering fractions for a future study.

In Section 4.3, we noted that more halo gas clouds existed across a wide range of temperatures in the `runaways` simulation. They arise from gas lifted from the disc as well as halo gas compression from self-gravity followed by efficient cooling [indeed, cooling is most efficient at $T \sim$ few $\times\ 10^5$ K, with feedback driven perturbations leading to thermal instabilities Joung, Bryan & Putman (2012) and cloud formation]. In reality, these clouds may be destroyed via hydrodynamical instabilities, as they fall back on to the disc (Heitsch & Putman 2009), a process that is likely not fully captured in our models. Regardless, these clouds could be interpreted as high velocity clouds (HVCs), which are observed in the Milky Way halo (Blitz et al. 1999; Wakker 2004; Moss et al. 2013; Moss, Lockman & McClure-Griffiths 2017). The origin of the HVCs is still an open question (Lockman et al. 2019), and although the most distant ones are likely from cosmic origin (see e.g. Richter 2012), there are plenty of clouds observed within few tens of kpc (see Wakker et al. 2008), compatible with our `runaways` model. It is likely that at least some fraction of these clouds originate from outflows (Quilis & Moore 2001), making the more efficient coupling of feedback energy to the galactic halo allowed by runaway stars an interesting addition to the formation scenario of HVCs.

Finally, we briefly highlight a curious effect found when including runaway stars in our simulations, namely their effect on the resolved Kennicutt–Schmidt (KS) relation. This relation is shown for the final output of both the `runaways` and `no runaways` simulations in Fig. 10, together with the relation from Daddi et al. (2010; see also Kennicutt 1998). With `runaways` we find regions of the disc that reside significantly below the canonical value, reaching $\Sigma_{\rm SFR} \sim 10^{-6}$ M$_\odot$ yr^{-1} kpc^{-2}. Since our model has a finite-mass resolution for star formation events (∼500 M$_\odot$), a lower limit to star formation surface densities of $\Sigma_{\rm SFR} \approx 10^{-4}$ M$_\odot$ yr^{-1} kpc^{-2}, for the accounted time (2 Myr) and area (1 kpc^2), is expected. This is indeed the case for `no runaways`, since stars does not significantly change in mass over 2 Myr. In contrast, in the `runaways` model, this is enough for a fraction of runaway stars to venture away from their natal region and masquerade as inefficient star formation events. This is highlighted by the deviation in mean peculiar velocity of the stars shown by colour in Fig. 10. Runaway star may therefore provide an explanation for the extremely inefficient star formation observed in local spiral and dwarf galaxies (Bigiel et al. 2010) which we will focus on in forthcoming work (Andersson et al. in preparation).

5.4 The impact of runaway stars in dwarf galaxies

Dwarf galaxies have shallow potential wells and are expected to be strongly affected by stellar feedback, with higher mass loading factors than the cases studied here (see Fig. 9) resulting in low galaxy formation efficiencies (Behroozi et al. 2019).

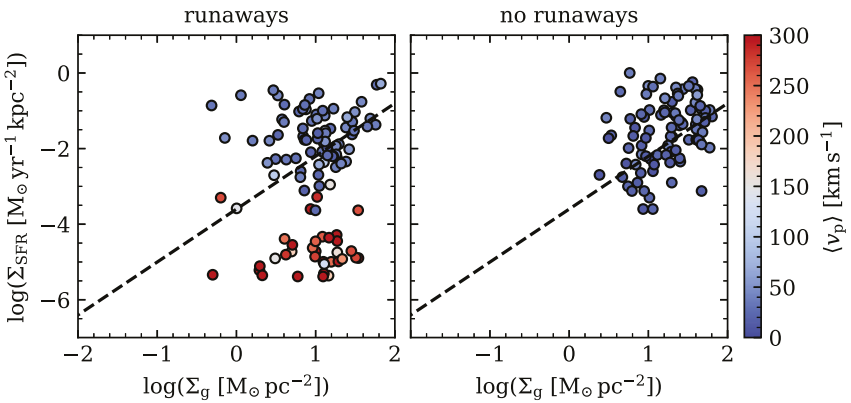

Figure 10. Resolved Kennicutt–Schmidt relation, $\Sigma_{\rm SFR}$ versus $\Sigma_{\rm g}$, comparing the runaway model (left) to the model ignoring runaway stars (right). Each point is a measurement from a 1 kpc square in the 24 kpc wide face-on view of the galaxy using data from our last output. To compute the star formation rate, we use an age bin of 2 Myr. The colours show the mean velocity of all these stars, calculated after removing the velocity component coming from the rotational velocity. The grey dashed line shows the empirical relation fitted by Daddi et al. (2010) for disc galaxies. The `runaways` simulation includes a group of points with star formation rates $\sim 10^{-5}$ M$_\odot$ yr^{-1} kpc^{-2} that corresponds to runaway stars, as is indicated by the high velocity of the stars in these points.

To give us an indication of how runaway stars impact these low-mass galaxies we set up two additional pairs of simulations. The first consists of a galaxy formed from collapsing gas in an analytical description of a dark matter halo. Its potential is set up according to a Navarro–Frenk–White (NFW) profile (Navarro, Frenk & White 1997) with $R_{200} = 50$ kpc, where the rotational velocity is 35 km s^{-1}. This set-up is identical to that of Teyssier et al. (2013), except they used a 'live' halo described by particles. We adopt the same star formation and feedback recipes as is described in Section 2 and compared the evolution of one with and one without our runaway star model. After a settling phase the star formation and outflow rates were almost identical regardless of whether runaway stars are included or not. In addition to the isolated dwarf galaxy, we simulated the formation of a ultra-faint dwarf (UFD) galaxy ($M_{200} = 10^9$ M$_\odot$ at $z = 0$) in cosmological setting. The set-up used is the same as the fiducial simulation in Agertz et al. (2020), except that we include our star formation and feedback models. Akin to the isolated dwarf galaxy we find a surprisingly small effect when including runaway stars, despite the mean travel distance for SNe progenitors being on the order of the half mass radius (∼300 pc) of the simulated UFD.

We attribute the lack of impact of runaways on dwarf galaxies, at least in terms of outflow properties, to the high porosity of the ISM which arises due to the shallow potential. This implies that energy from any SN is likely to efficiently couple to diffuse gas within or outside galaxy, regardless of the inclusion of runaways. None the less, since runaway stars can leave the galaxy entirely one may expect a different enrichment history for the CGM. How this affects the chemistry of the dwarf galaxy and its environment in the long term deserves a dedicated study.

5.5 Limitations of the model

Throughout this work we have outlined limitations to our model. In this section, we summarize these points and discuss possible improvements for the future. We highlight that this work is an exploratory study with the aim of giving a first approximation as to how runaway stars affect the physical processes in full galaxy simulations.

Treating self-consistently the star–star interactions responsible for the velocity kicks is still not possible in galactic context. This is due to the extreme computational cost a star-by-star description would represent, and also because of the need of a direct collisional treatment of gravity, to resolve close encounters and binary evolution, which is not possible with galaxy simulation codes. Therefore, we must rely on sub-grid models to assign the kick velocities, and ignore possible variation with the environment. None the less, future work should focus on how the results here depend on the velocity distribution, which in turn can be studied outside the galacic context (see e.g. Eldridge et al. 2011; Perets & Šubr 2012; Moyano Loyola & Hurley 2013; Oh & Kroupa 2016; Renzo et al. 2019). Furthermore, the results shown here assumes a runaway fraction of 14 per cent which is applied to all massive stars. Although this agrees with runaway fraction for O stars in a $10^{3.5}$ M$_\odot$ cluster (Oh & Kroupa 2016), it is not universal and observational data indicate that this fraction can be significantly lower with variations with stellar type. Maíz Apellániz et al. (2018) estimated the fraction at 10–12 per cent for the O stars and ∼ 6 per cent for B stars, which is also in agreement with those from Eldridge et al. (2011) when correcting for completeness. The results shown here could therefore overestimate the impact of runaway stars. Future work should focus on how the results depend on changing their runaway parameters.

The resolution of our simulations is limited to 9 pc. This allows us to resolve the typical size of the massive star-forming gas clouds with approximately ten resolution elements, and this is essentially the scale runaway stars need to travel to reach low densities. Since this contrast in density is key to how the runaway stars affect the galactic evolution, an increase in resolution that allows for higher density contrast may also increasing the effect of runaway stars – in essence, less travel distance is required for more of the stars to reach low density gas to explode in. A suite of galaxy simulations

with incrementally higher spatial resolution would be required to understand whether convergence can be reached.

Finally, we note that due to the adopted adaptive refinement scheme the cooling length of the halo remains unresolved and we can only demonstrate systematic effects of the strong galactic wind caused by runaway stars. For a detailed discussion as to what this entails we refer to McCourt et al. (2018), Hummels et al. (2019), and van de Voort et al. (2019).

6 CONCLUSIONS

Using hydrodynamical simulations of Milky Way-like galaxies, we have investigated how their evolution is affected by the inclusion of runaway stars, a mechanism not commonly accounted for in galaxy simulations. Our model initializes massive stars as individual particles with velocity kicks randomly sampled from a typical distribution for natal star clusters. For our star-by-star treatment, we have implemented a new model for stellar feedback accounting for fast stellar winds and core-collapse SN. We compare the impact of this implementation to one with similar feedback physics but without any velocity kicks, thus ignoring runaway stars. In summary, we find the following differences when including runaway stars:

(i) A significant fraction of SNe explode in low-density gas ($\rho < 10^{-3}$ cm^{-3}), with more than a doubling of SN explosions at densities 10^{-4} cm^{-3}. By placing SN progenitors in hot bubbles, where star formation is otherwise inhibited, the runaway mechanism significantly heats the inter-arm regions and drives strong galactic winds. This yields mass loading factors $\eta \sim 5$ when measured at the disc–halo interface – an order of magnitude increase compared to models neglecting runaways. Both our models are compatible with observational values of η, which have large scatter due to uncertainty in where in the galaxy it is measured. Therefore, measurements of η with accurate estimates of location are required to fully understand the importance of accounting for runaway stars.

(ii) In the halo, we find three times more gas mass, primarily in the hot diffuse phase, as well as a population of dense clouds that dissipate on time-scales of tens of Myrs. This is mainly due to the large amount of gas lifted out by outflows. Furthermore, runaway stars are able to travel far enough to directly deposit SN energy into the halo, efficiently heating the CGM and preventing re-accretion of gas on to the disc.

(iii) The cold ISM ($T < 10^4$ K) is less disturbed by stellar feedback since runaways can leave the star formation regions. This implies that, although runaway stars lead to increased feedback efficiency, there is little change to the overall structure of cold ISM. Therefore, the effect of runaway stars cannot be simply modelled by increasing stellar feedback, but an actual relocation of the feedback sources must be implemented.

One limitation of our model is the assumption of a universal velocity distribution for stellar birth environments. Contrary to this, properties such as cluster density, binary fraction, and IMF variations ought to play a role. Models accounting for stellar-scale properties (e.g. binary stars) in cosmological models exist (see e.g. Rosdahl et al. 2018), although without treatment for runaway stars, which requires tracing individual trajectories. A complete understanding of how runaways affect galaxy evolution might require a combination of these kind of models. However, treating even just a fraction of the stars as individual particles is very numerically expensive; therefore, studying how our results depend on this velocity distribution is left to future work. Another limitation is that our model for stellar feedback ignores radiative processes. The strong luminosity of OB stars heats the surrounding medium before they explode as SN, thus affects how the energy is transferred to the gas. Adding radiative transfer to our already computationally heavy method is however beyond the scope of disc galaxy simulations. This would however be feasible for less massive galaxies, however, we do not see any significant effect of runaway stars for these galaxies. We attribute this to the high porosity of small galaxies implying that SNe location plays a minor role. As a final remark, the effect of runaway stars is clear in spiral galaxies for which the strong outflows lead to a more efficient regulation of star formation and in the long term this might impact the high end of the luminosity function.

ACKNOWLEDGEMENTS

We thank Romain Teyssier for insightful discussions that improved our work. We thank the referee for helpful and constructive comments which greatly improved this work. The analysis of this work has made use of `yt` (Turk et al. 2011), `pynbody` (Pontzen et al. 2013), MATPLOTLIB (Hunter 2007), and NUMPY (Virtanen et al. 2020). We acknowledge support from the Knut and Alice Wallenberg Foundation. OA acknowledges support from the Swedish Research Council (grant no. 2014-5791). The simulations were performed on resources provided by the Swedish National Infrastructure for Computing (SNIC) at Lunarc. EA acknowledges financial support from the Royal Physiographic Society in Lund.

REFERENCES

Agertz O., et al., 2020 , MNRAS , 491, 1656
Agertz O., Kravtsov A. V., 2015, ApJ, 804, 18
Agertz O., Kravtsov A. V., 2016, ApJ, 824, 79
Agertz O., Teyssier R., Moore B., 2011, MNRAS, 410, 1391
Agertz O., Kravtsov A. V., Leitner S. N., Gnedin N. Y., 2013, ApJ, 770, 25
Agertz O., Romeo A. B., Grisdale K., 2015, MNRAS, 449, 2156
Asplund M., Grevesse N., Sauval A. J., Scott P., 2009, ARA&A, 47, 481
Banerjee S., Kroupa P., Oh S., 2012, ApJ, 746, 15
Behroozi P., Wechsler R. H., Hearin A. P., Conroy C., 2019, MNRAS, 488, 3143
Benson A. J., Bower R. G., Frenk C. S., Lacey C. G., Baugh C. M., Cole S., 2003, ApJ, 599, 38
Bigiel F., Leroy A., Walter F., Blitz L., Brinks E., de Blok W. J. G., Madore B., 2010, AJ, 140, 1194
Blaauw A., 1961, Bull. Astron. Inst. Neth., 15, 265
Blitz L., Spergel D. N., Teuben P. J., Hartmann D., Burton W. B., 1999, ApJ, 514, 818
Bouché N., Hohensee W., Vargas R., Kacprzak G. G., Martin C. L., Cooke J., Churchill C. W., 2012, MNRAS, 426, 801
Cassinelli J. P., Lamers H. J. G. L. M., 1987, in Kondo Y., Wamsteker W., eds, Astrophysics and Space Science Library Vol. 129, Exploring the Universe with the IUE Satellite, Springer, Dordrecht. p. 139
Ceverino D., Klypin A., 2009, ApJ, 695, 292
Ceverino D., Klypin A., Klimek E. S., Trujillo-Gomez S., Churchill C. W., Primack J., Dekel A., 2014, MNRAS, 442, 1545
Chisholm J., Tremonti C. A., Leitherer C., Chen Y., 2017, MNRAS, 469, 4831
Daddi E. et al., 2010, ApJ, 714, L118
Dale J. E., Bonnell I. A., 2008, MNRAS, 391, 2
de Avillez M. A., 2000, MNRAS, 315, 479
de Avillez M. A., Breitschwerdt D., 2004, A&A, 425, 899
de Avillez M. A., Breitschwerdt D., 2005, A&A, 436, 585
Dekel A., Silk J., 1986, ApJ, 303, 39
Eisenstein D. J. et al., 2005, ApJ, 633, 560
Eldridge J. J., Langer N., Tout C. A., 2011, MNRAS, 414, 3501
Emerick A., Bryan G. L., Mac Low M.-M., 2019, MNRAS, 482, 1304
Gatto A. et al., 2017, MNRAS, 466, 1903

Gies D. R., 1987, ApJS, 64, 545
Gies D. R., Bolton C. T., 1986, ApJS, 61, 419
Girichidis P. et al., 2016, MNRAS, 456, 3432
Grisdale K., Agertz O., Romeo A. B., Renaud F., Read J. I., 2017, MNRAS, 466, 1093
Grisdale K., Agertz O., Renaud F., Romeo A. B., 2018, MNRAS, 479, 3167
Grisdale K., Agertz O., Renaud F., Romeo A. B., Devriendt J., Slyz A., 2019, MNRAS, 489, 5482
Guillet T., Teyssier R., 2011, J. Comput. Phys., 230, 4756
Heitsch F., Putman M. E., 2009, ApJ, 698, 1485
Hernquist L., 1990, ApJ, 356, 359
Hernquist L., 1993, ApJS, 86, 389
Heyer M., Krawczyk C., Duval J., Jackson J. M., 2009, ApJ, 699, 1092
Hockney R. W., Eastwood J. W., 1981, Computer Simulation Using Particles, McGraw-Hill, New York
Hoogerwerf R., de Bruijne J. H. J., de Zeeuw P. T., 2000, ApJ, 544, L133
Hoogerwerf R., de Bruijne J. H. J., de Zeeuw P. T., 2001, A&A, 365, 49
Hopkins P. F. et al., 2018, MNRAS, 480, 800
Hopkins P. F., Kereš D., Oñorbe J., Faucher-Giguère C.-A., Quataert E., Murray N., Bullock J. S., 2014, MNRAS, 445, 581
Hu C.-Y., Naab T., Glover S. C. O., Walch S., Clark P. C., 2017, MNRAS, 471, 2151
Hummels C. B. et al., 2019, ApJ, 882, 156
Hunter J. D., 2007, Comput. Sci. Eng., 9, 90
Hurley J. R., Pols O. R., Tout C. A., 2000, MNRAS, 315, 543
Iffrig O., Hennebelle P., 2015, A&A, 576, A95
Jilinski E., Ortega V. G., Drake N. A., de la Reza R., 2010, ApJ, 721, 469
Joung M. K. R., Mac Low M.-M., 2006, ApJ, 653, 1266
Joung M. R., Bryan G. L., Putman M. E., 2012, ApJ, 745, 148
Katz N., 1992, ApJ, 391, 502
Keller B. W., Wadsley J., Benincasa S. M., Couchman H. M. P., 2014, MNRAS, 442, 3013
Kennicutt R. C.,, Jr, 1998, ARA&A, 36, 189
Kim J.-h. et al., 2014, ApJS, 210, 14
Kim J.-h. et al., 2016, ApJ, 833, 202
Kim C.-G., Ostriker E. C., 2015, ApJ, 802, 99
Kim C.-G., Ostriker E. C., 2018, ApJ, 853, 173
Klypin A. A., Shandarin S. F., 1983, MNRAS, 204, 891
Klypin A. A., Trujillo-Gomez S., Primack J., 2011, ApJ, 740, 102
Komatsu E. et al., 2011, ApJS, 192, 18
Korpi M. J., Brandenburg A., Shukurov A., Tuominen I., Nordlund, Å., 1999, ApJ, 514, L99
Kroupa P., 2001, MNRAS, 322, 231
Krumholz M. R., Tan J. C., 2007, ApJ, 654, 304
Kudritzki R. P., Pauldrach A., Puls J., 1987, A&A, 173, 293
Lahén N., Naab T., Johansson P. H., Elmegreen B., Hu C.-Y., Walch S., 2019, ApJ, 879, L18
Lamers H. J. G. L. M., Cassinelli J. P., 1999, Introduction to Stellar Winds, Cambridge Univ. Press, Cambridge, UK
Lee E. J., Miville-Deschênes M.-A., Murray N. W., 2016, ApJ, 833, 229
Leitherer C., Robert C., Drissen L., 1992, ApJ, 401, 596
Li M., Bryan G. L., 2020 , ApJ, 890, L30
Li M., Bryan G. L., Ostriker J. P., 2017, ApJ, 841, 101
Liang C. J., Kravtsov A. V., Agertz O., 2016, MNRAS, 458, 1164
Lockman F., Betti S. K., Hill A. S., Lehner N., Shelton R. L., Wakker B. P., 2019, BAAS, 51, 255
Maíz Apellániz J., Pantaleoni González M., Barbá R. H., Simón-Díaz S., Negueruela I., Lennon D. J., Sota A., Trigueros Páez E., 2018, A&A, 616, A149
Martin C. L., 1999, ApJ, 513, 156
Martizzi D., Faucher-Giguère C.-A., Quataert E., 2015, MNRAS, 450, 504
Martizzi D., Fielding D., Faucher-Giguère C.-A., Quataert E., 2016, MNRAS, 459, 2311
McCourt M., Oh S. P., O'Leary R., Madigan A.-M., 2018, MNRAS, 473, 5407
Mokiem M. R. et al., 2007, A&A, 473, 603
Moss V. A., McClure-Griffiths N. M., Murphy T., Pisano D. J., Kummerfeld J. K., Curran J. R., 2013, ApJS, 209, 12
Moss V. A., Lockman F. J., McClure-Griffiths N. M., 2017, ApJ, 834, 155
Moyano Loyola G. R. I., Hurley J. R., 2013, MNRAS, 434, 2509
Muratov A. L., Kereš D., Faucher-Giguère C.-A., Hopkins P. F., Quataert E., Murray N., 2015, MNRAS, 454, 2691
Murray N., 2011, ApJ, 729, 133
Naab T., Ostriker J. P., 2017, ARA&A, 55, 59
Navarro J. F., Frenk C. S., White S. D. M., 1997, ApJ, 490, 493
Oh S., Kroupa P., 2016, A&A, 590, A107
Ohlin L., Renaud F., Agertz O., 2019, MNRAS, 485, 3887
Perets H. B., Šubr L., 2012, ApJ, 751, 133
Pontzen A., Roškar R., Stinson G. S., Woods R., Reed D. M., Coles J., Quinn T. R., 2013, pynbody: Astrophysics Simulation Analysis for Python, Astrophysics Source Code Library, ascl:1305.002
Poveda A., Ruiz J., Allen C., 1967, Boletin de los Observatorios Tonantzintla y Tacubaya, 4, 86
Quilis V., Moore B., 2001, ApJ, 555, L95
Raiteri C. M., Villata M., Navarro J. F., 1996, A&A, 315, 105
Reid B. A. et al., 2010, MNRAS, 404, 60
Renaud F. et al., 2013, MNRAS, 436, 1836
Renzo M. et al., 2019, A&A, 624, A66
Rhodin N. H. P., Agertz O., Christensen L., Renaud F., Fynbo J. P. U., 2019, MNRAS, 488, 3634
Richter P., 2012, ApJ, 750, 165
Romeo A. B., Agertz O., Moore B., Stadel J., 2008, ApJ, 686, 1
Rosdahl J. et al., 2018, MNRAS, 479, 994
Rosdahl J., Schaye J., Dubois Y., Kimm T., Teyssier R., 2017, MNRAS, 466, 11
Rosen A., Bregman J. N., 1995, ApJ, 440, 634
Roškar R., Teyssier R., Agertz O., Wetzstein M., Moore B., 2014, MNRAS, 444, 2837
Rupke D., 2018, Galaxies, 6, 138
Schilbach E., Röser S., 2008, A&A, 489, 105
Schroetter I. et al., 2019, MNRAS, 490, 4368
Silva M. D. V., Napiwotzki R., 2011, MNRAS, 411, 2596
Simpson C. M., Bryan G. L., Hummels C., Ostriker J. P., 2015, ApJ, 809, 69
Somerville R. S., Davé R., 2015, ARA&A, 53, 51
Sormani M. C., Treß R. G., Klessen R. S., Glover S. C. O., 2017, MNRAS, 466, 407

Springel V. et al., 2005, Nature, 435, 629
Springel V., 2000, MNRAS, 312, 859
Stinson G., Seth A., Katz N., Wadsley J., Governato F., Quinn T., 2006, MNRAS, 373, 1074
Stone R. C., 1991, AJ, 102, 333
Su K.-Y. et al., 2018, MNRAS, 480, 1666
Sutherland R. S., Dopita M. A., 1993, ApJS, 88, 253
Tamburro D., Rix H. W., Leroy A. K., Mac Low M. M., Walter F., Kennicutt R. C., Brinks E., de Blok W. J. G., 2009, AJ, 137, 4424
Teyssier R., 2002, A&A, 385, 337
Teyssier R., Pontzen A., Dubois Y., Read J. I., 2013, MNRAS, 429, 3068
Tress R. G., Smith R. J., Sormani M. C., Glover S. C. O., Klessen R. S., Mac Low M.-M., Clark P. C., 2020, MNRAS, 492, 2973
Turk M. J., Smith B. D., Oishi J. S., Skory S., Skillman S. W., Abel T., Norman M. L., 2011, ApJS, 192, 9
van de Voort F., Springel V., Mandelker N., van den Bosch F. C., Pakmor R., 2019, MNRAS, 482, L85
Veilleux S., Cecil G., Bland-Hawthorn J., 2005, ARA&A, 43, 769
Viel M., Becker G. D., Bolton J. S., Haehnelt M. G., Rauch M., Sargent W. L. W., 2008, Phys. Rev. Lett., 100, 041304
Vink J. S., 2011, Ap&SS, 336, 163
Vink J. S., de Koter A., Lamers H. J. G. L. M., 2001, A&A, 369, 574
Virtanen P. et al., 2020 Nature Methods, 17, 261
Vogelsberger M., Genel S., Sijacki D., Torrey P., Springel V., Hernquist L., 2013, MNRAS, 436, 3031
Wakker B. P. et al., 2008, ApJ, 672, 298
Wakker B. P., 2004, in Duc P.-A., Braine J., Brinks E., eds, Proc. IAU Symp. 217, Recycling Intergalactic and Interstellar Matter, Astronomical Society of the Pacific, San Francisco. p. 2
Walch S. et al., 2015, MNRAS, 454, 238
Walch S., Naab T., 2015, MNRAS, 451, 2757
Werk J. K. et al., 2014, ApJ, 792, 8
Wheeler C. et al., 2019 , MNRAS, 490, 4447
Willis A. J., Garmany C. D., 1987, in Kondo Y., Wamsteker W., eds, Astrophysics and Space Science Library Vol. 129, Exploring the Universe with the IUE Satellite, Springer, Dordrecht. p. 157
Zolotov A. et al., 2015, MNRAS, 450, 2327

This paper has been typeset from a TEX/LATEX file prepared by the author.

Paper II

Monthly Notices of the ROYAL ASTRONOMICAL SOCIETY
MNRAS **502,** L29–L34 (2021) doi:10.1093/mnrasl/slaa201

Runaway stars masquerading as star formation in galactic outskirts

Eric P. Andersson ,★ Florent Renaud and Oscar Agertz
Department of Astronomy and Theoretical Physics, Lund Observatory, Box 43, SE-221 00 Lund, Sweden

Accepted 2020 December 10. Received 2020 December 7; in original form 2020 October 22

ABSTRACT

In the outskirts of nearby spiral galaxies, star formation is observed in extremely low gas surface densities. Star formation in these regions, where the interstellar medium is dominated by diffuse atomic hydrogen, is difficult to explain with classic star formation theories. In this letter, we introduce runaway stars as an explanation for this observation. Runaway stars, produced by collisional dynamics in young stellar clusters, can travel kiloparsecs during their main-sequence lifetime. Using galactic-scale hydrodynamic simulations including a treatment of individual stars, we demonstrate that this mechanism enables the ejection of young massive stars into environments where the gas is not dense enough to trigger star formation. This results in the appearance of star formation in regions where it ought to be impossible. We conclude that runaway stars are a contributing, if not dominant, factor to the observations of star formation in the outskirts of spiral galaxies.

Key words: stars: kinematics and dynamics – ISM: evolution – galaxies: star formation.

1 INTRODUCTION

Schmidt (1959) suggested that the relationship between the star formation rate (SFR) density $\Sigma_{\rm SFR}$ and gas surface density $\Sigma_{\rm g}$, commonly referred to as the star formation (SF) relation, follows a power law. The canonical SF relation is typically quoted with a slope of 1.4 with a break appearing at a critical threshold (e.g. Kennicutt 1989, 1998; Kennicutt & Evans 2012). The break occurs at $\sim$10 $M_\odot$ pc^{-2} and is attributed to the transition between molecular hydrogen H_2 and neutral atomic hydrogen H I (Wong & Blitz 2002; Kennicutt et al. 2007; Bigiel et al. 2008; Bolatto et al. 2011). However, the underlying reasons of the transition are debated; for a review, see, for example, Schaye (2004), Krumholz & McKee (2005), Krumholz, McKee & Tumlinson (2009), Renaud, Kraljic & Bournaud (2012), Federrath (2013) or Krumholz (2014).

In the outskirts of spiral galaxies and dwarf irregular galaxies, the SF relation extends into extremely diffuse gas going from $\Sigma_{\rm g} \sim 10\ M_\odot\ {\rm yr}^{-1}$ towards $\Sigma_{\rm g} \sim 1\ M_\odot\ {\rm yr}^{-1}$ (Roychowdhury et al. 2009; Bigiel et al. 2010; Bolatto et al. 2011; Elmegreen & Hunter 2015) in which SF proceeds extremely slowly with a roughly constant depletion time of 100 Gyr. Elmegreen (2015, 2018) found an SF relation with a slope of 2 for the outer galaxy if the disc flares (i.e. if the thickness is regulated by gas self-gravity and a radially uniform velocity dispersion). Krumholz (2013) suggested another model, in which SF can occur in an atomic medium with separate cold and warm phases. Krumholz argued that in regions with low SFR (e.g. galactic outskirts), the transition between H I and cold star-forming H_2 is mediated by hydrostatic balance. SF then proceeds slowly, with depletion times of $\sim$100 Gyr, in agreement with observations (e.g. Bigiel et al. 2010; Bolatto et al. 2011). Here we show that runaway stars, formed in dense gas and ejected into low-density regions, naturally explain the observed third regime of SF in galactic outskirts.

Runaway stars are produced by close encounters and binary disruption as a result of stellar evolution in young stellar clusters (Blaauw 1961; Poveda, Ruiz & Allen 1967). These stars have been studied extensively, both observationally (e.g. Gies & Bolton 1986; Gies 1987; Stone 1991; Hoogerwerf, de Bruijne & de Zeeuw 2000; Silva & Napiwotzki 2011; Maíz Apellániz et al. 2018; Dorigo Jones et al. 2020; Raddi et al. 2020) and through modelling (e.g. Ceverino & Klypin 2009; Eldridge, Langer & Tout 2011; Moyano Loyola & Hurley 2013; Oh & Kroupa 2016; Kim & Ostriker 2018; Andersson, Agertz & Renaud 2020). Typically, 5–10 per cent of massive OB-type stars have velocities exceeding 30 km s^{-1} and can travel hundreds of pc to several kpc before exploding as core-collapse supernovae (SNe). Moreover, the less massive B stars ($\sim$4 $M_\odot$) are more numerous and can travel significantly further because of their longer lifetimes ($\sim$150 Myr). As such, they can reach the galactic outskirts and contribute to the observational tracers of the SF activity, yet without direct physical connection to the formation sites. By expanding on the results of Andersson et al. (2020), we show in this letter that this mechanism yields an observable signature in striking agreement with SF in galactic outskirts, where gas surface densities are extremely low, as observed by Bigiel et al. (2010).

2 NUMERICAL SET-UP

We use the two isolated Milky Way-like galaxies described in Andersson et al. (2020). We compare one (a simulation referred to as `runaways`), which includes runaway stars where individual stars are tracked both in terms of stellar evolution and kinematically, with an identical simulation ignoring runaway stars (referred to as `no runaways`). We briefly describe the numerical method here, and refer to Andersson et al. (2020) for details.

We ran the two simulations for 250 Myr using the *N*-body + Adaptive Mesh Refinement (AMR) code RAMSES (Teyssier 2002),

★ E-mail: eric@astro.lu.se

which treats dark matter and stars as collisionless particles and computes the fluid dynamics on a grid with adaptive resolution assuming ideal mono-atomic gas with adiabatic index $\gamma = 5/3$. Gas cooling is metallicity-dependent and treated using tabulated values. SF is controlled by a density threshold (100 cm^{-3}) with the SFR density computed from the cell gas density divided by the local free-fall time and scaled with an efficiency of 5 per cent. The details of this method are discussed in Agertz et al. (2013). The resolution of the grid follows a quasi-Lagrangian refinement strategy for which a cell is refined if it contains more than eight particles, or more than 4014 $M_\odot$ of baryonic matter, down to a spatial resolution of 9 pc. The initial conditions are the same as those used for the isolated disc in the Project AGORA: Assembling Galaxies Of Resolved Anatomy (Kim et al. 2014, 2016) and give a galaxy similar to the Milky Way, but with a gas fraction of 20 per cent.

Star particles are initially sampled with a mass resolution of 500 $M_\odot$ and immediately split into two groups using the initial mass function (IMF) from Kroupa (2001). (i) Low-mass stars (LMS; <8 $M_\odot$) are grouped and represented by a star particle for which we consider mass loss, Fe and O enrichment as well as momentum and energy injection from type Ia supernovae (SNe Ia) and asymptotic giant branch winds (for details, see Agertz et al. 2013). (ii) High-mass stars (HMS; ≥ 8 $M_\odot$) are treated as individual stars with a feedback model accounting for fast winds and core-collapse SNe. The mass-loss rate from the fast winds is computed with a modified version of the model by Dale & Bonnell (2008) and depends on stellar mass and metallicity. Core-collapse SNe occur when HMS leave the main sequence, which results in the injection of 10^{51} erg of energy in the gas. The main-sequence time is computed with the age–mass–metallicity fit of Raiteri, Villata & Navarro (1996). In cases when the Sedov–Taylor phase of the SN is unresolved (resulting in problems with a self-consistent development of the momentum build up during this phase), we explicitly inject the associated momentum using the method from Kim & Ostriker (2015). This ensures that we capture the effect of SNe even in regions with lower resolution.

In the `runaways` simulation, we add natal velocity kicks to the HMS sampled from the power-law distribution derived from *N*-body simulations of clusters by Oh & Kroupa (2016):

$$f_v \propto v^{-1.8}, \quad v \in [3, 385] \text{ km s}^{-1}. \tag{1}$$

This results in ∼14 per cent of stars being runaway[1] with a mean velocity of 90 km s^{-1}.

2.1 Low-mass runaway stars

The model in Andersson et al. (2020) limits the runaway mechanism to massive (>8 $M_\odot$) stars because these stars are responsible for the majority of stellar feedback. In this work, where we focus on tracing the resolved SF relation discussed in Section 1, we extend the model to sample individual stars in the mass range 4–100 $M_\odot$ in order to account for the non-negligible contribution to far-ultraviolet (FUV) emission of low-mass B-stars. These stars are an important contributor to our SF tracer (see Section 3.2). This extension is achieved by resampling the mass[2] of every high-mass star in the aforementioned mass range using the Kroupa IMF as a post-processing step. For technical reasons, we focus our analysis on ∼150 Myr of evolution of the galaxy, which roughly corresponds to the main-sequence lifetime of a 4-$M_\odot$ star. Therefore, we use this mass as a lower limit, resulting in a mass range between 4 and 100 $M_\odot$ for the HMS. We keep equation (1) (which does not have any mass dependence) as the velocity distribution. The resampling increases the stellar mass in the HMS population by 1.4×10^7 $M_\odot$. We remove mass from LMS corresponding to stars in the mass range $4-8$ $M_\odot$ as stars in this mass range are now included as HMS, resulting in a decrease in total mass of 1.7×10^7 $M_\odot$. The discrepancy between the two comes from mass loss due to stellar evolution, which is unaccounted for by this resampling.

3 RESULTS

3.1 Resolution dependence of the SF relation

At the end of the simulation, we derive the local SFR surface density by considering the mass of all stars with an age less than Δt in square bins with sides Δx placed in a uniform grid on the face-on view of the galaxies. We compare this to the gas surface density in the same bins and show the result in Fig. 1 for different choices of Δt (0.1 and 1 kpc) and Δx (2 and 10 Myr). We find that both galaxies follow the empirical relation $\Sigma_{\rm SFR} \propto \Sigma_{\rm g}^{1.4}$ (Kennicutt 1998; red dashed line in Fig. 1) at high gas densities, with a break at $\sim 10x2013$; 100 $M_\odot$ pc^{-2} going into the regime of slow SF.[3] Our galaxies show slightly faster SF at high surface densities ($\Sigma_{\rm g} \gtrsim 100$ $M_\odot$ pc^{-2}), although it is within the typical observed scatter in local spiral galaxies (e.g. Wong & Blitz 2002; Crosthwaite & Turner 2007; Kennicutt et al. 2007; Schuster et al. 2007; Bigiel et al. 2008). We find that increasing the resolution in time and space (i.e. decreasing Δt and Δx) results in less dispersion in the SF relation for both `runaways` and `no runaways`. We attribute this to a tighter correlation between newly formed stars and their natal gas clouds. Increasing Δt causes the scatter to increase because of the decoupling between stars and gas due to, for example, stellar feedback, dynamical drift and cloud dissolution. These different decoupling mechanisms have a range of spatial scales and time-scales. By increasing Δx, the variations of the gas density from region to region are averaged out, thus reducing the scatter in Fig. 1. However, increasing the temporal and spatial scales inevitably causes the measurements to deviate from the relation imposed from the local (cell-based) SF law. Similarly to our results, Khoperskov & Vasiliev (2017) found that on small spatial scales ($\lesssim$100 pc) the SF relation, as measured from FUV flux, deviates from that estimated by free-fall collapse of molecular clouds (see equation 21 in Krumholz & McKee 2005). This implies that on such scales the SF relation reflects the various evolutionary stages of individual star-forming clouds, so the relation is lost as clouds are destroyed or stars escape (see also Onodera et al. 2010).

Naturally, we find more scatter in the SF relation in the `runaways` model, as the velocity kicks amplify the decoupling of the

[1] We define runaway stars as stars with peculiar velocities >30 km s^{-1}. For a discussion on this value, see Andersson et al. (2020) and references therein.

[2] Assigning new masses inevitably leads to a different stellar evolution. This implies a discrepancy between the stellar evolution of the analysed stars and those evolved in the simulation. This is a limitation of our model, which we take into consideration when drawing conclusions from our results.

[3] We use the terms slow/fast SF to describe trends following long/short depletion times (i.e. lines of constant $\tau_{\rm dep} = \Sigma_{\rm g}/\Sigma_{\rm SFR}$). This is sometimes referred to as SF efficiency (then defined as the inverse of depletion time). In this work, we reserve the term efficiency to describe the conversion of gas mass into stellar mass (without concern for the time-scale). For a more detailed discussion on differences between SF efficiency and depletion time, see, for example, Semenov, Kravtsov & Gnedin (2018) and Renaud et al. (2019)

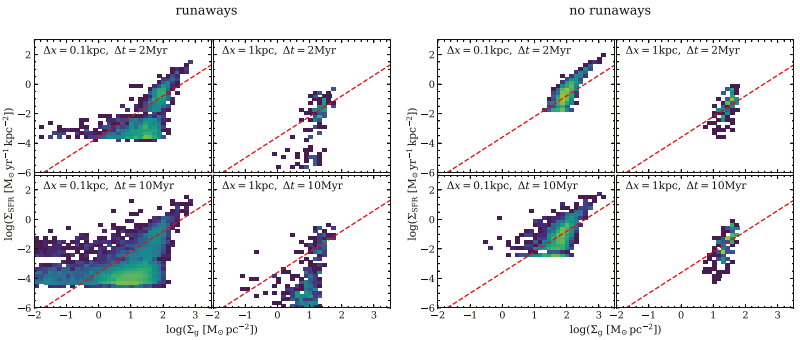

Figure 1. SFR surface density as a function of gas surface density for different resolutions in space (Δx) and time (Δt) for the models with (left) and without (right) runaway stars. Small values for Δx and Δt result in the tightest coupling between stars and gas. To guide the eye, the canonical SF relation with a slope of 1.4 (Kennicutt 1989, 1998) is shown by the red dashed line.

runaway stars from their natal gas. This masquerades as SF activity in regions of low Σ_g, as best seen in the left panels at $-1 \lesssim \log(\Sigma_g) \lesssim 0$ and $\log(\Sigma_{SFR}) \sim -2$.

In all panels of Fig. 1, there is a floor in Σ_{SFR} (most clearly visible for $\Delta x = 0.1$ kpc). This floor is a result of having a single star particle within a bin of size Δx, and is therefore set by the finite resolution in stellar masses. In `runaways`, the resolution is 4 $M_\odot$, while in the `no runaways` simulation, it is the mass of the entire unresolved stellar population. As discussed earlier, increasing Δt allows stars to travel further, reaching a larger range of densities. For very long time-scales ($\sim$100 Myr), runaway stars reach the outskirts of the galaxy, as discussed in the remainder of Section 3.

3.2 Runaway stars explain the observed low Σ_{SFR}

To avoid arbitrary time-scales (Δt), we create mock observations of the FUV flux. These are shown in Fig. 2 as surface brightness maps (left panel) from which we derive the SFR density. In the right panels, we plot them against the surface density of neutral and molecular hydrogen $\Sigma_{H\,I+H_2}$ (centre panels). This accounts for the dimming of FUV luminosity due to stellar evolution. Thus, it introduces a self-consistent time-scale, and lifts the requirement for an arbitrary Δt. This measurement of SFR is therefore consistent with that estimated observationally. Appendix A details how we produce and observe the mock spectra. The SFR is then computed as

$$\mathrm{SFR}\ (M_\odot\ \mathrm{yr}^{-1}) = 0.68 \times 10^{-28}\ I_{FUV}\ (\mathrm{erg\ s^{-1}\ Hz^{-1}}), \quad (2)$$

where I_{FUV} is the FUV intensity integrated over the *GALEX*-FUV filter. We calibrate the I_{FUV} such that the global SFR is the same as that measured in the simulation, as detailed in Appendix A. Equation (2) is identical to that derived by Salim et al. (2007) and later adopted by Leroy et al. (2008) and Bigiel et al. (2010). Note that this is the unobstructed SFR (not accounting for the contribution of embedded SF observed in infrared re-emission), and is therefore a lower limit of the SFR. However, our main finding is the feature in the low gas density regime, where the SFR densities are largely unaffected by extinction.

As shown in the top-right panel of Fig. 2, we find a radial dependence in the branch at low Σ_g and low Σ_{SFR}. In fact, we find that the transition into this feature corresponds to the regions outside the star-forming disc ($\gtrsim$10 kpc), thus explaining the absence of this branch in the `no runaways` simulation. The signal arises because the runaway mechanism ejects stars into regions where the density is too low for SF to be active. This creates the illusion of SF in gas with extremely low density, seen as the aforementioned feature extending from $\Sigma_{SFR} \sim 10^{-4}\ M_\odot\ \mathrm{yr}^{-1}\ \mathrm{kpc}^{-2}$, towards the bottom left. Initially, the branch roughly extends along a line of constant depletion time (shown by dashed lines) corresponding to extremely slow SF ($\tau_{dep} = 100$ Gyr), and flattens out as it reaches very low $\Sigma_{H\,I+H_2}$ ($\leq$0.1 $M_\odot$ pc^{-2}). A comparison to measurements of SF in outer regions of observed spiral galaxies (Bigiel et al. 2010) reveals a striking similarity to the feature produced by our runaway model. How far out the branch extends radially depends on the runaway model (i.e. the velocity distribution and the mass distribution of the stars), as discussed in Section 4.

The middle panels of Fig. 2 compare the gas structure between `runaways` and `no runaways`. The `runaways` (top) simulation features large under-dense regions within the star-forming disc (a few kpc from the centre). The repeated transport of runaway stars into low-density medium (e.g. inter-arm) allows these feedback bubbles to expand to large volumes and to survive for longer time-scales compared with the `no runaways` case where they are confined to dense media. As in the galactic outskirts, $\log(\Sigma_{SFR}) \sim -6$, these low gas surface density regions at $\log(\Sigma_{SFR}) \sim -2$ harbour an unexpected SF activity introduced by the presence of runaway stars. Contrary to the galactic outskirts, these measurements are indicative of fast SF ($\tau_{dep} \sim 10$ Myr) as seen in the top-right panel of Fig. 2, because runaway stars are more abundant in the inner parts of galactic discs.

4 DISCUSSION

The physical process responsible for the observational detection of young stars at gas surface densities as low as 1 $M_\odot$ pc^{-2} in resolved galaxies (e.g. Bigiel et al. 2008, 2010; Wyder et al. 2009; Elmegreen & Hunter 2015) has been debated (see Krumholz 2014 for a review). Elmegreen (2015) argued that the longer depletion times in the outskirts arises from disc flaring, which reduces the

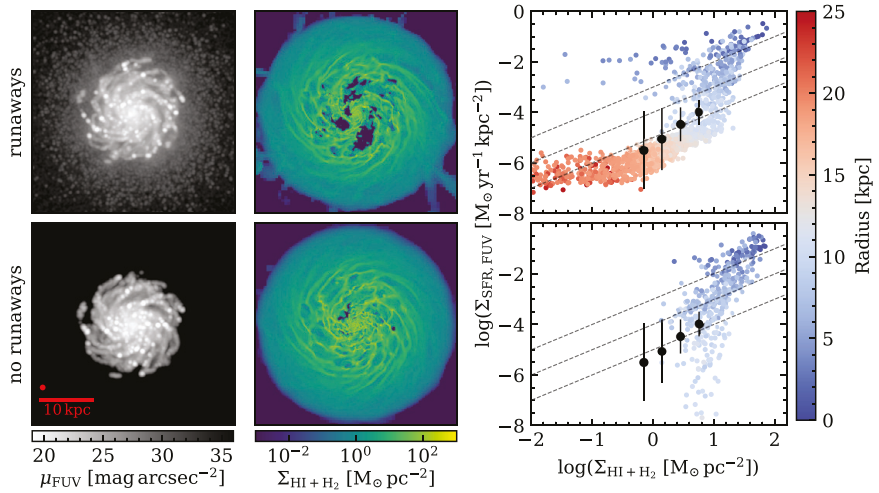

Figure 2. Left: FUV surface brightness maps derived by assigning spectra to each star (see text for details). Each pixel has been convolved with a Gaussian filter with FWHM of 4 arcsec converted to physical units by assuming a distance of 20 Mpc to the galaxies. The point spread function is shown by the red circle. Center: surface density of H I and H_2 gas along the line of sight. The scale is the same as in the left panel. Right: resolved SFR density as a function of gas surface density colour-coded by distance to the centre of the galaxy. $\Sigma_{\rm SFR,\,FUV}$ is computed from FUV intensity (equation 2), in 1-kpc squares. The colour-coding clearly shows that the low $\Sigma_{\rm SFR}$ feature is a radial trend related to the inclusion of runaway stars. The black dots with error bars show the mean and scatter for the resolved KS relation observed in the outer regions of spiral galaxies by Bigiel et al. (2010). The dashed lines correspond to constant depletion times of 100, 10 and 1 Gyr from bottom to top, respectively.

local volume density of gas, while keeping the surface density relatively high. This contradicts our `no runaways` model, where such a feature should be visible. Krumholz (2013) suggested that the trend at low $\Sigma_{\rm SFR}$ can be explained by inefficient SF in molecule-poor gas in the outskirts of galaxies. A key property of their model is the background interstellar radiation, which we do not take into account in the SF law in our simulations. Therefore, we cannot rule out low levels of SF in molecule-poor gas in the galactic outskirts. Nevertheless, runaway stars, as modelled in this work, must contribute to the observed SF signal, at least to some extent. A full understanding of the contribution from runaway stars likely requires advanced models with full *N*-body treatment of all stellar clusters, including consistent descriptions of the clusters' natal properties, such as the binary fraction. Furthermore, this needs to be taken into account over cosmological times to obtain a self-consistent local FUV background. This is beyond the scope of current models.

Star formation in very diffuse gas could either reflect *in situ* SF, or result from the rapid migration of stars, as we advocate here. As discussed above, the former case calls for an additional SF regime. However, the two possibilities would lead to a different stellar mass function. By comparing FUV flux with Hα emission from H II regions, Meurer et al. (2009) found a deficit of massive O stars associated with the FUV bright outskirts (see also Werk et al. 2010). Note that there is a debate surrounding their conclusions (see Fumagalli, da Silva & Krumholz 2011; Andrews et al. 2013, 2014). Unless arguing for a non-universal IMF (e.g. Pflamm-Altenburg & Kroupa 2008), a deficit in O stars supports our scenario as we find that the main contributors to the FUV signal are stars in the mass range 5–7M$_\odot$, with almost no contribution from O stars with mass >20 M$_\odot$.

In this work, we apply a model that treats stars as individual particles on galactic scales, which is numerically challenging. In order to reduce computational costs, the model in Andersson et al. (2020) is limited to massive stars (>8 M$_\odot$) because these trace the majority of stellar feedback. In this work, we have extended the model to include individual stars down to 4 M$_\odot$, thus accounting for their contribution to the FUV flux in galaxies.[4] The velocity distribution (equation 1) is that of all stars in a natal cluster, implying that in principle we can choose to resample for any stellar masses. However, because of mass segregation and the dynamics of many-body interactions, the velocity distribution is known to be mass-dependent. More massive stars are more likely to receive stronger kicks. Maíz Apellániz et al. (2018) estimated that, in the field, 10–12 per cent of O stars are runaways, while this is fraction is reduced to ∼6 per cent for B stars (see also Eldridge et al. 2011). In future work, we will investigate how our results depend on varying the distribution of kick velocities.

[4]Although the contribution to FUV intensity is limited for low-mass stars, their long main-sequence lifetime makes them important for the radial dependence of the SF relations.

5 SUMMARY AND CONCLUSIONS

Using hydrodynamic simulations of an isolated Milky Way-like galaxy (Andersson et al. 2020), we show how runaway stars change the appearance of SF, as seen in the Σ_g–Σ_{SFR} plane. We demonstrate how the SF relation depends sensitively on the spatial and temporal scales over which they are averaged. This sensitivity is increased by runaway stars, because their high velocities imply that they quickly leave their natal environments. By estimating the SFR from the FUV intensity, we remove the necessity of choosing an ad hoc time-scale and we produce a SF relation consistent with that derived from observations.

Our main result is a feature in the SF relation at $\Sigma_{SFR} \sim 10^{-4}$–$10^{-6}$ $M_\odot$ yr^{-1} kpc^{-2} in low surface density gas, with a galactocentric radial dependence, found exclusively in our model including runaway stars. This feature is in excellent agreement with that observed in the outer regions of spiral galaxies (Bigiel et al. 2010). We show that this feature arises by ejecting massive FUV emitting stars (via the runaway mechanism) from SF regions into low-density gas. This results in the presence of young stars in gas with densities that are too low to trigger SF. Therefore, it produces an unexpected signature of SF, with a strong radial dependence.

In conclusion, we argue that the SF relation in the outer regions of spiral galaxies is produced by a small, albeit observable, population of individual stars formed in denser environments and transported there by the runaway mechanism. Although our model cannot rule out SF in atomic gas (Krumholz 2013), runaway stars are at the very least a contributing, if not dominant, factor to establishing the SF relation in outer regions of galaxies.

ACKNOWLEDGEMENTS

We thank the anonymous referee for comments that have improved this letter. We also express gratitude for the stimulating discussions at the 2020 Ringberg Virtual Seminar Series. EA acknowledges discussions with Mark Krumholz. We acknowledge support from the Knut and Alice Wallenberg Foundation, the Swedish Research Council (grant 2014-5791) and the Royal Physiographic Society of Lund. We used computational resources at LUNARC hosted at Lund University, on the Swedish National Infrastructure for Computing (SNIC 2018/3-649), as well as allocation LU 2019/2-27.

DATA AVAILABILITY

The data underlying this article will be shared on reasonable request to the corresponding author.

REFERENCES

Agertz O., Kravtsov A. V., Leitner S. N., Gnedin N. Y., 2013, ApJ, 770, 25
Andersson E. P., Agertz O., Renaud F., 2020, MNRAS, 494, 3328
Andrews J. E. et al., 2013, ApJ, 767, 51
Andrews J. E. et al., 2014, ApJ, 793, 4
Bigiel F., Leroy A., Walter F., Brinks E., de Blok W. J. G., Madore B., Thornley M. D., 2008, AJ, 136, 2846
Bigiel F., Leroy A., Walter F., Blitz L., Brinks E., de Blok W. J. G., Madore B., 2010, AJ, 140, 1194
Blaauw A., 1961, Bulletin of the Astronomical Institutes of the Netherlands, 15, 265
Bolatto A. D. et al., 2011, ApJ, 741, 12
Ceverino D., Klypin A., 2009, ApJ, 695, 292
Crosthwaite L. P., Turner J. L., 2007, AJ, 134, 1827
Dale J. E., Bonnell I. A., 2008, MNRAS, 391, 2
Dorigo Jones J., Oey M. S., Paggeot K., Castro N., Moe M., 2020, ApJ, 903, 43
Eldridge J. J., Langer N., Tout C. A., 2011, MNRAS, 414, 3501
Elmegreen B. G., 2015, ApJ, 814, L30
Elmegreen B. G., 2018, ApJ, 854, 16
Elmegreen B. G., Hunter D. A., 2015, ApJ, 805, 145
Federrath C., 2013, MNRAS, 436, 3167
Fumagalli M., da Silva R. L., Krumholz M. R., 2011, ApJ, 741, L26
Gies D. R., 1987, ApJS, 64, 545
Gies D. R., Bolton C. T., 1986, ApJS, 61, 419
Hoogerwerf R., de Bruijne J. H. J., de Zeeuw P. T., 2000, ApJ, 544, L133
Jonsson P., 2006, MNRAS, 372, 2
Kennicutt R. C., 1989, ApJ, 344, 685
Kennicutt R. C., 1998, ApJ, 498, 541
Kennicutt R. C., Evans N. J., 2012, ARA&A, 50, 531
Kennicutt R. C. et al., 2007, ApJ, 671, 333
Khoperskov S. A., Vasiliev E. O., 2017, MNRAS, 468, 920
Kim J-h. et al., 2014, ApJS, 210, 14
Kim J-h. et al., 2016, ApJ, 833, 202
Kim C-G., Ostriker E. C., 2015, ApJ, 802, 99
Kim C-G., Ostriker E. C., 2018, ApJ, 853, 173
Kroupa P., 2001, MNRAS, 322, 231
Krumholz M. R., 2013, MNRAS, 436, 2747
Krumholz M. R., 2014, Phys. Rep., 539, 49
Krumholz M. R., McKee C. F., 2005, ApJ, 630, 250
Krumholz M. R., McKee C. F., Tumlinson J., 2009, ApJ, 699, 850
Leitherer C. et al., 1999, ApJS, 123, 3
Leitherer C., Ortiz Otálvaro P. A., Bresolin F., Kudritzki R.-P., Lo Faro B., Pauldrach A. W. A., Pettini M., Rix S. A., 2010, ApJS, 189, 309
Leitherer C., Ekström S., Meynet G., Schaerer D., Agienko K. B., Levesque E. M., 2014, ApJS, 212, 14
Leroy A. K., Walter F., Brinks E., Bigiel F., de Blok W. J. G., Madore B., Thornley M. D., 2008, AJ, 136, 2782
Li A., Draine B. T., 2001, ApJ, 554, 778
Maíz Apellániz J., Pantaleoni González M., Barbá R. H., Simón-Díaz S., Negueruela I., Lennon D. J., Sota A., Trigueros Páez E., 2018, A&A, 616, A149
Meurer G. R. et al., 2009, ApJ, 695, 765
Moyano Loyola G. R. I., Hurley J. R., 2013, MNRAS, 434, 2509
Oh S., Kroupa P., 2016, A&A, 590, A107
Onodera S. et al., 2010, ApJ, 722, L127
Pflamm-Altenburg J., Kroupa P., 2008, Nature, 455, 641
Poveda A., Ruiz J., Allen C., 1967, Boletin de los Observatorios Tonantzintla y Tacubaya, 4, 86
Raddi R., Irrgang A., Heber U., Schneider D., Kreuzer S., 2020, A&A, in press( )
Raiteri C. M., Villata M., Navarro J. F., 1996, A&A, 315, 105
Renaud F., Kraljic K., Bournaud F., 2012, ApJ, 760, L16
Renaud F., Bournaud F., Agertz O., Kraljic K., Schinnerer E., Bolatto A., Daddi E., Hughes A., 2019, A&A, 625, A65
Roychowdhury S., Chengalur J. N., Begum A., Karachentsev I. D., 2009, MNRAS, 397, 1435
Salim S. et al., 2007, ApJS, 173, 267
Schaye J., 2004, ApJ, 609, 667
Schmidt M., 1959, ApJ, 129, 243
Schuster K. F., Kramer C., Hitschfeld M., Garcia-Burillo S., Mookerjea B., 2007, A&A, 461, 143
Semenov V. A., Kravtsov A. V., Gnedin N. Y., 2018, ApJ, 861, 4
Silva M. D. V., Napiwotzki R., 2011, MNRAS, 411, 2596
Stone R. C., 1991, AJ, 102, 333
Teyssier R., 2002, A&A, 385, 337
Vázquez G. A., Leitherer C., 2005, ApJ, 621, 695
Werk J. K. et al., 2010, AJ, 139, 279
Wong T., Blitz L., 2002, ApJ, 569, 157
Wyder T. K. et al., 2009, ApJ, 696, 1834

APPENDIX A: GENERATING SYNTHETIC SPECTRA FOR STELLAR POPULATIONS

The mock observations used in this work are derived by combining a wave propagation method similar to that used in SUNRISE (Jonsson 2006) with stellar spectra from a modified version of the stellar population synthesis code STARBURST99 (Leitherer et al. 1999, 2010, 2014; Vázquez & Leitherer 2005). All HMS use evolving spectra for individual stars while LMS use an evolving spectra from the stellar population with stars in the relevant mass range. The spectra of each source are propagated through the gas at the highest AMR resolution (∼9 pc) to the observer. We account for extinction using a dust attenuation curve from Li & Draine (2001) assuming a uniform dust-to-gas ratio of 0.01. We compute the photometric intensity in the *GALEX*-FUV band for the stars that formed during the simulation (i.e. younger than 250 Myr). To account for missing FUV flux from unresolved populations and loss of mass due to sampling new masses for HMS particles (see Section 2.1), we artificially boost $I_{\rm FUV}$ such that the global SFR derived from equation (2) matches that from the simulation. Furthermore, we apply a Gaussian filter with FWHM of 4 arcsec (i.e. standard deviation of $\sigma = 1.7$ arcsec) to all pixels to simulate the angular resolution of the *GALEX* satellite. To convert to physical units, we assume a distance of 20 Mpc. The surface brightness maps were computed from the magnitudes using

$$m_{\rm FUV} = -2.5 \log \left(\frac{f_\nu}{\rm erg\,s^{-1}\,cm^{-2}\,Hz^{-1}} \right) - 48.6, \tag{A1}$$

where f_ν is the spectral flux density in the *GALEX*-FUV band. When we compute f_ν we assume an initial distance of 10 pc and add a distance modulus corresponding to 20 Mpc. For the conversion to surface brightness, we compute the pixel angular size at a distance of 20 Mpc.

This paper has been typeset from a TEX/LATEX file prepared by the author.

Paper III

MNRAS 000, 1–16 (2022) Preprint 15 September 2022 Compiled using MNRAS LATEX style file v3.0

INFERNO: Galactic winds in dwarf galaxies with star-by-star simulations including runaway stars

Eric P. Andersson[1]★, Oscar Agertz[1], Florent Renaud[1] and Romain Teyssier[2]
[1]Department of Astronomy and Theoretical Physics, Lund Observatory, Box 43, SE-221 00 Lund, Sweden
[2]Department of Astrophysical Sciences, Princeton University, Princeton, NJ 08544, USA

Accepted XXX. Received YYY; in original form ZZZ

ABSTRACT

The formation and evolution of galaxies have proved sensitive to the inclusion of stellar feedback, which is therefore crucial to any successful galaxy model. We present INFERNO, a new model for hydrodynamic simulations of galaxies, which incorporates resolved stellar objects with star-by-star calculations of when and *where* the injection of enriched material, momentum and energy takes place. INFERNO treats early stellar kinematics to include phenomena such as walkaway and runaway stars. We employ this innovative model on simulations of a dwarf galaxy and demonstrate that our physically motivated stellar feedback model can drive vigorous galactic winds. This is quantified by mass and metal loading factors in the range 10 – 100, and an energy loading factor close to unity. Outflows are established close to the disc, are highly multi-phase, spanning almost 8 order of magnitude in temperature, and with a clear dichotomy between mass ejected in cold, slow-moving ($T \lesssim 10^5$ K, $v < 100$ km s^{-1}) gas and energy ejected in hot, fast-moving ($T > 10^6$ K, $v > 100$ km s^{-1}) gas. In contrast to massive disc galaxies, we find a surprisingly weak impact of the early stellar kinematics, with runaway stars having little to no effect on our results, despite exploding in diffuse gas outside the dense star-forming gas, as well as outside the galactic disc entirely. We demonstrate that this weak impact in dwarf galaxies stems from a combination of strong feedback and a porous interstellar medium, which obscure any unique signatures that runaway stars provide.

Key words: methods: numerical – galaxies: evolution – ISM: jets and outflows

1 INTRODUCTION

Galactic evolution is governed by a manifold of connected processes over a vast range of physical scales. An important aspect of this evolution, and an example of this scale-coupling is galactic scale winds driven by feedback processes in the interstellar medium (ISM). This generates a baryon cycle (for a review, see Veilleux et al. 2005; Zhang 2018). Understanding the injection of energy and momentum on parsec scales (McKee & Ostriker 1977; Katz 1992; Kim & Ostriker 2015), how this translates into outflows (Schroetter et al. 2016; Chisholm et al. 2017; Fielding et al. 2017), and how the ejected material evolves after leaving the galaxy (Tumlinson et al. 2017; Fielding et al. 2020) are fundamental questions for galaxy theory. To tackle these questions, semi-analytical models (e.g., Baugh 2006; Benson 2010), large-scale cosmological simulations (e.g., Schaye et al. 2015; Vogelsberger et al. 2014; Nelson et al. 2019), and simulations of the ISM (e.g., Walch et al. 2015; Kim et al. 2020a,b) have been employed. Progress made towards answering these questions can be attributed both to advances in numerical methods and modelling, as well as an improved understanding of the physics involved (see Somerville & Davé 2015, for a review). The complex physics of gaseous material innate to these problems make hydrodynamic simulations combined with sub-grid models for the relevant unresolved physics highly suitable for this task (see, e.g., Wheeler et al. 2019; Agertz et al. 2020; Smith et al. 2021). The recent progress made with these kinds of models has in part been facilitated by galaxy-scale simulations reaching a higher resolution, thereby better resolving processes within the ISM (and consequently the star-forming clouds), while capturing the global dynamics of evolving galaxies.

Today, galaxy simulations routinely reach parsec-scale resolution, with star-particles representing individual stars (see, e.g., Hu et al. 2016; Emerick et al. 2018; Andersson et al. 2020, 2021; Hirai et al. 2021; Hislop et al. 2021; Gutcke et al. 2021), and in fact, *should* be done in this way to avoid the many restrictions (e.g., location of individual stars) imposed by the traditional approach[1]. Star-by-star models allow for a detailed account of when and *where* individual stars inject momentum, energy and enriched material. The locality of supernovae (SNe) has already been shown to affect the efficiency of stellar feedback (e.g., Walch et al. 2015; Girichidis et al. 2016; Gatto et al. 2017), in turn altering the properties of massive galaxies (e.g., Ceverino & Klypin 2009; Kimm & Cen 2014; Andersson et al. 2020) and dwarf galaxies (e.g., Gutcke et al. 2022; Steinwandel et al. 2022). This indicates that star-by-star models are necessary to fully study

★ E-mail: eric@astro.lu.se

[1] To relieve the computational cost of tracking the vast number of stars hosted by galaxies, stars are typically modelled as single stellar populations which are tracked by a single particle. This approach becomes less sensible when the mass of the star-particles is smaller than that of individual stars, which is often the case in highly resolved simulations.

cloud evolution, star formation, stellar feedback, chemical mixing, and thus galaxy evolution as a whole.

To this end, we present the INdividual stars with Feedback, Enrichment and Realistic Natal mOtions (INFERNO) model, a new versatile star-by-star model implemented in the *N*-body+hydrodynamics code Ramses (Teyssier 2002). The INFERNO model is a step towards a complete account of the physics that drives galaxy formation and evolution. In its current state, INFERNO account for feedback processes from giant branch stars, the rapidly evolving O and B type stars, core-collapse supernovae (CCSNe) and type Ia supernovae (SNeIa). Furthermore, INFERNO treats the early collisional dynamics in natal star clusters, which is one origin of walkaway and runaway stars (Poveda et al. 1967; Oh & Kroupa 2016).

How massive runaway stars affect galaxy evolution is still a debated question (for a review, see Naab & Ostriker 2017). These types of fast-moving stars are key examples of processes which relocate SNe. As mentioned before, this affects the stellar feedback and as a result outflows. This, often called *random versus peak driving*, has been explained by the interplay between clustered star formation (and consequently clustered feedback of short-lived stars, see e.g., Mac Low & McCray 1988; Nath & Shchekinov 2013; Sharma et al. 2014; Keller et al. 2014, 2016; Gentry et al. 2017, 2019), and more isolated SNeIa (Tang et al. 2009), as well as CCSNe with progenitors being fast-moving runaway stars (see e.g., Ceverino & Klypin 2009; Kimm & Cen 2014; Andersson et al. 2020). Nonetheless, uncertainties regarding the fraction of runaway stars (Stone 1991; Silva & Napiwotzki 2011; Eldridge et al. 2011; Maíz Apellániz et al. 2018; Renzo et al. 2019; Drew et al. 2021) makes their contribution to isolated SNe an unsolved problem. Furthermore, simulations with an explicit treatment of runaway stars find contradicting results. Andersson et al. (2020) found that runaway stars exploding in low-density gas located in the inter-arm regions of large spiral galaxies result in increased outflow rates. In the dwarf galaxy simulations presented in Steinwandel et al. (2022), runaway stars were found to escape the disc of the galaxy, providing thermal energy directly to gas in the circumgalactic medium (CGM). While both these works found runaway stars to play an important role for the galactic scale outflows, Kim & Ostriker (2018) found runaway stars to have negligible effects on these outflows in simulations of stratified kpc-sized patches of the ISM (see also Kim et al. 2020a). Because of significant model variation (e.g. environment, runaway star model, and numerical scheme), no consensus is yet reached for the effect that runaway stars have on feedback physics.

One aim of this work is to study the role that the natal kinematics of individual stars (including walkaway and runaway stars) have on dwarf galaxies, in particular, the role played by the fraction of runaway stars. Dwarf galaxies are both common in the Universe (Sawala et al. 2015; Read et al. 2017; Behroozi et al. 2019), and they exhibit strong winds relative to their star formation rates (Chisholm et al. 2017; McQuinn et al. 2019). Furthermore, galactic outflows driven by strong feedback are a necessary component in the Λ-cold dark matter cosmological model to explain the faint-end of the galaxy-luminosity function (Dekel & Silk 1986; Benson et al. 2003), and the cored density profiles observed in many dwarf galaxies (Moore 1994; Teyssier et al. 2013; Read et al. 2016). Their low escape velocities and relatively large gas contents make them sensitive probes of stellar feedback physics (Rosdahl et al. 2015; Hu et al. 2017; Emerick et al. 2018; Su et al. 2018; Hu 2019; Smith et al. 2019; Wheeler et al. 2019; Agertz et al. 2020; Smith et al. 2021), the stellar initial mass function (IMF) (Smith 2021; Prgomet et al. 2022), and cosmic rays (Dashyan & Dubois 2020; Farcy et al. 2022; Girichidis et al. 2022). As numerical laboratories, the small sizes of dwarf galaxies make them less computationally expensive compared to Milky-Way-sized objects, therefore allowing for a large number of simulations at high numerical resolution. In the case of this work, it enables us to run a suite of simulations with a varying fraction of runaway stars, while achieving a resolution high enough to capture important aspects of stellar feedback (e.g. the Sedov-Taylor evolution of SNe, see more details in Section 3).

Our paper describes our star-by-star model INFERNO, as well as presents the theoretical work that motivations our model in Section 2, details the numerical set-up and initial conditions (ICs) in Section 3, and presents the results in Section 4. We discuss our results and place our work in a wider context in Section 5, and finally summarize and conclude in Section 6.

2 THE INFERNO MODEL

2.1 Star formation, IMF sampling & initial kinematics

Following Andersson et al. (2020, 2021), our model incorporates particles representing individual stars to follow stellar motions and feedback for stars above a mass threshold. The threshold is set by a parameter $m_\star$, and its value determines whether the feedback is calculated for individual stars, or taken as an average over the stellar population below $m_\star$. Note that $m_\star$ can take any value within a given IMF, and while small values employ a more detailed stellar model, it increases the computational cost. Using any pre-defined IMF, individual stars are stochastically sampled from mass $M_{\rm sf}$ (set as a user-defined parameter; see details in next paragraph). Star formation ensues in each cell with cold ($T < 10^4$ K) and dense ($\rho_{\rm g} > 500$ cm^{-3}) gas. At each fine time step, several $M_{\rm sf}$ units of mass can be spawned through a Poisson sampling of a Schmidt-like star formation law,

$$\dot{\rho}_{\rm sf} = \epsilon_{\rm ff} \frac{\rho_{\rm g}}{t_{\rm ff}}, \tag{1}$$

where $\epsilon_{\rm ff} = 0.1$ is the star formation efficiency per free-fall time, and $t_{\rm ff} = \sqrt{3\pi/32 G \rho_{\rm g}}$ is the local gas free-fall time. These choices are selected to match the resolution of our simulation, ensuring that our galaxy matches the observed Schmidt-Kennicutt relation (Schmidt 1959; Kennicutt 1989). The population of stars with mass ($m < m_\star$) is traced by one star-particle per star formation event, and can inject feedback based on the model from Agertz et al. (2013). In this work, we keep $m_\star$ small enough (2 M$_\odot$), such that in practice this model is never applied, i.e. stars in this mass range never enter a stellar evolution phase with mass, momentum or energy ejection.

To sample individual stars from stellar ensembles, we employ the method by Sormani et al. (2017), in which the IMF is sampled in predefined mass bins. A detailed description of our implementation can also be found in Andersson et al. (2020, see also Sormani et al. 2017). In short, the number of stars in a given stellar mass bin is determined by random number generation from a Poisson distribution with appropriate pre-computed weights. To avoid oversampling, the available mass is sampled consecutively from low to high mass, stopping the process when the available mass is reached[2]. To minimise this problem we choose the mass of stellar ensembles to be $M_{\rm sf} = 500$ M$_\odot$, ensuring a well sampled IMF (Smith 2021). For this work we use the IMF from Kroupa (2001), defined as a split power-law function $\xi \propto m^{-\alpha_i}$, with two different mass ranges; $\alpha_1 = 1.3$ for masses $0.08 - 0.5$ M$_\odot$, and $\alpha_2 = 2.3$ for masses $0.5 - 100$ M$_\odot$.

[2] This model sometimes sufferers from under-sampling the most massive stars, which affects the stellar feedback budget. However, the steepness of the IMF makes this under-sampling rare (handful of times per Gyr).

At birth, all stellar particles receive the velocity of the gas from which they formed. For individual stars, we give the particles an additional radial velocity with isotropic distribution to model the dynamics which are unresolved in our collisionless simulations. We include two models for this: 1) stars from the same stellar ensemble receive an innate velocity dispersion σ_v, using random sampling from a Gaussian distribution (referred to as `stir`); 2) velocity kicks to simulate walkaway and runaway stars[3], which overrides the velocity from `stir` (referred to as `kick`). The `stir` model is applied to avoid stars formed at a single instance to remain perfectly overlapping. We emphasise that the `stir` model does not entail an accurate treatment of the collisional dynamics on small scales, which are affected by gravitational softening. The `kick` model, applied to a fraction $f_{\rm kick}$ of the massive (> 8 M$_\odot$, unless otherwise stated) stars, models walkaway and runaway stars associated with early dynamical interactions in natal star clusters. For this work, we use the inverse power-law distribution $f_v \propto v^{-1.8}$, covering the range $3 < v < 375$ km s^{-1}. This is the velocity distribution of stars escaping a $10^{3.5}$ M$_\odot$ natal cluster in its first 3 Myr of evolution, as modelled by Oh & Kroupa (2016). This is the same distribution used for massive stars (> 8 M$_\odot$) in Andersson et al. (2020), and one of two runaway star models tested by Steinwandel et al. (2022).

2.2 Stellar evolution & feedback

INFERNO accounts for the injection of energy, momentum and chemically enriched material, with a model taking the initial mass, metallicity and age of a given star into consideration. These models apply to different stellar evolutionary stages, and each is described in detail throughout this section. The main factor determining when stars move between evolutionary phases is the main-sequence lifetime. We calculate this using the fitting function from Raiteri et al. (1996) calibrated to the Padova tracks (Alongi et al. 1993; Bressan et al. 1993; Bertelli et al. 1994).

The chemical evolution of stars and gas is based on stars inheriting the chemical composition of the gas from which they form, and then injecting chemically enriched material (henceforth referred to as yields). To determine the yield of a given stellar evolution process we use bilinear interpolation of yield tables from NuGrid (Pignatari et al. 2016; Ritter et al. 2018). This set provides yields for a wide range of stellar masses and metallicities, although we note that there are other yield tables in the literature, with large differences in total yield (see Buck et al. 2021, for a comparison). This method allows us to track up to 80 of the elements in the periodic table, which we describe in more detail in Andersson et al. (*in prep.*). The stellar evolution models depend only on the total stellar metal mass which we approximate as $M_Z = 2.09 M_{\rm O} + 1.06 M_{\rm Fe}$, based on Solar mixture (Asplund et al. 2009).

[3] Walkaways as stars are typically referred to as stars with peculiar velocities $v < 30$ km s^{-1}, while runaways have $v > 30$ km s^{-1}. We use this convention in our work. These stars originate from either the internal dynamics of star clusters (Poveda et al. 1967), or via binary system breakup due to instantaneous mass loss from companion SNe (Blaauw 1961). Both these scenarios favour more massive stars becoming runaways. The former is due to mass segregation, moving massive stars to the dense centre of the cluster, and the latter is due to binary fraction increasing with stellar mass. The kick distribution we apply to escaping stars was estimated from numerical simulations of the first 3 Myr of the clusters evolution (see Oh & Kroupa 2016, for details). This does not account for SNe break-up of binary systems, which is constrained by the time of the first SNe ($\gtrsim 3$ Myr). The velocity distribution used for escapers results in 86% walkaways and 14% runaways.

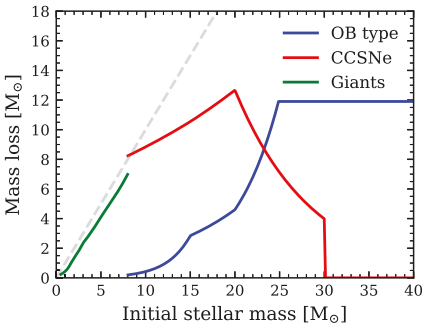

Figure 1. Total mass loss as a function of initial stellar mass shown for the feedback sources considered, denoted in the legend. The grey dashed line shows the equivalence between the two axes. Values are derived by interpolating the results from the NuGrid data sets, and applying the limits constraining the interpolations (see main text for details).

Similarly to the yields, all mass loss is computed by interpolating the NuGrid tables. Figure 1 shows the total mass lost through different feedback channels as a function of the initial mass of a given star. Note that we ensure that the mass expelled by a given star can never result in particles with a negative mass.

2.2.1 *Winds from massive O & B stars*

The most massive stars (> 8 M$_\odot$) have high enough luminosity to push away material from their surface during the main-sequence phase of their evolution. During this phase, stars launch a fast (~ 1000 km s^{-1}) stellar wind. This wind is driven by the extreme stellar radiation, pushing on the stellar envelope through resonant line absorption (Vink 2015). Due to its early onset after the formation of a star, this wind can aid the disruption of star-forming clouds, suppresses star formation locally, and affects the clustering of stars (see e.g., Dale & Bonnell 2008; Rosen et al. 2014; Lancaster et al. 2021).

Our model assumes that all stars in the mass range $8 - 60$ M$_\odot$[4] launch a wind at a constant velocity of 1000 km s^{-1}, for the entire duration of the main sequence. Depending on the stellar mass, the mass loss rates range from roughly $10^{-8} - 10^{-6}$ M$_\odot$ yr^{-1}. As shown in Figure 1, the mass-loss rate increases non-linearly with stellar mass making extrapolation above the NuGrid upper mass limit (25 M$_\odot$) sometimes exceeding the initial stellar mass. To avoid this, we assume a constant mass-loss rate for all stars more massive than this limit. This implies that our model likely underestimates the amount of momentum and energy from these winds, although we note that typical IMFs make stars with mass > 25 M$_\odot$ rare.

[4] We note that this mass range does not include all B type stars. For lower mass stars (< 8 M$_\odot$) of this class, we refer to Section 2.2.3 for details about wind treatment.

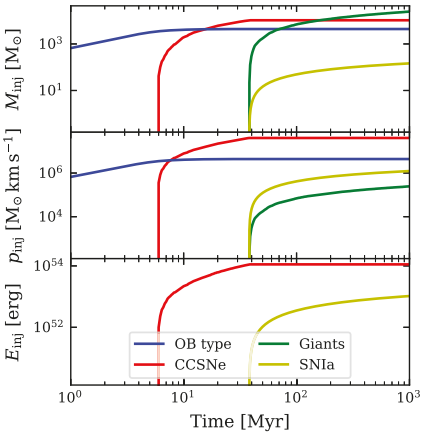

Figure 2. Cumulative sum of the mass (upper), momentum (middle) and energy (lower) injected as a function of time by a 10^5 M$_\odot$ mono-age population of stars. Different sources are distinguished by line colour denoted in the figure legend.

2.2.2 *Core-collapse supernovae*

CCSNe results in the instantaneous release of $\sim 10^{51}$ erg of energy, making them a crucial component of any stellar feedback model (McKee & Ostriker 1977; Katz 1992; Kimm et al. 2015). The explosion is triggered at the end of the main-sequence for massive stars ($\gtrsim$ 8 M$_\odot$), however, the exact mechanism behind the explosion is not fully understood[5]. This uncertainty is the often-called *islands of explodability* (Janka 2012; Zapartas et al. 2021), stating that many models favour specific ranges in stellar mass to trigger an explosion, with the alternative being the direct collapse to a compact object. Typically, the most massive stars go through the direct collapse channel, however, extremely massive stars ($>$ 100 M$_\odot$) can undergo pair-instability explosions resulting in the complete disruption of the star (see e.g. Fryer et al. 2001).

Keeping the above complexity in mind, our model assumes that all stars in the mass range 8 – 30 M$_\odot$ undergo SNe after leaving the main sequence, instantaneously depositing 10^{51} erg of energy, along with chemically enriched material, into its immediate surroundings. The mass expelled during the SNe event is shown by the red line in Figure 1. For stellar masses above this range, we assume that leaving the main sequence results in direct collapse into a black hole, without any injection of energy or enriched material. This implies that the earliest possible injection of energy via SNe occurs 6 Myr after star formation (see Figure 2).

[5] The currently favoured hypothesis is delayed neutrino-heating, which ejects the outer layers of the stars (see Janka 2012, for a review).

2.2.3 *Stellar winds from giant stars*

Stars more massive than 0.5 M$_\odot$ enter a giant phase for a short period after leaving the main-sequence unless the star undergoes SNe before this. In this phase, energy is mostly generated through hot-bottom burning in convective shells exterior to the stellar core, periodically supplying the core with fuel giving rise to explosive burning (see Höfner & Olofsson 2018, for a review). These surges in energy (often called thermal pulses) drive a stellar wind with mass loss rates in the range $10^{-8} - 10^{-4}$ M$_\odot$ yr^{-1} at velocities $\approx$ 10 km s^{-1} (see e.g. Schöier & Olofsson 2001; Olofsson et al. 2002; González Delgado et al. 2003; Ramstedt et al. 2009; Eriksson et al. 2014). Although this wind makes up only a small fraction of the stellar feedback energy budget, it is crucial for the chemical enrichment of the ISM. A source of uncertainty in stellar evolution models with regards to giant stars is the intermediate phase (7.5 – 9 M$_\odot$) between evolving into a white dwarf or CCSNe (Poelarends et al. 2008; Doherty et al. 2017). After leaving the main-sequence, these stars are massive enough to ignite carbon-burning in their core, resulting in a large number of thermal pulses giving rise to a super asymptotic giant branch phase. During this phase, material fueled to the core can result in its mass exceeding the Chandrasekhar mass, leading to core explosion.

Our model assumes that all stars in the mass range 0.5 – 8 M$_\odot$ enter a post-main-sequence phase, during which a stellar wind is expelled. The wind is injected as a source of momentum at a constant mass loss rate of 10^{-5} M$_\odot$ yr^{-1} with a velocity of 10 km s^{-1}. The duration of this phase is set by the total mass lost (green line in Figure 1), computed from the NuGrid tables, i.e. winds are expelled until no more mass is available, in which case the star is considered to have become a white dwarf. The resulting initial-final mass relation roughly matches that in Cummings et al. (2016).

2.2.4 *Type Ia supernovae*

SNe Ia are essential for the chemical evolution of galaxies as they are a source of Fe-peak elements, with some contribution to α (see e.g., Seitenzahl et al. 2013; Kobayashi et al. 2020). Although their origin is still not fully understood, mass transfer to a degeneracy-supported object in a binary system seems ubiquitous to models, with a near-Chandrasekhar-mass white dwarf primary being the most favourable candidate (Bloom et al. 2012). Due to their uncertain origins, empirical models assuming delay-time distributions weighted by cosmic star formation histories are often used for modelling SNeIa rates (see e.g., Mannucci et al. 2006; Maoz et al. 2014; Maoz & Graur 2017).

Our model incorporates the field normalised delay-time distributions from Maoz & Graur (2017), giving a SNeIa rate per unit mass

$$n_{\rm Ia} = I_{\rm Ia} \left(\frac{t}{\rm Gyr} \right)^{-1.12} \Delta t, \quad t > t_{\rm Ia}, \tag{2}$$

assuming a delay time $t_{\rm Ia}$ = 38 Myr (main sequence lifetime of 8 M$_\odot$ star), and normalisation $I_{\rm Ia} = 2.6 \times 10^{-13}$ yr^{-1} M$_\odot^{-1}$. Because of the uncertainty regarding progenitor[6], as well as a missing tracer for binary stars in our model, we use the particles tracing the unresolved stellar component to determine possible locations of SNeIa. To compute the number of SNeIa, each star particle representing unresolved stars stores the total mass of coeval stars, and uses it to normalise $n_{\rm Ia}$

[6] Note that these rates do not assume a progenitor, however, our chemical yield model does. SNeIa yields from Seitenzahl et al. (2013) assumes a Chandrasekhar-mass delayed-detonation scenario.

for a given star particle age. This number ($\ll 1$) is used to determine the probability of an event, ultimately sampling discrete SNIa. Each explosion releases 10^{51} erg of energy and 1.4 $M_\odot$ of mass into its immediate surrounding.

Figure 2 summarises the feedback budget of our model, showing the cumulative mass, momentum, and energy which is injected into the surroundings of a 10^5 $M_\odot$ mono-age population of stars over 1 Gyr. With the exception of winds from OB-type stars, the onset of feedback from the different sources is determined by the main-sequence lifetime of the most massive star in the relevant population of stars. The range of timescales for this onset highlights the importance of including a multitude of feedback sources, as this affects both how star formation proceeds locally, and shapes the environment for subsequent feedback.

3 NUMERICAL SETUP AND MODEL IMPLEMENTATION

INFERNO is implemented in the adaptive-mesh-refinement (AMR) and N-body code Ramses (Teyssier 2002). Ramses evolves the gas by solving the fluid equations on a refinement grid with a second order unsplit Godunov method, assuming an ideal mono-atomic gas with an adiabatic index of 5/3. The code accounts for metallicity-dependent cooling, assuming collisional ionisation equilibrium, using the cooling functions by Sutherland & Dopita (1993) for gas temperatures of $10^{4-8.5}$ K, and rates from Rosen & Bregman (1995) for cooling at lower temperatures. Additionally, we apply a background field of ultra-violet radiation as a heating source using the redshift zero field from Haardt & Madau (1996), including a model for self-shielding in dense gas (Aubert & Teyssier 2010). The dynamics of stars and dark matter are tracked using collisionless particles, whose contribution to the gravitational potential is added to the AMR grid with the cloud-in-cell particle-mesh method. The forces are calculated by solving the Poisson equation with a multi-grid method (Guillet & Teyssier 2011). A quasi-Lagrangian refinement strategy ensures roughly 8 particles in each cell, which reduces discreteness effects (Romeo et al. 2008). Furthermore, cells are split into 8 new cells, using a refinement mass criterion of 800 $M_\odot$. We limit cell-splitting to 16 levels of refinement, providing a spatial resolution limit of $\sim$ 1.5 pc for our simulations, which are set up in a box with 100 kpc side length.

We employ INFERNO on a dwarf galaxy to study how efficiently stellar feedback drives outflows. The simulated galaxy is an analogue of the Wolf–Lundmark–Melotte (WLM) galaxy with a gas mass $M_{\rm g,disc} \approx 7 \times 10^7$ $M_\odot$, an initial stellar disc with mass $M_{\rm s,disc} = 10^7$ $M_\odot$ and a dark matter halo with mass $M_{\rm vir} = 10^{10}$ $M_\odot$. The latter two are comprised of 12.5 $M_\odot$ stellar particles and 1650 $M_\odot$ dark matter particles. We consider the initial stellar component only as a mass component (i.e. with no contribution to feedback or enrichment). The initial disc, comprised of gas and stars, has an exponential radial density profile with a scale length of 1.1 kpc. The vertical gas distribution is set in accordance with hydrostatic equilibrium at an initial temperature of 10^4 K, while the vertical distribution of stars is initialised with a Gaussian distribution with a scale height of 0.7 kpc. Initially, the gas disc has a metallicity of 0.1 $Z_\odot$. The dark matter profile matches a NFW profile (Navarro et al. 1996) with a spin parameter $\lambda = 0.04$ and concentration parameter $c = 15$. The ICs were generated using MakeDiscGalaxy (Springel 2005)) and mapped onto the AMR grid using the cloud-in-cell method. These generated ICs do not fill the full extent of our simulated box, hence cells without assigned properties are initialised with a density of 10^{-5} cm^{-3}, a metallicity of 0.001 $Z_\odot$, and a temperature of 3×10^4 K. These ICs are almost identical to those in Smith et al. (2021).

Since we do not consider feedback processes from the stars included in the ICs, the initial gas support is purely thermal. This energy support is quickly radiated away resulting in a sudden collapse and star formation burst, which is typical for galaxies simulated in isolated boxes. To mitigate this effect we start the simulation without gas cooling and then ramp it up exponentially (formally we scale the internal energy sink responsible for cooling by $(t/t_0)^5$, effectively re-scaling the cooling rate) over the first $t_0 = 100$ Myr. This method allows for a calm initialisation of the galaxy. We do not include this transient in any of our result figures.

The stellar feedback model injects energy, momentum, and chemically enriched material at each fine time step (i.e. between the time integration of each refinement level). For each injection we loop through all stars and assign the relevant feedback quantities into the local oct (8 neighbouring cells), updating the density, velocity, and pressure of each cell. If a star enters a new evolutionary stage during a timestep (which affects the feedback model), we adapt the calculation to only cover the part of the timestep during which stellar feedback is active. Furthermore, two safety criteria (a maximum advection velocity of 6000 km s^{-1}, and a maximum temperature of 10^9 K) are employed to ensure the stability of the hydrodynamics solver.

Because the resolution is limited (specifically in low-density gas by the AMR prescription) the momentum buildup in the quasi-energy-conserving stage of SNe explosions is not always captured. To handle this problem, we first calculate the radius $r_{\rm ST}$ of the blast-wave when it transitions from energy conserving to momentum conserving (i.e., from the Sedov-Taylor phase to the often called snowplough phase, Sedov 1959; Taylor 1950). If this radius is not resolved by at least 6 cells we inject the terminal momentum $p_{\rm ST}$ that would have built up during the energy conserving stage. We compute the cooling radius from $r_{\rm ST} = 30\, E_{51}^{7/17}\, \rho_{\rm g}^{-7/17}\, Z_{\rm g}^{-0.2}$ pc, where E_{51} is energy in units of 10^{51} erg, $\rho_{\rm g}$ is cell density in units cm^{-3}, and $Z_{\rm g}$ is metallicity in solar value. This follows from the analytical blast-wave solution (Blondin et al. 1998), to which we have added a metallicity scaling calibrated to our cooling function (Thornton et al. 1998). Similarity, the terminal momentum is calculated from $p_{\rm ST} = 2.95 \times 10^5\, E_{51}^{16/17}\, \rho_{\rm g}^{-2/17}\, Z_{\rm g}^{-0.2}$ $M_\odot$ km s^{-1}, where we have adjusted the scaling following Kim & Ostriker (2015). Roughly 5% of SNe are unresolved in our simulations.

4 RESULTS

As detailed in Section 1, the aims of this work are (i) verifying that INFERNO produces realistic ISM conditions for galaxy evolution, (ii) exploring the physics of outflows in a dwarf galaxy, and (iii) investigating how these outflows are affected by natal stellar kinematics. For the latter, we compare the results of 8 dwarf galaxy simulations with identical ICs, but with different natal velocity distributions. In addition, a ninth simulation (`no feedback`) serves as an example of not including stellar feedback. To maintain clarity, the main body of this work includes the detailed analysis of 4 simulations: 1) `no feedback`, with no energy or momentum injection from stellar feedback sources; 2) $\sigma_v = 0$, with neither `stir` or `kick` applied; 3) $\sigma_v = 0.01$ km s^{-1}, with `stir` applied; 4) $f_{\rm kick} = 0.2$, with $\sigma_v = 0.01$ km s^{-1} `stir` and `kick` applied. The full suite of simulations is shown in Appendix A, where we divided them into `stir` models ($f_{\rm kick} = 0$), and `kick` models ($f_{\rm kick} > 0$). The `no feedback` simulation have a $\sigma_v = 0.01$ km s^{-1} `stir` applied. The choice of $f_{\rm kick} = 0.2$ is motivated by the cluster escape fractions ranging from

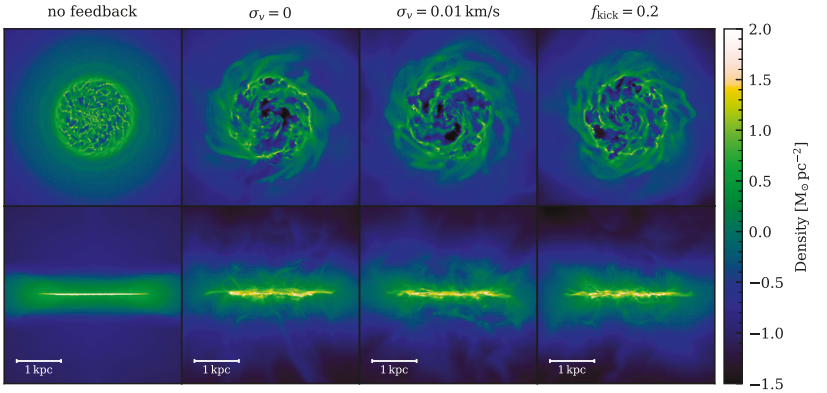

Figure 3. Projected gas density of the simulations studied in this work, shown in face-on projection on the top row and edge-on projection on the bottom. The snapshots shown are at t = 400 Myr, and all snapshots for a given simulation in the time-span 300 – 500 Myr are similar, with the exception of transient events, such as super-bubble outbreaks.

10 to 30% for massive stars, as found in Oh & Kroupa (2016). After the initial relaxation (200 Myr) we follow the evolution for 500 Myr, covering a few orbital times. Our analysis only concerns the final 500 Myr of evolution.

4.1 Effect on interstellar medium

With the exception of `no feedback`, the visual appearances of the gas properties in our simulations are similar (see e.g., gas density in Figure 3). For `no feedback`, the absence of energy and momentum sources results in a cold and fragmented disc. In contrast, the inclusion of stellar feedback significantly reduces the number of clouds and creates hot low-density voids in between the gaseous spiral structure. Furthermore, feedback drives gas out of the galaxy, generating a complex gas structure above and below the disc. This inner circumgalactic medium (CGM) is similar in all feedback models, regardless of the natal kick model. This is unlike those found in Steinwandel et al. (2022), as well as results for more massive systems, which have been shown to be strongly affected by the inclusion of runaway stars (Ceverino & Klypin 2009; Andersson et al. 2020, but see Kim & Ostriker 2018; Kim et al. 2020a). We discuss this further in Section 5.

Feedback leads to a lower star formation rate (SFR), quantified in Figure 4. At early times (t < 200 Myr), the lack of significant inflows causes the gas content to reduce over time, with an accompanying decrease in SFR in all simulations. For simulations including feedback, the SFR flattens after this period, as fountain flows are starting to regulate the supply of gas to the galaxy. In the first 300 Myr of these simulations, the total gas mass fraction $f_g = M_g/(M_g + M_\star)$ is reduced by $\sim$ 10%, while that of only cold ($T < 10^4$ K) gas is reduced by $\sim$ 20%. From this, it is clear that feedback reduces the amount of gas available for star formation, in part due to outflows which we focus on in Section 4.2. In the simulations including feedback, the SFR is compatible with that observed in the WLM galaxy ($\sim 6 \times 10^{-3}$ M$_\odot$ yr^{-1}, Karachentsev et al. 2013) at $\sim$ 200 Myr. The galaxies evolve with periodic variations in the SFR, on average lying below the observed rate by a factor of few after 200 Myr. The periodicity arise from bursts in stellar feedback act in response to the periods of high star formation. For example, in the case of $\sigma_v = 0.01$ km s^{-1}, a complete shutdown of SFR occurs between 430 and 470 Myr.

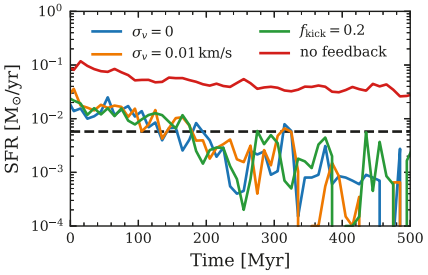

Figure 4. Star formation rate as a function of time for our simulations, computed by summing the stellar mass in 10 Myr age bins. The dashed horizontal line shows the observed star formation rate of WLM (Karachentsev et al. 2013). With the inclusion of stellar feedback, star formation is significantly reduced as a result of the loss of cold gas.

In addition to suppressing the SFR, stellar feedback generates an over-pressured hot phase in the ISM, and large low-density bubbles. Figure 5 shows this highly multi-phase gas structure of the disc (defined as a cylinder with a radius of 3.5 kpc and height of 1 kpc, as outlined with red lines in the right plots of Figure 7). The pressure P of simulations including feedback spans several orders of magnitude ($P/k_B \sim 1 - 10^6$ K cm^{-3} at $\rho = 1$ cm^{-3}, where k_B is the Boltzmann constant). The majority of high-pressure gas is generated by clustered feedback and the natal stellar velocity model plays only a minor role. The clustered nature stems from vigorous star formation in dense

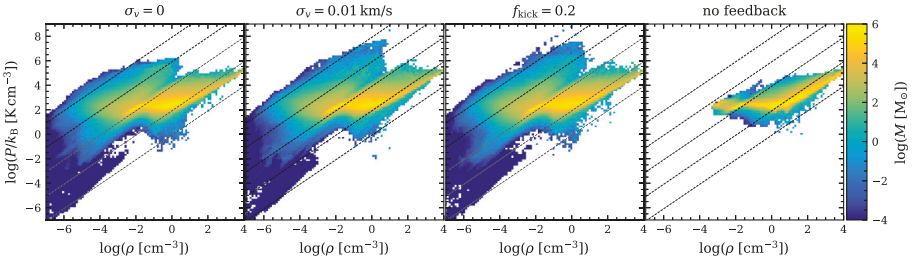

Figure 5. Pressure at different gas densities in the disc of our simulations (denoted by the title of each panel). These quantities are measured in each cell for all outputs and plotted as time-averaged (300 – 500 Myr), mass-weighted 2D-histogram. The dotted lines show temperatures 10^0, 10^2, 10^4, 10^6 and 10^8 K from bottom right to top left, computed from the ideal gas law.

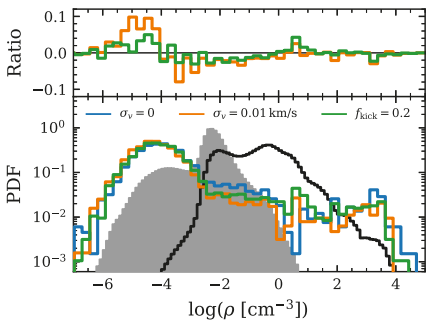

Figure 6. Probability distribution of gas density, showing volume (mass) weighted distributions for $f_{\rm kick} = 0.2$ in the filled grey histogram (thick black line), and coloured lines (different models labelled in legend) showing the distribution of densities where CCSNe exploded. Note that all models with feedback have similar volume and mass-weighted distributions. All results are taken as time-averages for the final 200 Myr of each run. The top inset show the ratio of the distributions between the two models including natal stellar velocities (distinguished by the same colour as in the bottom plot) and the $\sigma_v = 0$ model.

clouds, and proceeds until halted by the onset of the first CCSNe (6 Myr). Before this disruption of the star-forming clouds, the gas collapse is suppressed by stellar winds.

Figure 6 compares the average probability density function (PDF) of the gas densities for the simulations. For a given coeval stellar population, the first CCSNe typically explode in dense gas ($\rho \sim 10^4$ cm^{-3}), rapidly building up a low-density bubble ($10^{-6} < \rho < 10^{-3}$ cm^{-3}) for subsequent CCSNe. During the buildup of the bubble, CCSNe explode in intermediate gas densities ($10^{-2} \lesssim \rho \lesssim 10^2$ cm^{-3}). In the top panel, we show the ratio between the explosion densities of the two simulations including natal kinematic models and the $\sigma_v = 0$ model. Surprisingly, $\sigma_v = 0.01$ km s^{-1} deviates the most from $\sigma_v = 0$ (clearly visible at $\rho = 10^{-5}$ cm^{-3}), although the difference is small and subject to stochasticity between measurements. The minor role of runaway stars in determining the explosion density distribution is due to their rarity in comparison to non-runaway stars. For our galaxy, the effect that stellar feedback has on the gas dynamics is completely dominated by the clustered CCSNe. This is apparent in the outflows, which we explore in the following section.

4.2 Outflows and inner CGM

The energy supplied by our feedback model translates into a galactic wind, resulting in large amounts of gas being pushed out of the galaxy. Significant amounts of gas return in galaxy scale fountain flows, while the rest is accelerated to outflow velocities $v_{\rm out}$ exceeding the escape velocity $v_{\rm esc}$ (described in more detail in Section 4.3). Here we explore the interplay between the outflowing gas and the inner parts of the CGM, focusing on the final 200 Myr of the simulations. We no longer consider any results from the `no feedback` model, due to its inability to generate outflows.

We measure the properties of outflowing gas at two interfaces located outside the galaxy. Their location (white filled) and extent (white dotted) is displayed on top of projected density maps of the $f_{\rm kick} = 0.2$ simulation in Figure 7. We refer to the interface located close to the disc as *launching*, and the spherical shell interface, which encapsulates the inner CGM, as *inner-outer halo*. Note that these definitions vary in the literature, and that outflow properties can depend on how these are defined. We measure the properties of the outflowing gas by summing a quantity q multiplied by the gas velocity v, considering only cells with outward moving gas within a given region.[7] Variables indexed by i refer to their value in individual cells. For the *launching* interface, this is formally calculated following

$$\frac{{\rm d}q_z}{{\rm d}t} = \frac{1}{\Delta z} \sum_i q_i \, |v_{z,i}|, \text{ for } \begin{cases} v_{z,i} > 0, \text{ if } z_i > 0 \\ v_{z,i} < 0, \text{ if } z_i < 0 \end{cases}, \quad (3)$$

where the sum runs over cells (i) in a cylindrical slab with thickness

[7] In this work we mainly consider mass m_i, metal mass $Z_i m_i$, and total energy $m_i\,(v_i^2/2 + c_{s,i}^2/(\gamma - 1))$ outflows, substituting q_i with these terms when applicable. Throughout the paper, we take Z_i to be the metal mass fraction, c_s to be thermal sound speed, and $\gamma = 5/3$ to be the adiabatic index. Note that kinetic energy refers to the first term in the total energy sum, while the second term is thermal energy.

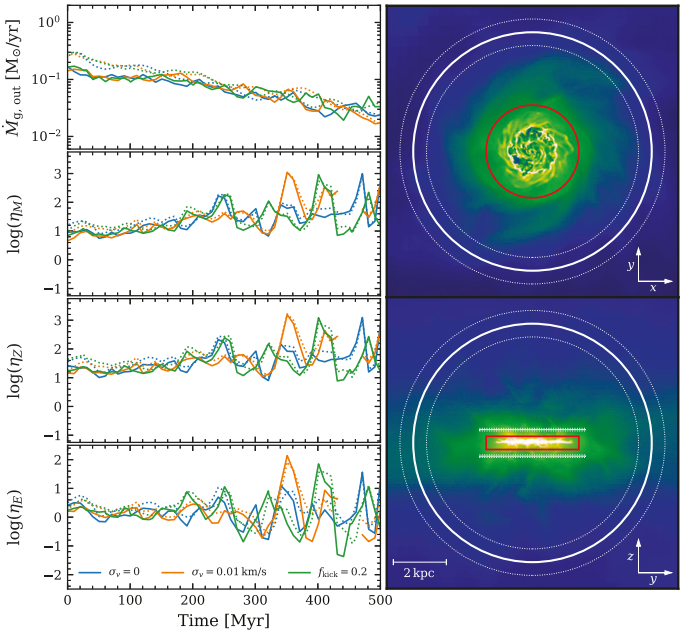

Figure 7. *Left:* Mass outflow rate (top) and loading factor of mass (top centre), metal (bottom centre) and energy (bottom) as a function of time for the simulations including feedback with different natal kinematic models as labelled by the legend in the bottom plot. The filled (dotted) lines show measurements through the *launching* (*inner-outer halo*) interface. *Right:* Projected gas density of the $f_{kick} = 0.2$ simulation in a 22 kpc view, displaying the placement of the *launching* and *inner-outer halo* interfaces (white filled and dotted lines). Material encapsulated by the red lines is considered disc material. The colourbar is similar to that of Figure 3, but with limits $[-2.5, 1]$ M$_\odot$ pc^{-2} to better display to lower density gas in the CGM.

$\Delta z = 0.1$ kpc placed ± 1 kpc from the disc mid-plane. For the *inner-outer halo* interface, we use

$$\frac{dq_r}{dt} = \frac{1}{\Delta r} \sum_i q_i \, v_{r,i}, \text{ for } v_{r,i} = \mathbf{v}_i \cdot \hat{\mathbf{r}} > 0 \tag{4}$$

where the sum runs over cells in a spherical shell with a radius of 9 kpc (roughly equal to 20% of the virial radius) and a thickness $\Delta r = 2$ kpc. The coordinate system has its origin at the centre of the galaxy and its directions are indicated in the density maps to the right in Figure 7. In Equation 4, $\mathbf{v}_i$ is the velocity vector, and $\hat{\mathbf{r}}$ is the radial unit vector.

The top left plot in Figure 7 shows the mass outflow rate as a function of time[8]. The remaining three left plots show the time evolution of the logarithm of mass, metal and energy loading factors, which we define as

$$\eta_M = \frac{\dot{M}_g}{\text{SFR}}, \quad \eta_Z = \frac{\dot{M}_Z}{Z_g \cdot \text{SFR}}, \quad \eta_E = \frac{\dot{E}}{\xi_{SN} \cdot \text{SFR}} \tag{5}$$

respectively, where Z_g is the gas metallicity of the disc, and $\xi_{SN} = 4.89 \times 10^5$ km^2 s^{-2} is the average energy injected by CCSNe from stellar populations with a fully sampled Kroupa (2001) IMF assuming 10^{51} erg per CCSNe (c.f., Kim & Ostriker 2017; Smith et al. 2021).

The gas mass ejected in outflows exceeds the mass consumed in star formation by up to two orders of magnitude. This is the case for all three models, which all show outflow rates of similar average values. Furthermore, the values are similar both at the *launching* and the *inner-outer halo* interfaces. As noted in the previous paragraph, wind properties are in general sensitive to where they are measured and here their similar values are coincidental, as the vertical placement of the *launching* interface affects the value measured. Surprisingly, this is not the case for the *inner-outer halo* which we discuss in more detail in Section 4.3.

The mass loading factor increases in the first 200 Myr, and then reach values that fluctuate between $\sim 10 - 1000$, independently of the natal stellar velocity model. This is also the case for the metal loading factor, although its value slightly exceeds η_M. The energy

[8] There is some ambiguity in how one defines the vertical outflows, and in our case, we chose to compute the outflows in the two slabs independently and then sum them. For modelling purposes, the total outflow through both slabs is most useful, as it captures the mass loss from the disc. Observationally, the outflow measurements are typically limited to a single cone and then multiplied by a factor of two (assuming symmetry), in order to capture the total outflow rate (see, e.g., Schroetter et al. 2019). We find little to no difference between the two slabs, justifying this assumption.

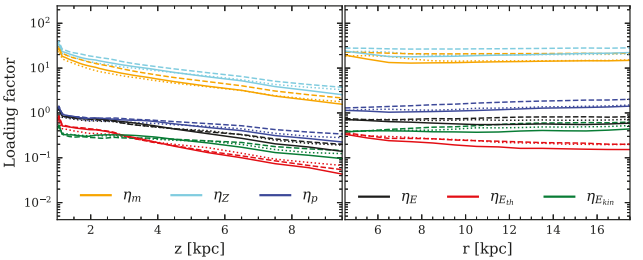

Figure 8. Loading factors of mass (orange), metal (cyan), momentum (blue), total energy (black), thermal energy (red) and kinetic energy (green) as a function of vertical distance to the left and radial distance to the right. We measure vertical outflow using slabs of the same size as that in Figure 7 but increasing the thickness to 1 kpc above 4 kpc. Radial outflows are measured as in Figure 7, but for different radii. The lines show the mean value of all outputs in the last 200 Myr (see text for details). $f_{\rm kick} = 0.2$ is shown by the filled lines, while the thin dotted (dashed) lines shows the results for $\sigma_v = 0$ ($\sigma_v = 0.01$ km s^{-1}).

loading factors do not show an initial increase but display similar fluctuations around the same time. As with the other loading factors, these fluctuations grow significantly stronger at later times, resulting in values of η_E in the range $\sim 0.1 - 100$. These fluctuations are the result of variations in SFR, and the outflow properties remain more stable (see e.g. mass outflow rate in the top left plot of Figure 7).

In a broader context, high mass loading factor ($10 - 100$) for low mass galaxies are typically required by semi-analytical models (see e.g., Benson et al. 2003; Somerville & Davé 2015) and large volume simulations to match observed galaxy scaling relations (e.g, Mitchell et al. 2020). Metal loading factors are typically found to be of the same order or in excess of the mass loading factor (Yates et al. 2021), as we also find here. INFERNO captures these heavily mass and metal-loaded winds without fine-tuning any feedback parameters. Comparisons of energy loading factors are more difficult since these depend strongly on the details of the feedback model, as well as the cooling and structure of the CGM. In our case, the absence of a cosmological environment, and η_E around unity gives rise to a CGM with total energy set by the stellar feedback budget. Compared to studies of outflows with similar feedback model and galaxy (e.g., Smith et al. 2021; Steinwandel et al. 2022) our values of η_E are high, which we discuss further in Section 5.1. Our loading factors roughly match those in observed galaxies (Chisholm et al. 2017, 2018), although it should be noted that completeness issues and differences in the geometrical definition of where outflows are measured make loading factors notoriously difficult to estimate, in particular for dwarf galaxies (see Collins & Read 2022, for a review). For mass and energy loading, Chisholm et al. (2017) accounts only for the photo-ionized gas, which does not necessarily capture the entire outflow (a notion returned to later). Furthermore, because of the strong temporal fluctuations we find in our simulation, a better comparison would be to investigate if the range of loading factors in our simulations matches the scatter in observations. However, such a comparison would necessitate more observational data points for the galaxy mass range we consider.

4.3 Time-averaged wind properties

We now turn to time-averaged properties of the outflows, considering only the final 200 Myr of each simulation. Note that for loading factors (see Equation 5) we consider the fraction of the mean of the numerator and denominator separately, rather than the mean of the loading factor itself. This alleviates the problem with ill-defined loading factors when the denominator is zero. Furthermore, we do not account for the scatter in SFR, but only consider that of the outflow. A similar approach is sometimes used in the literature when quoting loading factors resolved in time (see e.g., Hislop et al. 2021; Steinwandel et al. 2022)

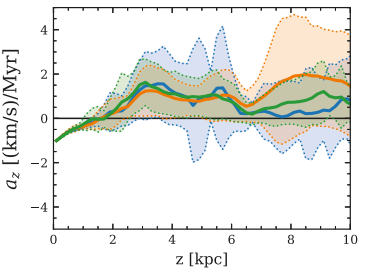

Figure 9. Vertical profile of gas acceleration in the CGM for the simulations, computed from the pressure gradient and an analytical approximation of the gravitational potential of each galaxy. The filled lines show the mean acceleration from all outputs in the final 200 Myr, with the shaded regions showing the standard deviation.

Figure 8 shows the average loading factors as function of vertical distance (left) and radius (right). In addition to mass, metal and energy loading factor we also include momentum loading factor[9], as well as the energy loading factor split into thermal and kinetic energy. As previously mentioned, we see that while the vertical profile decreases with distance, the radial remains roughly constant. The decrease in vertical loading factors comes from the cylindrical slabs with a constant radius being unable to capture the full extent of the conical outflow, as these slabs are moved out. The outflow transition from thermally dominated to kinetically dominated around $z = 3$ kpc

[9] Momentum loading factor is measured by dividing $\dot{p}$ (computed from Equations 3 & 4, with $q_i = m_i v_i$) by the product of star formation rate and $1.25 \times 10^5 / 95.5$ km s^{-1}. See Kim et al. (2020b) for details on the normalization.

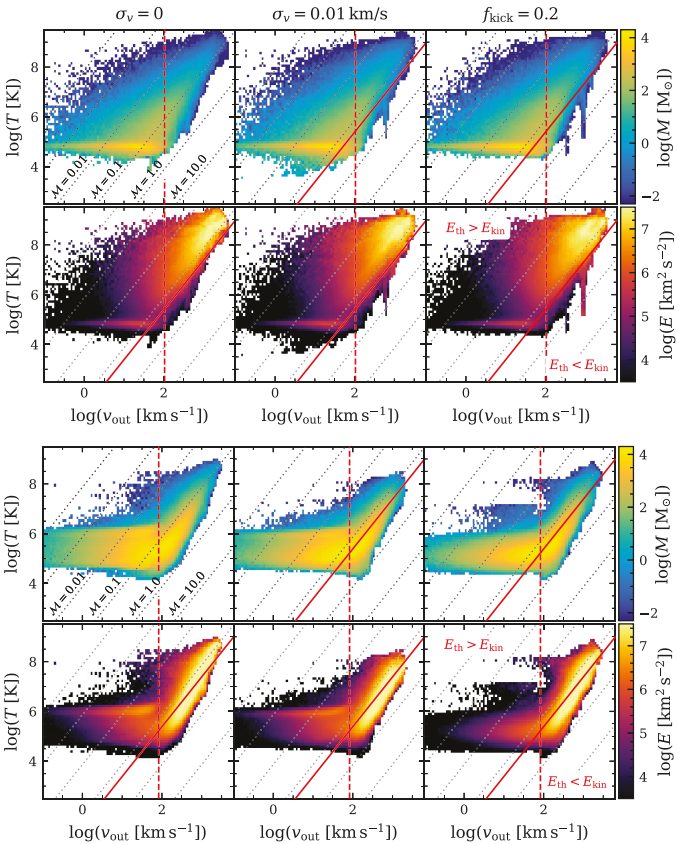

Figure 10. Temperature-velocity diagrams for outflowing gas shown for the *launching* (*inner-outer halo*) interface in the top (bottom) two rows. We weigh the maps by mass or specific energy, as indicated by the colourbar on the right-hand side of each row. Each panel shows the time average of the 2D-histograms for all outputs in the last 200 Myr. Each column shows the simulation indicated by the column title. The dotted black lines draws order of magnitude Mach numbers ($\mathcal{M} = v_{\rm out}/c_{\rm s}$) calculated from the adiabatic sound speed ($T = m_{\rm H}\, c_{\rm s}^2/(k_{\rm B}\gamma)$, with $\gamma = 5/3$). Solid red lines indicate where the kinetic ($0.5v^2$) and thermal ($2.5P/\rho$) energy of the outflowing gas is equivalent. The red dashed line shows the escape velocity of the dark matter halo at the location of the interface.

in all simulations. This is not only the result of gas cooling but also gas acceleration (seen as an increase in momentum loading). The acceleration arises due to pressure gradients existing in the halo, shown in Figure 9. We compute this by taking the gradient of the pressure profile and subtracting the gravitational force from an analytical NFW profile (Navarro et al. 1996, the disc has negligible contribution to the potential outside 2 kpc). We find that the acceleration becomes positive around 2 kpc, and flattens at a value of 1 km s^{-1} Myr^{-1} around 3 kpc. The flattening coincides with the transition between thermally and kinetically dominated gas energy. Provided that the acceleration can proceed far out in the halo, it can accelerate gas to 100 km s^{-1} in 100 Myr. As already indicated by the similarity in mass outflow rate (Figure 7), there is little difference between the models. Furthermore, this affects the velocity structure of the gas between the *launching* and *inner-outer halo* interfaces, described below.

Figure 10 shows the velocity and temperature structure of the outflows. The figure is divided into two sets of subplots, the two rows on top show the *launching* interface, while the two bottom rows show the *inner-outer halo* interface. In the *launching* interface, we find that outflows with temperature $T \lesssim 10^5$ K dominate the mass budget (first row), while hotter outflows dominate the energy budget (second row). The majority of the mass resides in gas with temperatures $T \lesssim 10^5$ K, with velocities up to around 100 km s^{-1}.

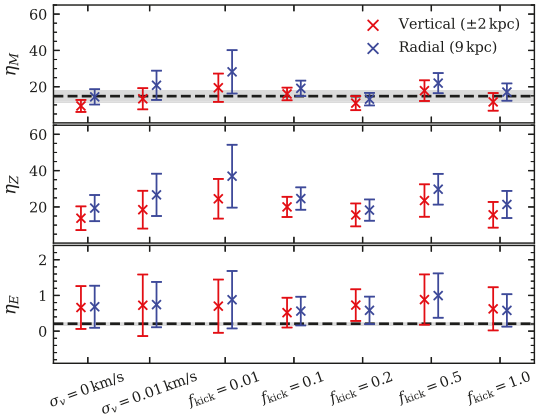

Figure 11. Mean and standard deviation of mass (top), metal (centre) and energy (bottom) loading factors taken over the last 200 Myr of all our simulations. Red markers show the loading factors as measured at the *launching* interface, while blue points show that measured at the *inner-outer halo* interface. Note that all models including some fraction of stars with the walkaway and runaway velocity distribution ($f_{\rm kick} \neq 0$) also imposes the $\sigma = 0.01$ km s^{-1} distribution on stars which are not kicked. The black dashed line (errors indicated by grey region) shows the value from the empirical fitting function of Chisholm et al. (2017).

Above 100 km s^{-1}, the temperature of the gas increases along a trend of roughly constant Mach number $\mathcal{M} = 0.1$. This increase roughly coincides with the escape velocity of the dark matter halo. For the *launching* interface, this trend only includes a small fraction of mass. At the peak of the trend, we find most of the energy, at temperatures around few $\sim 10^8$ K and velocities $\gtrsim$1000 km s^{-1}. This is in broad agreement with Kim et al. (2020b), who find a similar dichotomy in cold and hot gas when comparing the mass and energy budget of these different phases. Notably, Kim et al. (2020b) found the hot medium to reach supersonic speeds, which is in contrast to the exclusively subsonic flows in our simulations. The subsonic nature of the outflows stems from the efficient heating of halo gas, discussed in Section 5.2.3.

When the gas reaches the *inner-outer halo*, more mass has been entrained into the fast and hot phase of the wind. We also see that the energy has made the transition from thermal to kinetic (the transition is indicated by the filled black line in Figure 10). The trend along a constant Mach number appears clearly, in particular in energy-weighted velocity-temperature space. As in the *launching* interface, the gas is limited to subsonic velocities.

Finally, we summarise the mass, metal and energy loading factor for all simulations in Figure 11, including those presented in Appendix A. The mass and energy loading factors of all our simulations are comparable to the values from empirically derived fitting functions by Chisholm et al. (2017), shown with black dashed lines. A similar fitting function for metal loading factor is presented in Chisholm et al. (2018), however, our values underestimate these by 2 orders of magnitude, hence we omit including these estimates on the linear vertical axis of Figure 11. We do not find large differences among our simulations, but rather that all simulations have $\eta_M \sim 5-40$, $\eta_Z \sim 10-60$ and $\eta_E \sim 0-2$. The largest value and scatter are found in $\sigma_v = 1$ km s^{-1}, and in $f_{\rm kick} = 0.5$ when including walkaway and runaway stars. The minor role of runaway stars is likely a result of highly porous ISM, as well as a halo which is highly energetic. We discuss this and other factors which might affect the small role of runaway stars in Section 5.2.

5 DISCUSSION

The results covered have been focused on the INFERNO model's ability to regulate star formation and drive galactic scale outflows via stellar feedback. For a dwarf galaxy, our model generates a strong steady outflow, with large (> 10) mass and metal loading factors, as well as the energy loading factor close to unity (summarised in Figure 11). When resolved in time, we find that the loading factors display strong fluctuations (two orders of magnitude) as a result of bursty SFR. High loading factors on the dwarf mass scale are necessary to reproduce the faint end of the galaxy mass function (Naab & Ostriker 2017), a notion that is also supported empirically (Chisholm et al. 2017, 2018; Schroetter et al. 2019). The outflows are more metal-rich compared to the ISM, however, not to the extent found by Chisholm et al. (2018). We investigate this further in Andersson et al. (*in prep.*), where we present the full chemical evolution model implemented in INFERNO. Our outflows are highly multi-phase in nature, covering a large range of temperatures. This is crucial for the degree of ionisation in the CGM (Tumlinson et al. 2017). In stark contrast to previous results obtained for massive disc galaxies (Andersson et al. 2020), we find that the natal velocity distribution of the stars plays a minor role in setting the loading factor on dwarf scales. In the following sections, we discuss this in more detail.

5.1 Comparisons with contemporary feedback models

Our simulation setup of a dwarf galaxy in an isolated environment allows us to reach parsec scale resolution, which is comparable to works by e.g. Hu (2019); Emerick et al. (2020); Smith et al. (2021);

Steinwandel et al. (2022). While the initial gas mass of these models varies (particularly in Emerick et al., who simulated an ultra-faint dwarf), the mass and metal loading factor are in broad agreement. However, the energy loading factor of our simulations is around unity, while the aforementioned works routinely find values around 0.1. As discussed below, this discrepancy by an order of magnitude could provide insight into differences in feedback models and numerical treatment. The energy supplied to the halo affects the re-accretion of material, dividing feedback into *preventive* (inhibiting gas inflow) and *ejective* (expelling gas) feedback (Davé et al. 2012). For a thorough literature comparison, we refer to Li & Bryan (2020).

Of particular interest is the work by Smith et al. (2021, see also Smith 2021). Smith et al. investigated a suit of simulation with similar ICs and numerical resolution, but with a different hydrodynamics solver, star formation recipe, and for a range of different feedback sources (see also Hu 2019). Their SN-PE model is the most comparable model in terms of included feedback processes (although we include SNIa and stellar winds which may be of importance, see Section 5.2.2), with which we find slightly lower mass loading (factor 2), but a significantly higher energy loading (factor 10). We note that when Smith et al. introduces radiation feedback, the energy loading decreases significantly, thereby increasing the discrepancy with our model.

The discrepancy could be the result of fundamentally different hydrodynamics methods, i.e., their particle-based scheme (Lagrangian) compared to our grid-based scheme (Eulerian). Two possible explanations are the different treatments of shock heating in the halo and star formation in dense clouds. Concerning the former, the difference between methods arises mainly in low gas density environments, e.g. in the halo. Because low-density gas is inherently traced by a low number of particles, it is not clear how well Lagrangian methods treat chocks in these environments. This is particularly interesting concerning runaway stars which leave the disc, discussed further in Section 5.2.3. Concerning the star formation in dense clouds, Lagrangian methods typically find density distributions which extend to higher densities[10], resulting in shorter free-fall times for star formation (see Equation 1). We could increase the star formation efficiency to account for this, which increases the clustering of SNe as a result of denser star clusters (Hu et al. 2022). This difference likely need to be accounted for when comparing models with similar star formation recipe but different hydrodynamical solver. Note that Smith et al. (2021) explored this and concluded that their results were insensitive to this, although this is not clear for our model. Likely, the numerical method plays other roles as well, a factor which has been discussed extensively in literature (see, e.g., Kim et al. 2014, 2016; Roca-Fàbrega et al. 2020).

A limitation of the INFERNO model is the lack of radiation feedback. With the ability to reduce the clustering of star formation (see e.g. Hislop et al. 2021), radiation feedback typically limits loading factors, in particular in energy (Smith et al. 2021). Furthermore, Agertz et al. (2020) showed that radiative feedback has a strong effect on the formation of ultra-faint dwarf galaxies, with a significant suppression in SFRs, leading to an overall calmer evolution. Our model does not yet include radiation feedback, although stellar winds play a similar role (Andersson et al., in preparation).

[10] In contrast to Eularian formalism with particle-mesh gravity solver, particle-based hydrodynamics does not strictly require the smoothing length (set by particle neighbour search) to be that of the gravitational softening length. Unless carefully treated, this implies that densities can have spurious fluctuations on scales below the formal resolution. However, limiting the smallest smoothing length can result in an extremely costly neighbour search. The equivalent in our method is extremely deep refinement. Although the basic hydrodynamics are formally the same at the identical resolution, the effect of this fundamental difference in method is highly non-trivial (Tasker et al. 2008; Hu et al. 2022)

5.2 The weak impact of natal stellar kinematics on stellar feedback

5.2.1 The role of disc structure and the ISM

As previously mentioned, the density structure of the ISM likely plays a role in how relevant runaway stars are. In Andersson et al. (2020), the inclusion of runaway stars resulted in a supply of CCSNe progenitors into large under-dense regions which enabled SNe to more efficiently drive outflows (Ohlin et al. 2019). This could also explain the disagreement found by Kim et al. (2020b), which does not capture the low-density regions imparted by spiral arm shearing and the full geometrical extent of the galaxy (see also Martizzi et al. 2016). In the simulations presented here, the low SFR implies that the number of runaway stars is low, hence, although low-density regions develop, they are unlikely to receive a significant number of runaway stars before dissolving. We confirmed this through visual inspection of our simulations.

Furthermore, the shallow potential of the disc in the dwarf galaxy implies a thick gas disc (initial scale height $h_{\rm disc} = 0.7$ kpc). As such, stars need to travel a long distance to reach dramatically different environment, even when travelling vertically (unless reaching far out in the CGM, see Section 5.2.3). In contrast, runaway stars in more massive disc galaxies (e.g. as in Andersson et al. 2020 with a gas disc scale height of $h_{\rm disc} = 0.34$ kpc) have a shorter travel distance to environments with as dramatic differences (e.g. in gas density).

The weak impact of runaway stars could be connected to the star formation threshold (500 cm^{-3}). Such a high density implies that star formation depletes the local gas reservoir on a timescale $\tau_{\rm dep} = \rho_g / \dot{\rho}_{\rm sf} = t_{\rm ff}/\epsilon_{\rm ff} \simeq 20$ Myr, which is similar to the timescale for SNe. Varying the star formation threshold and $\epsilon_{\rm ff}$ affects the clustering of SNe and to some extent the outflow properties (Smith et al. 2021). If gas is depleted fast, massive stars in clusters explode as SNe in low-density gas, leading to efficient heating of the ISM (e.g., Agertz & Kravtsov 2015). Differences in star formation recipes (as well as numerical resolution, see discussion in Kim et al. 2020a) could be the cause for the discrepancy in the results of e.g., this work, Kim & Ostriker (2018), Andersson et al. (2020), and Steinwandel et al. (2022). This would explain the lack of consensus regarding the impact of runaway stars. However, the full explanation is likely more intricate, with many factors playing a role, e.g. overall structure of the ISM (which determines escape channels for SNe energy, see e.g., Hayward & Hopkins 2017; Ohlin et al. 2019), or pre-SNe feedback (which can counteract gas collapse, see e.g., Smith et al. 2021).

5.2.2 The role of type Ia supernovae

A key aspect of the supposed effect that massive runaway stars have on stellar feedback is that they explode far away from where they were formed. This leads to more randomly distributed SNe sites, in contrast to SNe only around star-forming gas (see, e.g., Li et al. 2015, 2017). To a large extent, this is also the case for delayed SNe, e.g. SNeIa with rates which are a few tens of per cent of the CCSNe (Tammann et al. 1994). Exploring the role of these SNe in the context of dwarf galaxies warrants follow-up work, but we can speculate on their effect since our model implements a method to include these objects. Note that at late times in our simulations (final 200 Myr),

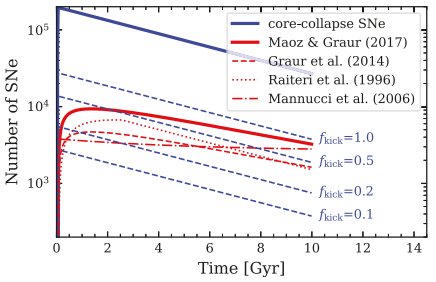

Figure 12. Number of CCSNe (blue) and SNeIa (red) as a function of time calculated for an exponential star formation rate. The dashed blue lines show the number of CCSNe related to runaway stars, assuming different cluster escape fractions $f_{\rm kick}$ (= 1 implies 14% runaway stars), labelled in the figure. The different red lines show SNeIa rates for different models widely used in the literature. The filled red line is the one used in our simulation.

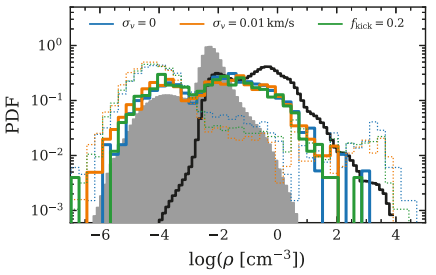

Figure 13. The probability distribution function of density, with coloured lines showing the densities where SNeIa explodes in our simulations. As in Figure 6, the filled grey histogram (thick black line) shows the volume (mass) weighted density distribution for the $f_{\rm kick}$ = 0.2 model. For comparison, we included the distribution of CCSNe with thin dotted lines. Note that the densities are sampled at different cadences; Ia densities are recorded at the time of the explosion, while the mass- and volume-weighted densities are computed at the 10 Myr output rate.

SNe Ia makes up ∼ 20% of the total SNe population. With only a small per cent of stars being runaways, SNe Ia may in fact be the main contributor to randomly located stellar explosions. To quantify this, we show the number of CCSNe and SNeIa in Figure 12, assuming an exponential SFR = $\exp -t/5$ Gyr $\mathrm{M}_\odot$ yr^{-1}. Also shown is the number CCSNe associated with runaway stars for different values of $f_{\rm kick}$, as well as several different models for the SNIa rate. In our simulations, we adopt the model by Maoz & Graur (2017). The second model shown is from Graur et al. (2014), which is the same as Maoz & Graur (2017) but normalized to fit data from galaxy clusters (half the rate of field galaxies). The model by Raiteri et al. (1996) has been widely used in early galaxy models (see e.g., Greggio & Renzini 1983; Matteucci & Greggio 1986; Agertz et al. 2013). We also show the the model derived by Mannucci et al. (2006) used in the FIRE2 model for galaxy simulations (Hopkins et al. 2014, 2018; Gandhi et al. 2022).

The SNIa rate builds up in the first few Gyr, and is comparable to the number of SNe associated with runaway stars even in models assuming a high fraction of kicked stars ($f_{\rm kick} \geq 0.5$). To our best knowledge, the role that this build-up of SNe Ia has on non-cosmological simulations is not well explored in the literature.

We show the gas densities where SNeIa explodes in Figure 13. Interestingly, we find that the density distribution of SNeIa explosions is a combination of the mass- and volume-weighted density PDF. If distributed homogeneously, one expects this distribution to follow the volume-weighted one. Nonetheless, we find the Ia explosions to extend toward higher densities. Furthermore, we find no correlation between the age of the star particle when the Ia occurs and the explosion density, implying that even early Ia are no longer associated with any particular density.

If SNe Ia affects the role of runaway stars, this might explain some of the discrepancies between our results and those of e.g. Smith et al. (2021); Steinwandel et al. (2022).

5.2.3 *CGM and out-of-disc runaway stars*

Steinwandel et al. (2022) finds that *out-of-disc* runaway stars can supply a significant amount of energy, thereby increasing the energy loading in simulations that include runaway stars. We do not find this to be the case in our simulations, despite us studying a galaxy of similar mass, and we see runaway stars escaping into the halo (see Figure A3). It is likely that the high energy-loading of all our simulations creates an environment around the galaxy which makes additional thermal energy dumps negligible. Indeed, in the case of $f_{\rm kick}$ = 0.2, the CGM inside the *inner-outer halo* interface contains $\sim 400 \times 10^{51}$ erg of thermal energy throughout its later evolution, i.e. hundred times larger than what any single SNe would provide. Compared to this highly energy-loaded halo, *out-of-disc* runaway stars only supply a small amount of energy (we find only ∼ 40 SNe 200 pc above the disc in the final 200 Myr of our $f_{\rm kick}$ = 0.2 simulation).

Another aspect of such a high thermal energy content is that this establishes a negative pressure gradient. As shown in Section 4.3, this results in an outward acceleration of significant amounts of gas ejected from the galaxy. Furthermore, it is likely that material is accelerated to high velocities by SNe blast waves (1000 km s^{-1}) that break out from the disc. The details of this will be explored in future work.

6 SUMMARY & CONCLUSIONS

We present a new galaxy physics model called INFERNO, introducing a star-by-star treatment for the injection of momentum, energy and chemically enriched material, each with timing, locality and amount calculated based on the properties of individual stars. We employ INFERNO to simulate the evolution of a dwarf galaxy to study how stellar feedback drives outflows. Our results focus on the mass, metal and energy loading factors, as well as the properties of galactic winds.

We draw the following concluding remarks from our study:

(i) Our stellar feedback model causes a lowering of star formation by roughly two orders of magnitude while driving strong gas outflows. A galactic wind is established close to the disc (around ±2 kpc from the disc mid-plane) and moves material through the CGM. We recover mass and metal loading factors on the order of 10 − 100, as

required to match the faint end of the galaxy mass function (Naab & Ostriker 2017). Furthermore, the wind is heavily energy-loaded, with an energy loading factor close to unity.

(ii) The galactic winds display a clear dichotomy in the mass and energy outflow, with mass primarily carried by cold gas ($T \simeq 10^5$ K) at velocities $v < 100$ km s^{-1}, while energy is carried in a hot ($T > 10^7$ K), fast ($v > 100$ km s^{-1}) wind. The energy evolves with distance from the galaxy, transitioning from thermally dominated to kinetically dominated a few kpc above the disc plane. Our model generates a highly energetic CGM where outflows are limited to the subsonic regime, with high-velocity gas ($v > 100$ km s^{-1}) following a trend of roughly constant Mach number $\mathcal{M} \sim 0.1$ in the velocity-temperature space.

(iii) We find no strong effects imposed by the different natal velocity distribution applied to newly formed stars. While we include runaway stars in our model, we find a surprising insensitivity to their presence, in stark contrast to more massive galaxies where runaway stars play a significant role in setting the outflows (Andersson et al. 2020). Not only is this the case for outflows ejected by dwarfs, but we find similar SFRs, gas multi-phase structures and SNe explosion densities, regardless of what natal stellar velocity distribution we apply.

The precise role played by runaway stars for galaxy evolution is not yet established, with varying conclusions in the literature (Ceverino & Klypin 2009; Kimm & Cen 2014; Andersson et al. 2020; Kim et al. 2020b; Steinwandel et al. 2022). At this stage, the literature covers a wide range of galaxy masses, which are simulated with a multitude of different models. This work is the first in a series which will employ INFERNO, with the aim of exploring runaway stars, as well as galaxy evolution physics in general.

ACKNOWLEDGEMENTS

EA thanks Ulrich Steinwandel for insightful conversations. EA, OA and FR acknowledge financial support from the Knut and Alice Wallenberg Foundation and the Swedish Research Council (grant 2019-04659). EA acknowledges financial support from the Royal Physiographic Society of Lund. EA acknowledge computer resources from Swedish National Infrastructure for Computing (projects SNIC 2021/5-111, SNIC 2021/6-87 and SNIC 2021/6-85) and Large Unified Modern Infrastructure (LUMI pilot phase).

DATA AVAILABILITY

The data underlying this article will be shared on reasonable request to the corresponding author.

REFERENCES

Agertz O., Kravtsov A. V., 2015, ApJ, 804, 18
Agertz O., Kravtsov A. V., Leitner S. N., Gnedin N. Y., 2013, ApJ, 770, 25
Agertz O., et al., 2020, MNRAS, 491, 1656
Alongi M., Bertelli G., Bressan A., Chiosi C., Fagotto F., Greggio L., Nasi E., 1993, A&AS, 97, 851
Andersson E. P., Agertz O., Renaud F., 2020, MNRAS, 494, 3328
Andersson E. P., Renaud F., Agertz O., 2021, MNRAS, 502, L29
Asplund M., Grevesse N., Sauval A. J., Scott P., 2009, ARA&A, 47, 481
Aubert D., Teyssier R., 2010, ApJ, 724, 244
Baugh C. M., 2006, Reports on Progress in Physics, 69, 3101
Behroozi P., Wechsler R. H., Hearin A. P., Conroy C., 2019, MNRAS, 488, 3143
Benson A. J., 2010, Phys. Rep., 495, 33
Benson A. J., Bower R. G., Frenk C. S., Lacey C. G., Baugh C. M., Cole S., 2003, ApJ, 599, 38
Bertelli G., Bressan A., Chiosi C., Fagotto F., Nasi E., 1994, A&AS, 106, 275
Blaauw A., 1961, Bulletin of the Astronomical Institutes of the Netherlands, 15, 265
Blondin J. M., Wright E. B., Borkowski K. J., Reynolds S. P., 1998, ApJ, 500, 342
Bloom J. S., et al., 2012, ApJ, 744, L17
Bressan A., Fagotto F., Bertelli G., Chiosi C., 1993, A&AS, 100, 647
Buck T., Rybizki J., Buder S., Obreja A., Macciò A. V., Pfrommer C., Steinmetz M., Ness M., 2021, MNRAS, 508, 3365
Ceverino D., Klypin A., 2009, ApJ, 695, 292
Chisholm J., Tremonti C. A., Leitherer C., Chen Y., 2017, MNRAS, 469, 4831
Chisholm J., Tremonti C., Leitherer C., 2018, MNRAS, 481, 1690
Collins M. L. M., Read J. I., 2022, Nature Astronomy, 6, 647
Cummings J. D., Kalirai J. S., Tremblay P. E., Ramirez-Ruiz E., 2016, ApJ, 818, 84
Dale J. E., Bonnell I. A., 2008, MNRAS, 391, 2
Dashyan G., Dubois Y., 2020, A&A, 638, A123
Davé R., Finlator K., Oppenheimer B. D., 2012, MNRAS, 421, 98
Dekel A., Silk J., 1986, ApJ, 303, 39
Doherty C. L., Gil-Pons P., Siess L., Lattanzio J. C., 2017, Publ. Astron. Soc. Australia, 34, e056
Drew J. E., Monguió M., Wright N. J., 2021, MNRAS, 508, 4952
Eldridge J. J., Langer N., Tout C. A., 2011, MNRAS, 414, 3501
Emerick A., Bryan G. L., Mac Low M.-M., 2018, ApJ, 865, L22
Emerick A., Bryan G. L., Mac Low M.-M., 2020, arXiv e-prints, p. arXiv:2007.03702
Eriksson K., Nowotny W., Höfner S., Aringer B., Wachter A., 2014, A&A, 566, A95
Farcy M., Rosdahl J., Dubois Y., Blaizot J., Martin-Alvarez S., 2022, arXiv e-prints, p. arXiv:2202.01245
Fielding D., Quataert E., Martizzi D., Faucher-Giguère C.-A., 2017, MNRAS, 470, L39
Fielding D. B., et al., 2020, ApJ, 903, 32
Fryer C. L., Woosley S. E., Heger A., 2001, ApJ, 550, 372
Gandhi P. J., Wetzel A., Hopkins P. F., Shappee B. J., Wheeler C., Faucher-Giguère C.-A., 2022, arXiv e-prints, p. arXiv:2202.10477
Gatto A., et al., 2017, MNRAS, 466, 1903
Gentry E. S., Krumholz M. R., Dekel A., Madau P., 2017, MNRAS, 465, 2471
Gentry E. S., Krumholz M. R., Madau P., Lupi A., 2019, MNRAS, 483, 3647
Girichidis P., et al., 2016, MNRAS, 456, 3432
Girichidis P., Pfrommer C., Pakmor R., Springel V., 2022, MNRAS, 510, 3917
González Delgado D., Olofsson H., Kerschbaum F., Schöier F. L., Lindqvist M., Groenewegen M. A. T., 2003, A&A, 411, 123
Graur O., et al., 2014, ApJ, 783, 28
Greggio L., Renzini A., 1983, A&A, 118, 217
Guillet T., Teyssier R., 2011, Journal of Computational Physics, 230, 4756
Gutcke T. A., Pakmor R., Naab T., Springel V., 2021, MNRAS, 501, 5597
Gutcke T. A., Pakmor R., Naab T., Springel V., 2022, MNRAS, 513, 1372
Haardt F., Madau P., 1996, ApJ, 461, 20
Hayward C. C., Hopkins P. F., 2017, MNRAS, 465, 1682
Hirai Y., Fujii M. S., Saitoh T. R., 2021, PASJ, 73, 1036
Hislop J. M., Naab T., Steinwandel U. P., Lahén N., Irodotou D., Johansson P. H., Walch S., 2021, arXiv e-prints, p. arXiv:2109.08160
Höfner S., Olofsson H., 2018, A&ARv, 26, 1
Hopkins P. F., Kereš D., Oñorbe J., Faucher-Giguère C.-A., Quataert E., Murray N., Bullock J. S., 2014, MNRAS, 445, 581
Hopkins P. F., et al., 2018, MNRAS, 480, 800
Hu C.-Y., 2019, MNRAS, 483, 3363
Hu C.-Y., Naab T., Walch S., Glover S. C. O., Clark P. C., 2016, MNRAS, 458, 3528

Hu C.-Y., Naab T., Glover S. C. O., Walch S., Clark P. C., 2017, MNRAS, 471, 2151
Hu C.-Y., et al., 2022, arXiv e-prints, p. arXiv:2208.10528
Janka H.-T., 2012, Annual Review of Nuclear and Particle Science, 62, 407
Karachentsev I. D., Makarov D. I., Kaisina E. I., 2013, AJ, 145, 101
Katz N., 1992, ApJ, 391, 502
Keller B. W., Wadsley J., Benincasa S. M., Couchman H. M. P., 2014, MNRAS, 442, 3013
Keller B. W., Wadsley J., Couchman H. M. P., 2016, MNRAS, 463, 1431
Kennicutt Robert C. J., 1989, ApJ, 344, 685
Kim C.-G., Ostriker E. C., 2015, ApJ, 802, 99
Kim C.-G., Ostriker E. C., 2017, ApJ, 846, 133
Kim C.-G., Ostriker E. C., 2018, ApJ, 853, 173
Kim J.-h., et al., 2014, ApJS, 210, 14
Kim J.-h., et al., 2016, ApJ, 833, 202
Kim C.-G., et al., 2020a, ApJ, 900, 61
Kim C.-G., et al., 2020b, ApJ, 903, L34
Kimm T., Cen R., 2014, ApJ, 788, 121
Kimm T., Cen R., Devriendt J., Dubois Y., Slyz A., 2015, MNRAS, 451, 2900
Kobayashi C., Karakas A. I., Lugaro M., 2020, ApJ, 900, 179
Kroupa P., 2001, MNRAS, 322, 231
Lancaster L., Ostriker E. C., Kim J.-G., Kim C.-G., 2021, ApJ, 922, L3
Li M., Bryan G. L., 2020, ApJ, 890, L30
Li M., Ostriker J. P., Cen R., Bryan G. L., Naab T., 2015, ApJ, 814, 4
Li M., Bryan G. L., Ostriker J. P., 2017, ApJ, 841, 101
Mac Low M.-M., McCray R., 1988, ApJ, 324, 776
Maíz Apellániz J., Pantaleoni González M., Barbá R. H., Simón-Díaz S., Negueruela I., Lennon D. J., Sota A., Trigueros Páez E., 2018, A&A, 616, A149
Mannucci F., Della Valle M., Panagia N., 2006, MNRAS, 370, 773
Maoz D., Graur O., 2017, ApJ, 848, 25
Maoz D., Mannucci F., Nelemans G., 2014, ARA&A, 52, 107
Martizzi D., Fielding D., Faucher-Giguère C.-A., Quataert E., 2016, MNRAS, 459, 2311
Matteucci F., Greggio L., 1986, A&A, 154, 279
McKee C. F., Ostriker J. P., 1977, ApJ, 218, 148
McQuinn K. B. W., van Zee L., Skillman E. D., 2019, ApJ, 886, 74
Mitchell P. D., Schaye J., Bower R. G., Crain R. A., 2020, MNRAS, 494, 3971
Moore B., 1994, Nature, 370, 629
Naab T., Ostriker J. P., 2017, ARA&A, 55, 59
Nath B. B., Shchekinov Y., 2013, ApJ, 777, L12
Navarro J. F., Frenk C. S., White S. D. M., 1996, ApJ, 462, 563
Nelson D., et al., 2019, Computational Astrophysics and Cosmology, 6, 2
Oh S., Kroupa P., 2016, A&A, 590, A107
Ohlin L., Renaud F., Agertz O., 2019, MNRAS, 485, 3887
Olofsson H., González Delgado D., Kerschbaum F., Schöier F. L., 2002, A&A, 391, 1053
Pignatari M., et al., 2016, ApJS, 225, 24
Poelarends A. J. T., Herwig F., Langer N., Heger A., 2008, ApJ, 675, 614
Poveda A., Ruiz J., Allen C., 1967, Boletin de los Observatorios Tonantzintla y Tacubaya, 4, 86
Prgomet M., Rey M. P., Andersson E. P., Segovia Otero A., Agertz O., Renaud F., Pontzen A., Read J. I., 2022, MNRAS, 513, 2326
Raiteri C. M., Villata M., Navarro J. F., 1996, A&A, 315, 105
Ramstedt S., Schöier F. L., Olofsson H., 2009, A&A, 499, 515
Read J. I., Agertz O., Collins M. L. M., 2016, MNRAS, 459, 2573
Read J. I., Iorio G., Agertz O., Fraternali F., 2017, MNRAS, 467, 2019
Renzo M., et al., 2019, A&A, 624, A66
Ritter C., Herwig F., Jones S., Pignatari M., Fryer C., Hirschi R., 2018, MNRAS, 480, 538
Roca-Fàbrega S., et al., 2020, arXiv e-prints, p. arXiv:2001.04354
Romeo A. B., Agertz O., Moore B., Stadel J., 2008, ApJ, 686, 1
Rosdahl J., Schaye J., Teyssier R., Agertz O., 2015, MNRAS, 451, 34
Rosen A., Bregman J. N., 1995, ApJ, 440, 634
Rosen A. L., Lopez L. A., Krumholz M. R., Ramirez-Ruiz E., 2014, MNRAS, 442, 2701
Sawala T., et al., 2015, MNRAS, 448, 2941
Schaye J., et al., 2015, MNRAS, 446, 521
Schmidt M., 1959, ApJ, 129, 243
Schöier F. L., Olofsson H., 2001, A&A, 368, 969
Schroetter I., et al., 2016, ApJ, 833, 39
Schroetter I., et al., 2019, MNRAS, 490, 4368
Sedov L. I., 1959, Similarity and Dimensional Methods in Mechanics. Academic Press, New York
Seitenzahl I. R., et al., 2013, MNRAS, 429, 1156
Sharma P., Roy A., Nath B. B., Shchekinov Y., 2014, MNRAS, 443, 3463
Silva M. D. V., Napiwotzki R., 2011, MNRAS, 411, 2596
Smith M. C., 2021, MNRAS, 502, 5417
Smith M. C., Sijacki D., Shen S., 2019, MNRAS, 485, 3317
Smith M. C., Bryan G. L., Somerville R. S., Hu C.-Y., Teyssier R., Burkhart B., Hernquist L., 2021, MNRAS, 506, 3882
Somerville R. S., Davé R., 2015, ARA&A, 53, 51
Sormani M. C., Treß R. G., Klessen R. S., Glover S. C. O., 2017, MNRAS, 466, 407
Springel V., 2005, MNRAS, 364, 1105
Steinwandel U. P., Bryan G. L., Somerville R. S., Hayward C. C., Burkhart B., 2022, arXiv e-prints, p. arXiv:2205.09774
Stone R. C., 1991, AJ, 102, 333
Su K.-Y., et al., 2018, MNRAS, 480, 1666
Sutherland R. S., Dopita M. A., 1993, ApJS, 88, 253
Tammann G. A., Loeffler W., Schroeder A., 1994, ApJS, 92, 487
Tang S., Wang Q. D., Mac Low M.-M., Joung M. R., 2009, MNRAS, 398, 1468
Tasker E. J., Brunino R., Mitchell N. L., Michielsen D., Hopton S., Pearce F. R., Bryan G. L., Theuns T., 2008, MNRAS, 390, 1267
Taylor G., 1950, Proceedings of the Royal Society of London Series A, 201, 159
Teyssier R., 2002, A&A, 385, 337
Teyssier R., Pontzen A., Dubois Y., Read J. I., 2013, MNRAS, 429, 3068
Thornton K., Gaudlitz M., Janka H. T., Steinmetz M., 1998, ApJ, 500, 95
Tumlinson J., Peeples M. S., Werk J. K., 2017, ARA&A, 55, 389
Veilleux S., Cecil G., Bland-Hawthorn J., 2005, ARA&A, 43, 769
Vink J. S., 2015, Very Massive Stars in the Local Universe. Astrophysics and Space Science Library Vol. 412, Springer, Cham (arXiv:1406.4836), doi:10.1007/978-3-319-09596-7
Vogelsberger M., et al., 2014, MNRAS, 444, 1518
Walch S., et al., 2015, MNRAS, 454, 238
Wheeler C., et al., 2019, MNRAS, 490, 4447
Yates R. M., Henriques B. M. B., Fu J., Kauffmann G., Thomas P. A., Guo Q., White S. D. M., Schady P., 2021, MNRAS, 503, 4474
Zapartas E., et al., 2021, A&A, 656, L19
Zhang D., 2018, Galaxies, 6, 114

APPENDIX A: ALL SIMULATIONS

Here we present the full suite of simulations aimed at extensively exploring how the natal velocity distribution of individual stars affects our feedback model. The `stir` model is parameterized by σ_v, for which we tested values 0, 0.01 km s^{-1} and 1 km s^{-1}. This model intends to allow conatal stars to have diverging trajectories arising from small perturbations in the gravitational potential. That the stars do not do so without `stir` is a numerical effect of the collisionless particle-mesh gravity solver, and thus a small value for σ_v is preferred. Nonetheless, our results do not change drastically between the values we tested, as shown in Figure A1.

The `kick` model implements walkaway and runaway stars following the velocity distribution of stars escaping clusters through dynamical interactions (Oh & Kroupa 2016). Because both the fraction of stars born in clusters and the fraction of stars which escape clusters is not well known, we parameterize this with a kick fraction $f_{\rm kick}$ and apply it only to massive stars (> 8 M$_\odot$). We tested values 0.01, 0.1, 0.2, 0.5 and 1.0. Note that for $f_{\rm kick} = 1.0$ the fraction

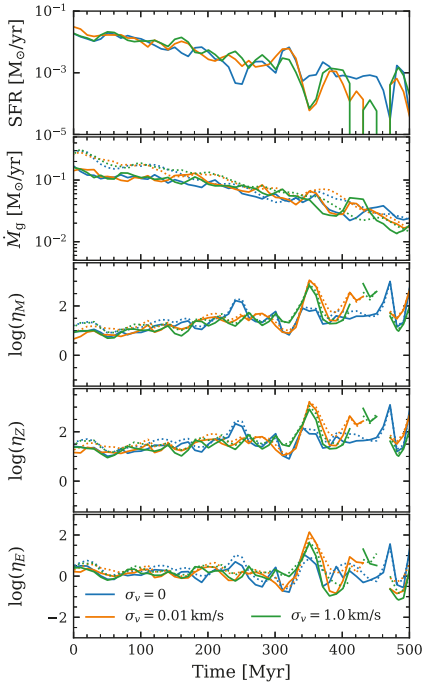

Figure A1. The top two rows show SFR and mass outflow rate, while the remaining three rows show mass, metal and energy loading from top to bottom, all as a function of time for the `stir` simulations. Rates are computed in 10 Myr time-bins, with filled lines showing the *launching* interface and dotted lines showing the *inner-outer halo* interface. Different values of σ_v are denoted in the legend of the bottom plot.

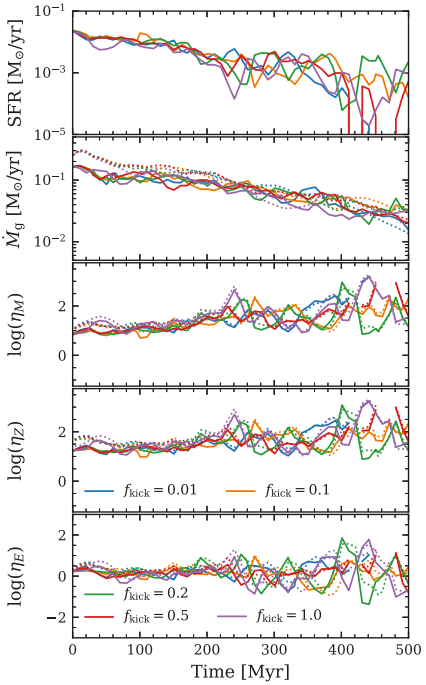

Figure A2. Same as for Figure A1, but for the `kick` models. Different values of f_{kick} are denoted in the legends of the bottom two plots.

of massive runaway stars is 14%. We find little to no effect from runaway stars for all values, as shown in A2.

Finally, in Figure A3 we show the locations of recent CCSNe for all models with the face-on view in the upper plot and edge-on view in the lower plot. This is shown on top of the temperature maps of each simulation. Notably, we see how the number of *out-of-disc* SNe increase, as we increase f_{kick}.

This paper has been typeset from a TEX/LATEX file prepared by the author.

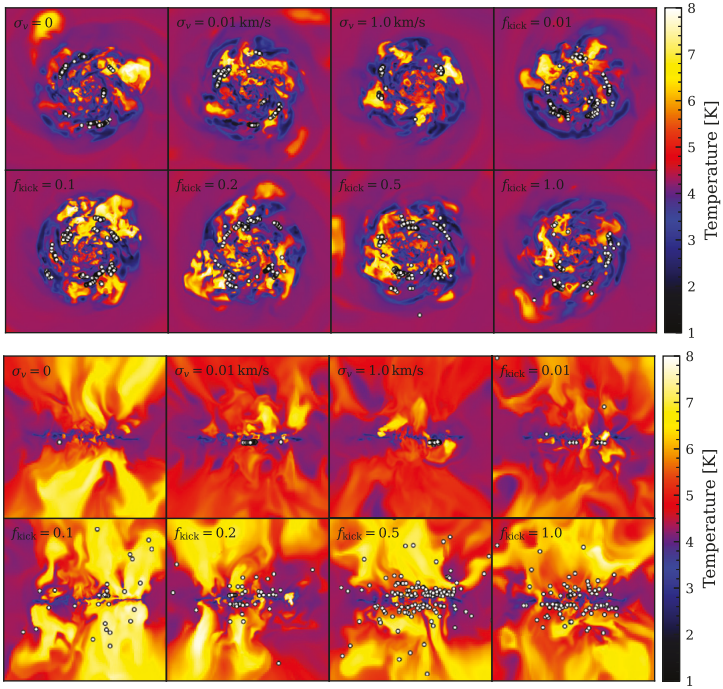

Figure A3. Gas temperature in slices through the centre of our simulation boxes showing the face-on view in the top panels and edge-on view in the bottom panels. All plots shown are for t = 400 Myr, and the panels have a width of 8 kpc. Each panel shows a different simulation denoted by the label in the upper left corner. The location of recent (< 5 Myr in the disc; < 50 Myr outside the disc) SNe are shown in white points.